Characterization of exoplanets and their host-stars with high precision photometry from ground-based and satellite observations.

Dissertation with the aim of achieving a doctoral degree
at the Faculty of Mathematics, Informatics and Natural Sciences

Department of Physics
Universität Hamburg

submitted by:

Panagiotis Ioannidis

Hamburg, 2016

Day of oral defense: 15.06.2016

Evaluators of the dissertation:
Prof. Dr. J. H. M. M. Schmitt
Prof. Dr. Ansgar Reiners

Evaluators of the defense:
Prof. Dr. J. H. M. M. Schmitt
Prof. Dr. A. Bonafede
Prof. Dr. R. Banerjee
Prof. Dr. Brüggen
Prof. Dr. P. H. Hauschildt

Acknowledgements

I am grateful to the people who have helped me during my Ph.D. studies, without however to forget those who supported my studies prior to that.

I owe enormous gratitude to my supervisor Prof. Dr. Jürgen H.M.M. Schmitt, who always found time for me and provided levels of support superior to the support that the majority of other students, known to me, accepted from their supervisors. I feel fortunate to have had a supervisor who afforded me the freedom to pursue my own ideas and encouraged such thinking throughout. I account my self privileged to be the student of such a smart and foresightful scientist. I will always extend my warmest thanks to him for everything he has done for me.

I would also like to thank my other GrK supervisors Dr. Klaus F. Huber and Prof. Dr. Sonja Schuh, for their unerring support and guidance throughout my years as a Ph.D student. Special thanks to my dissertation evaluators Prof. Dr. Jürgen H.M.M. Schmitt and Prof. Dr. Ansgar Reiners, for taking the time to so carefully read and referee this work. In addition I would like to thank Dr. Uwe Wolter, for proofreading and helping form my thesis. Also I would like to thank all the other members of the GrK 1351/2 and employees of Hamburg Observatory for their tirelessly responds and help with all my requests. A special thanks to my friend and collaborator Chrysa Avdellidou, for the long and thoughtful conversations and support.

Furthermore, I acknowledge the funding through the DFG grant RTG 1351/2 "Extrasolar planets and their host stars", without which my thesis would not be possible to conclude.

I would like to thank my mother and father for their love and immeasurable support throughout my life and my studies. Without them none of my achievements would have been possible. Finally I thank Christina, my beautiful star, whose continuous support encourages me to steadily improve as a person, as well as a scientist. I cannot find words to express my love for you.

To Christina...

Abstract

The quest for exoplanets is motivated by our urge to understand the planet formation in our solar system, along with the expectation of finding inhabited new worlds. Today we have confirmed the existence of almost 2000 exoplanets, discovered from several surveys using a variety of different methods. Yet, the main part of the known planet population has been found from the space telescope *Kepler*, with the method of transits. In contrast to our initial expectations, extra solar planets come in a plethora of sizes and orbital configurations. Studying those objects we gain insight into the planet formation processes and the population of planets in our galactic neighborhood.

A useful side-product from our chase for the discovery of new exoplanets, is the creation of a large database with high accuracy, often continuous, stellar observations. Using these data, we can study the photospheric activity of the planet-hosting stars as well as the planets. The most obvious effect of stellar magnetic activity is the appearance of dark spots on the stellar photosphere. Because of the stellar rotation, these spots appear and disappear periodically from the visible hemisphere of the star. This effect leads to formation of periodic variations in the observed stellar flux. These photometric modulations are a precious source of informations about the star, as they offer an insight into processes like i.e., differential rotation and the existence, or absence, of magnetic cycles.

My thesis is dedicated to the improvement of the characterization of exoplanets around active stars, along with the study of the photospheric activity of their hosts, using high precision photometric data.

To this end, I began my studies with the characterization of the planets around the active star Kepler-210. Furthermore, with the use of spot modeling in combination with other established methods I studied the activity modulations in the light curve of Kepler-210.

The influence of spots on stellar light curves has a negative impact on the characterization of transiting planets. The occasional occultations of starspots by planets may affect the estimation of the transit parameters, e.g. the mid-transit time. To evaluate the probability for the detection of spot induced transit timing variations (TTV), I designed and ran a set of simulations, with a variety of star-planet and starspot configurations. Furthermore, I introduce the technique of unsharp masking as a tool for transit light curve analysis. I successfully apply this method in order to examine the origins of the photometric modulations and timing variations of KOI-1452.

The main reason for the limited precision of ground based observations is the scintillation noise. Atmospheric scintillation is the wavefront distortion of electromagnetic radiation due to the turbulent higher layers of the atmosphere. In an effort to understand the scintillation noise effects on the light curves, we assembled a fast imaging telescope in order to simultaneously study the statistical properties of scintillation on multiple targets. The results of this study suggest that, with systematic scintillation studies with our fast imaging telescope, it is possible to improve the ground based photometry, i.e, to reach sub milimag precision, with the use of small telescopes. Besides scintillation studies, the fast imager is ideal for high precision differential photometry of bright variable stars and large planets. As a proof of concept I demonstrate observations of the variable star ϵ-Cep.

Zusammenfassung

Die Erforschung von Exoplaneten eröffnet uns ein tieferes Verständnis der Planetenentstehung in unserem Sonnensystem und wird von der langfristigen Hoffnung begleitet, lebensfreundliche neue Welten zu finden. Bis heute haben wir die Existenz von fast 2000 Exoplaneten bestätigt, die mithilfe einer Vielzahl unterschiedlicher Methoden entdeckt wurden. Ein Großteil der uns bekannten Planetenpopulation wurde mit dem Transitverfahren von dem Weltraumteleskop Kepler gefunden. Entgegen unseren ursprünglichen Erwartungen treten extrasolare Planeten in sehr verschiedenen Größen und orbitalen Konfigurationen auf. Indem wir diese Objekte studieren, gewinnen wir einen Einblick in die Prozesse der Planetenbildung und die Population der Planeten in unserer galaktischen Nachbarschaft.

Ein vielseitiges Nebenprodukt der Bestrebungen, neue Planeten zu entdecken, ist der Aufbau einer großen fortlaufenden Datenbank stellarer Beobachtungen mit hoher Genauigkeit. Auf Grundlage dieser Daten können wir verschiedene Planeteneigenschaften ebenso wie die photosphärische Aktivität der Zentralsterne untersuchen. Der auffälligste Effekt der magnetischen Aktivität der Sterne ist das Auftreten dunkler Flecken in der stellaren Photosphäre. Wegen der stellaren Rotation treten diese Flecken zumeist periodisch auf der sichtbaren Hemisphäre des Sterns auf, um dann wieder von dieser zu verschwinden. Dieser Effekt führt zu einer quasi-periodischen Variation der beobachteten stellaren Flüsse. Diese photometrischen Modulationen liefern wertvolle Informationen über den Stern, da sie uns beispielsweise Einsicht in die Prozesse der differentiellen Rotation ermöglichen und die Existenz oder Abwesenheit magnetischer Zyklen anzeigen.

Meine Doktorarbeit beschäftigt sich mit der Verbesserung der Charakterisierung von Exoplaneten um aktive Sterne. Darauf aufbauend wird eine Untersuchung der photosphärischen Aktivität ihrer Zentralsterne mithilfe hochpräziser photometrischer Daten durchgeführt.

Meine Untersuchungen habe ich mit der Charakterisierung der Planeten um den aktiven Stern Kepler-210 begonnen. Aufgrund der Ergebnisse meiner Untersuchung über die Aktivitätsmodulation von Kepler-210 schlage ich zudem den Gebrauch von Spot-Modellen in Verbindung mit anderen bewährten Methoden vor, um photosphärisch aktive Sterne zu untersuchen.

Unglücklicherweise erschwert der Einfluss der Flecken auf stellaren Lichtkurven die Charakterisierung der bedeckenden Planeten. Die gelegentliche Bedeckung von Sternflecken durch Planeten hat Auswirkungen auf die aus den Transits bestimmten Parameter, wie zum Beispiel den gemessenen Zeitpunkt der Transitmitte. Ich habe Simulationen mit einer Vielzahl von Stern-Planet- und Sternflecken-Konfigurationen entwickelt und durchgeführt, um die Wahrscheinlichkeit der Entdeckungen von fleckeninduzierten Transitmittelpunktvariationen (transit timing variations - TTVs) beurteilen zu können. Darauf aufbauend schlage ich die Methode "unsharp masking" als Werkzeug zur Analyse der Transitl-Lchtkurven vor. Ich wende diese Methode an, um die Urspr'onge der photometrischen Modulationen und Zeitvariationen des KOI-1452 zu untersuchen.

Der Hauptgrund für die eingeschränkte Präzision bodengebundener photometrischer Beobachtungen liegt in ihrer Störung durch atmosphärische Szintillation. Szintillation ist die Störung der Wellenfront elektromagnetischer Strahlen, die auf Störungen durch unruhige höhere Schichten der Atmosphäre zurückzuführen ist. In dem Bestreben, diese Szintillationseffekte zu verstehen, haben wir ein astronomisches Schnellbild-Teleskop aufgebaut, um gle-

ichzeitig die statistischen Eigenschaften der Szintillation bei mehreren Zielobjekten studieren zu können. Das Ergebnis dieser Studie zeigt, dass es möglich ist, aufgrund systematischer Untersuchungen mit diesem "fast imager" die bodenbasierte Photometrie zu verbessern und beispielsweise sub-milimag-Präzision mit kleinen Teleskopen zu erreichen. Neben diesen Studien der Szintillation eignet sich der" fast imager" ideal für die hochgenaue differentielle Photometrie bei hellen variablen Sternen und großen Planeten. Zum Test und Nachweis dieser Möglichkeiten habe ich mit diesem Teleskop Beobachtungen variabler Sterne durchgeführt und ausgewertet.

Contents

Chapter 1

Introduction

1.1 Cosmos

The term Cosmos was introduced by the Greek philosopher Pythagoras, in order to describe the "totality" or the "order" of the universe. For him and for the most of the ancient civilizations, the sky was a great source of inspiration and a mystery waiting to be solved. The Earth was in the middle and the sky was occupied by those little lights known as *ἀστέρες* . There were two kinds of those; the *ἀπλανείς ἀστέρες* (stars) which were stable in respect to the other ones and the seven *πλάνιτες ἀστέρες* (planets), the wanderers. The mightier of them, *Ἥλιος* (the Sun), dominates during the day while during the night the brightest would be his sister, *Σελήνη* (the Moon). The first attempt to describe the movement of the planets was made by the Greeks, who introduced a geometric model of their motions. In his Almagest (Μεγίστη), written in the 2^{nd} century A.D., Ptolemy presented the top of those theories by introducing a set of ellipses and epicycles in order to explain the orbits of the planets (e.g., Fig. 1.1).

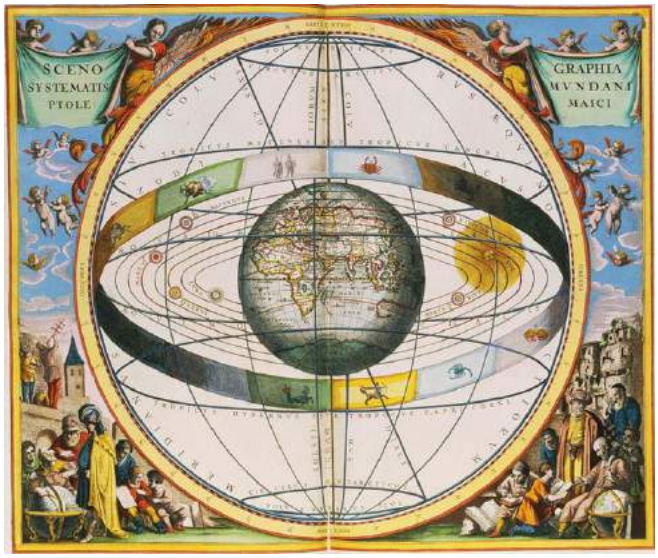

Figure 1.1: The Ptolemaic model for the Cosmos, illustrated by Cellarius Andreas (c. 1596-1665)

Despite its complexity, the Ptolemaic model, was so successful that it took almost 2000 years until Copernicus, following the proposal of Aristarchus from Samos, managed to "shake" the Earth from its exquisite position. Nevertheless, it was Galileo with his telescope and Kepler with his theory for the elliptical nature of the planetary orbits who placed the Sun in the middle of the Cosmos. In the same period, a monk named Giordano Bruno, re-introduced[1] an idea well buried since then; the existence of worlds other than ours, planets orbiting not our Sun but other stars, the extrasolar planets.

Since then, there have been great advances and achievements regarding astronomy. By now, we confirmed the existence of more than 1000 extrasolar planets. The continuous improvement of our theories and instrumentation allows us to study those objects and their host stars.

[1] many ancient Greek (i.e. Epicurus, Democritus, Aristotle) and other philosophers where on the belief that our world cannot be the only one.

1.2 Sun

It was known, even from ancient times, that in rare occasions, dark spots are observable on the Sun. It was until the invention of the telescope, with which it was made clear, that those spots are not rare at all. In fact scientists realized that it is possible to use sunspot features as movement, shape and location to study the properties of the Sun itself.

Christoph Scheiner used those features to measure the solar rotational period at the equator. Additionally he realized that the spots in higher latitudes are rotating more slowly than those in latitudes closer to the solar equator, product of the differential rotation of the Sun. During the 19^{th} century and after long term observations of sunspots, Schwabe (1844) discovered that the population of spots is periodically changing, about every 10 years (what today is known as the 11-years Solar cycle). A few years later, Carrington (1863) noted that the spots tend to appear closer to the solar equator, during a cycle. Spoerer (1890), refined those observations to form the so-called Spörer's Law. A practical method to demonstrate this effect, which was introduced by Maunder (1904), is the widely known "butterfly diagram" as appears in Fig. 1.2. Spörer, also, discovered an anomaly in the sunspot data; the lack of sunspots between the years 1645 - 1715. Ironically, this peculiarity, which still remains an unsolved mystery, is known as Maunder minimum due to a later paper of Maunder, with comments on the conclusions of Spörer.

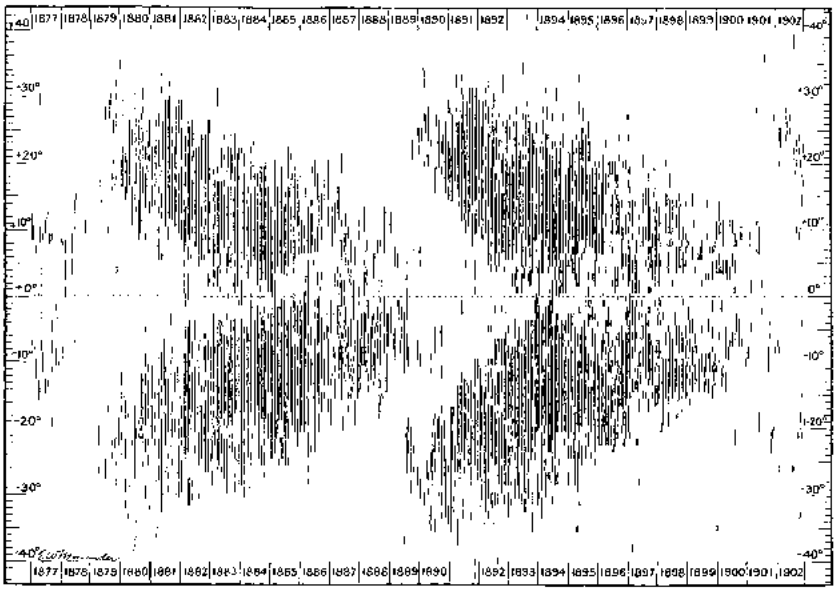

Figure 1.2: "Distribution of the spot center in latitude, rotation by rotation, 1877-1902", produced by Maunder (1904)

At the beginning of the previous century, Hale (1908), proved that the spotted areas are highly magnetized, while after about a decade he and his collaborators concluded that the spots of a Solar hemisphere have the same polarity which is opposite to the polarity of the spots of the other hemisphere and that the polarity of the spots is stable during a cycle and reverses from one cycle to the other. Hale's research revealed the physical basis of the 11-year cycle, which later allowed Babcock (1961) to express his theory introducing a qualitative Solar dynamo model with a period of 22-years.

After the discovery of the connection between the sunspots and the activity of the Sun, it became obvious that our understanding of the astrophysics would increase with the quality and quantity of the Solar observations. Thus a plethora of Solar Observatories were built to observe the Sun from the Earth or space. In addition to the resolved pictures of the Sun, some of those observatories where designed to measure the Total Solar Irradiance (TSI) of the Sun. Fröhlich (2012) presents a synthetic plot with the TSI measurements of the last 3.5 decades, using several instruments, which is illustrated in Fig. 1.3. Lanza et al. (2003) used TSI data from the VIRGO instrument on SOHO satellite, in order to create a spot model, treating the Sun as a star. His model proved that it is possible to extract the sunspot properties as the location and the size, using the TSI data, which one can easily compare to the photometry data from other stars.

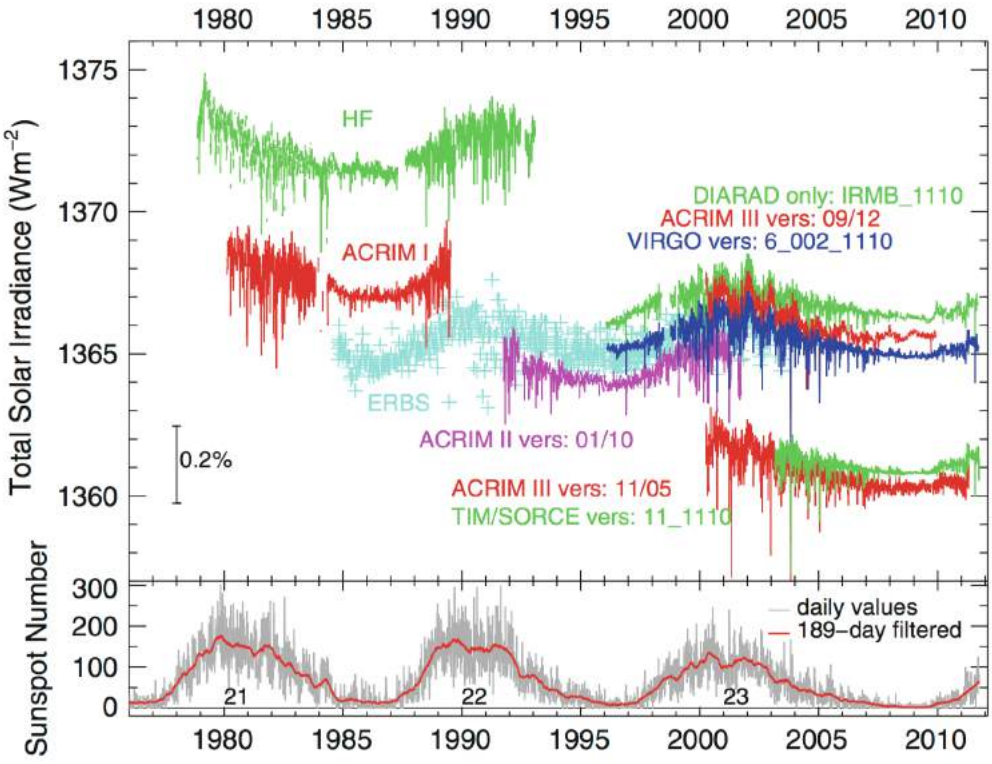

Figure 1.3: Top: The daily averaged values of the Sun's total irradiance from radiometers on different space platforms, since November 1978. Bottom: The sunspot number as an illustration of Solar activity for the three cycles.

1.3 Stars

1.3.1 From solar to stellar...

Although the idea that the fixed stars on the sky where distant Sun-like objects existed from ancient times, it started to reach a consensus among scientists after the 16^{th} century. The confirmation came in the second half of the 1800s, when the comparison of Solar and stellar spectrum photographs became possible. However, the similarities between the stars and the Sun were few and a massive stellar classification effort begun. The outcome of this effort was the construction of the famous H-R diagram by E. Hertzsprung and H. N. Russell. Amongst the other interpretations of the H-R diagram, it became clear that by observing other stars, especially stars with similar features to the Sun, we would be able to understand the majority of the Solar evolutionary stages.

1.3.2 Activity studies

In his book "Cosmical magnetic fields" Parker (1979) shows that stars with sufficient rotation rates to trigger a solar-like dynamo effect and the existence of an outer convective envelope should show similar to the Sun activity. The Sun is considered to be "active" when the number of spots is maximum, in every 11-year cycle. Nevertheless, It is not only the number of spots that which can be used as an indication for high activity.

1.3.2.1 X-rays observations and Coronae

The advance in spectroscopy, during the late 19^{th} century, led to the discovery of the elements Helium (J. Jansen, 1868) and Coronium (Harness & Young 1869). Both elements would introduce strong emission lines in the solar corona spectrums, which where measured during total solar eclipses. Another characteristic of the solar corona was its connection to the number of sunspots. According to Mitchell (1929), it was already known that "there is an intimate connection between the form of the corona and the sun-spot period". Finally W. Grotrian and Edlén (1943) made clear that the Coronium was nothing more than ionized Fe XIV. The solution of the mystery of Coronium created another difficulty to answer; i.e., the problem of the coronal heating. The levels of ionization suggested by the observations, require temperatures of at least a few hundred thousands Kelvin, much higher than the temperature of the Solar photosphere. There have been many theories attempting to solve the coronal heating problem but the real mechanism causing the effect is still not very well understood.

Obtaining observations of the Solar corona from the Earth is only possible during total Solar eclipses or with coronagraphs. The reason is that in any other case the Solar spectrum is dominated by light coming from the photosphere of the Sun. A solution to that problem was to observe the Sun in different wavelengths where the corona would be dominant. A wavelength range where the photosphere of the Sun is dark while the corona is very bright due to its very high temperatures are the X-rays. Unfortunately the atmosphere of the Earth doesn't allow X-rays to reach the ground so, finally, the only possible way to observe was from space. An interesting attempt was the mount of counter tubes on V-2 rockets, remnants of WWII, with aim to observe between 0 Å and 2100 Å. The first X-ray observatory, outside the Earth's atmosphere was set on the space station *Skylab*, setting the stage for the later missions. A great contribution of *Skylab* was the detection of coronal holes, which would rotate in a solid way, preserving their shape for many 27-days rotations.

The true revolution in X-ray astronomy began with the launch and operation of the HEAO B satellite or Einstein observatory at 1978 - 1981. This offered 10^3 times better sensitivity in point sources which allowed the detections of stellar X-ray sources. Using Einstein data, Vaiana et al. (1981) confirmed that different types of stars have different X-ray luminosities, with a trend for more massive types to present persistently higher luminosities. In the same year Pallavicini et al. (1981) determined the correlation between the rotational velocity $v \cdot \sin(i)$ and X-ray luminosity (activity). For early type stars their X-ray luminosities are proportional to their bolometric luminosities while for late type stars the X-ray luminosity is strongly dependent on the rotational velocity, which means that the late type stars are more active when they rotate faster and thus when they are younger.

1.3.2.2 Spectroscopy

The introduction of the solar magnetograph by Babcock (1953) revealed new features of the Sun, correlated to its active regions. One of them, noted by Leighton (1959), is the emission of H- and K- Ca II around or close to spot formations. In addition to that, Sheeley (1967) was able to relate, as expected, the H- Ca II line to the solar cycle. Consequently Wilson (1968) observed for a year a list of 139 stars, some of which presented "no undoubted variations" in the intensity of the H- and K- Ca II lines, probably the result of activity cycles similar to the 11-year Solar cycle. About 10 years later Wilson (1978) published the long term monitoring of 91 main-sequence stars, most of which presented obvious H-K variations .

Cold spots on the surface of a star introduce anomalies in the profile of stellar absorption lines. This effect was first mentioned by Fekel (1980). Vogt & Penrod (1983) used this observation to propose a method in order recreate resolved images fast rotating star. A step further was achieved by Marsh & Horne (1988) and the Zeeman-Doppler imaging method, with which it is possible to create a map of the magnetic field of a star. Due to the Zeeman effect, the absorbed or emitted light in spectral lines is polarized because of the existence of strong magnetic fields on the stellar surface. Assuming relative fast rotating stars, it is possible to monitor the Zeeman signatures from one stellar rotation to the other and create an iterative reconstruction of the stellar magnetic field (see, Donati & Collier Cameron (1997)).

The differential rotation of a star, can indirectly work also as an indicator for activity. In the case of a Solar-like activity cycles the spot migration to different latitudes should also be indicated by differences in the measured rotational period of the star. Reiners & Schmitt (2002) proposed an alternative method to study the differential rotation of stars, skipping the thorough and some times cumbersome photospheric reconstruction of the Doppler Imaging process. Instead they prove that it is possible to measure differential rotation of stars by studying their absorption lines with the Fourier Transform method.

1.3.2.3 Long-term photometry from the ground

Although by making use of X-rays and spectral analysis in the optical it is possible to successfully study the magnetic activity of stars, the number of objects suitable for such studies is small; X-ray photons can only be detected from stars in the solar neighborhood and only from space, while the spectral analysis of faint stars requires sophisticated spectrographs and meter class telescopes.

Due to the simplicity of photometry observations and in combination to long-term photometric surveys the statement of Wilson (1968) that "the uncovering of analogous (to the Sun) cycles by luminosity

measurements is not practical" was meant to be proven wrong. A plethora of long term photometric studies (see,Strassmeier et al. (1989), Jetsu et al. (1990), Rodono & Cutispoto (1992)) resulted to the collection of an extensive record of light curves of active binary and single stars. The mechanism responsible for the variability of the stellar flux is not different than the TSI fluctuations measured on the Sun. As a starspot appears on the visible hemisphere of a star, the measured stellar flux is reduced. In cases where the lifetime of the spots is longer than the stellar rotation, the fluctuations appear in correlation to the rotational period (e.g., Rodono et al. (1986)).

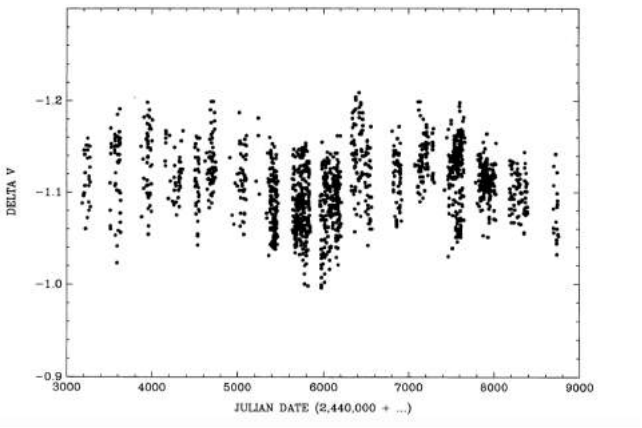

Figure 1.4: The V light curve of σ Gem binary star, presented by Henry et al. (1995). There is clear variations, which are accounted to starspots by Henry et al. (1995).

The study of the stellar photometric variations due to spots can reveal a great deal of information about the activity of the star, which are briefly listed bellow:

- *Starspot filling factors, longitudes and lifetimes*: The peak to peak amplitude of the variations is related to the spotted area of the visible hemisphere of the star. The appearance of spots in different longitudes is causing differences in the variations shape from one rotation to the next. By making use of a spot model one can measure the position of the spots and their radius in order to produce the observed modulations. On the other hand the presence of an active region in the same longitude can reveal the life time of those spots.

- *Differential rotation*: Under the assumption that other stars have solar like differential rotation, it is possible to distinguish between the different spot latitudes a star by measuring the variations in the calculated periods of the spots.

- *Spot temperatures*: While a direct measurement of the spot surface brightness is not possible, we can measure it indirectly during the occultation of another star over the spot.

- *Magnetic cycles*: The long-term monitoring of a star may reveal low frequency variability connected to a possible magnetic cycle. Also, a star with a Sun-like magnetic cycle would demonstrate low frequency differences to the peak to peak amplitude of the rotation to rotation variations, as seen in the TSI data of the Sun

A great example of such studies is presented by Henry et al. (1995). In their paper they show the results of the starspot analysis on the light curves of four, photometrically active, eclipsing binaries (e.g., Fig. 1.4).

1.4 Planets

1.4.1 Solar System planets

Whilst six of the eight planets of our solar system have seen since the Babylonians, as early as 2000 B.C., it was not until 16^{th} and 19^{th} century that the rest, Uranus and Neptune, were added to that list. The existence of Uranus might have been known by the ancient times it is possible that it was listed as a star by Hipparchus (Hertzog 1988). The first to confirm that Uranus was not "ἀπλανής ἀστήρ" (a star) was Sir W. Herschel in 1781, who proposed that this object was a comet. Using the Newtonian theory, the astronomers A. J. Lexel and J. E. Bode presented the theory that due to its nearly circular orbit, the new object was not a comet but a new planet.

The use of celestial dynamics on the orbit of Uranus led to the discovery of yet another planet of our Solar System, Neptune. The first to propose the hypothesis that there might be another object further than Uranus was Bouvard in 1821. His theory was based on observations of the positions of Uranus which were not in complete agreement with the calculated ephemeris. Later, Le Verrier and Adams attempted to predict the orbit of that body. Their calculations where accurate enough to lead to the discovery of Neptune by Galle (1846).

Celestial dynamics in combination to observations led to the discovery and orbital characterization of plenty of dwarf planets, e.g. Pluto (P. Lowel 1915), Ceres (G. Piazzi 1801) etc., asteroids and comets.

1.4.2 Extrasolar planets

The hypothesis of other worlds, similar to ours, exists since antiquity. The invention of the telescope and the discoveries of until then unknown objects, i.e. variable stars, galaxies, nebulae etc., meant to reinforce this believe. Yet the observation of extrasolar planets, or "exoplanets", similar to those of our Solar System, would not be trivial.

According to the International Astronomical Union (IAU) the definition of an exoplanet, which issued in 2001 and modified in 2003 (WGESP IAU 2003) contains the following criteria:

- Objects with true masses below the limiting mass for thermonuclear fusion of deuterium (currently calculated to be 13 Jupiter masses for objects of solar metallicity) that orbit stars or stellar remnants are "planets" (no matter how they formed). The minimum mass/size required for an extrasolar object to be considered a planet should be the same as that used in our solar system.

- Substellar objects with true masses above the limiting mass for thermonuclear fusion of deuterium are "brown dwarfs", no matter how they formed or where they are located.

- Free-floating objects in young star clusters with masses below the limiting mass for thermonuclear fusion of deuterium are not "planets", but are "sub-brown dwarfs" (or whatever name is most appropriate).

In the case of the Solar System, the majority of the planets were detected and confirmed by direct visual observations, or imaging, of the sunlight as it is reflected back to Earth from their surface. Nevertheless, due to the high contrast of the starlight in comparison to the reflected light from extrasolar planets, the spatial resolution of the planet from the host star is extremely challenging. Upon the recognition of that fact, astronomers had to explore other, indirect, ways to detect extra solar planets.

1.4.2.1 Orbital perturbations

The successful prediction of Neptune's existence from Le Varrier introduced a new technique for planet detection; the monitoring of the motion of a known object and the comparison of the observed positions with a linear ephemeris. The first claim of such anomalies, observed in extra solar object, was made by Jacob (1855), regarding the resolved binary system 70 Ophiuchi. Jacob attempted to explain the orbit anomalies of the secondary component of the system with the existence assumption of a third, non visible, companion.

Jacob's claims were supported by See (1896). In this publication there is a presentation of a diagram with the comparison between the observed and calculated values (the equivalent of an O-C diagram today) of the angle and distance of the system. However, Moulton (1899) proved that the proposed system would be highly unstable. Finally Heintz (1988) claims that the false detection was to be accounted to instrumentation errors.

1.4.2.2 Astrometry

According to Newton's theory, two gravitationally bound bodies will orbit a common center of mass. As a result, despite the high contrast between the masses of a planet and its host star, the star should also orbit around the common center of mass. The discovery of the unresolved companions of Procyon and Sirius from Bessel (1844), revealed the potential of astrometry to discover, non visible, companions to a star.

Despite that fact though, the first claim for a discovery of a planet was made about 120 years later by van de Kamp (1963) about the detection of an exoplanet orbiting a nearby M-dwarf known as "Barnard's star" . In his paper, van de Kamp (1963) argued that the perturber was a planet 1.6 times more massive than Jupiter on a 4.4 AU orbit.

Unfortunately this claim would also be proven wrong. In follow up observations, Gatewood & Eichhorn (1973), failed to detect the planet. Following the usual trend, a paper from Hershey (1973) revealed that the discovery was an maintenance artifact of the telescope with which the observations were made.

1.4.2.3 Pulsar Timing

The first confirmed detection of exoplanets was announced by Wolszczan & Frail (1992), around the millisecond pulsar PSR B1257+12. Neutron stars consist the last part of the life of a main sequence star with mass between 2 and 8 $M_{\odot}$ and they carry very strong magnetic fields, usually misaligned to the rotational axis of the star. Radiation produced by the neutron star is focused by the magnetic field, into two oppositely-directed beams, in the direction of the axis of the magnetic field. As the star rotates, the beam is swept across the sky and when the beam intercepts the Earth once per rotation, then brief but regular pulses of radiation are seen, much like a lighthouse.

When a planet is introduced, the pulsar is forced to move around the center of mass of the system. In the case of a pulsar and a planet, the center of mass will lie very close to the pulsar, since it is much heavier than the planet. Therefore, during one orbit the pulsar will move a much lesser distance than the planet. However, even thought the pulsar's "wobble" is small, it has an effect on the timing of the emitted pulses. When the pulsar is moving away from the Earth, the time between each pulse becomes slightly longer; conversely, when the pulsar is moving toward the Earth, the time between

pulses becomes slightly shorter. By measuring these periodic changes in pulse timing, it is possible not only to deduce the existence of a planet orbiting around the pulsar, but in addition to estimate the semi-major axis of the planet's orbit, and place a lower limit on the mass of the planet.

Wolszczan & Frail (1992) calculated that the planets around the pulsar PSR B1257+12 had masses 2.8 $M_{\oplus}$ and 3.4 $M_{\oplus}$, with respective orbital periods of 98.2 days and 66.6 days. Despite the remarkable fact of the discovery of two Earth like planets, in relatively wide orbits, the discovery was depreciated due to the fact that the environment of such planets was considered inhabitable.

1.4.2.4 Radial Velocity

An other way to measure the periodic disposition of a star, due to the existence of a visible or not companion is the radial velocity (RV) technique. When there is a companion of mass m around a star of mass M then the system will rotate around the center of mass of the system. The light from the star with the substantial relative radial velocity, will be subject to the Doppler effect. Thus, the frequency of the starlight will decrease when it recedes (redshift) and will increase when the star is approaching (blueshift), as described by the Doppler's law

$$f = \left(\frac{c + u_{\mathrm{s}}}{c + u_{\mathrm{r}}}\right) \cdot f_{\mathrm{o}}, \tag{1.1}$$

where c is the speed of light, u_s the radial velocity component of the star, u_r the relative speed of the observer (Earth) and f_o is the original frequency. The detection of an extrasolar planet with this method involves taking precise measurements of stellar spectrum with an optical telescope and compare the wavelengths of known spectral lines in the stellar spectrum, to wavelengths from laboratory measurements. Each measurement is associated with a specific time. By solving the equation 1.1 as of u_{s} a plot can be created showing the star's radial velocity as a function of time. The result is a sinusoidal curve. The radial velocity semi-amplitude K of this curve is related with the period P of the planet, the inclination i and the eccentricity e of its orbit, with the equation:

$$K = \left(\frac{2\pi G}{P}\right)^{1/3} \frac{m \cdot \sin i}{M^{2/3}} \frac{1}{\sqrt{1 - e^2}}. \tag{1.2}$$

It is only possible to estimate the true mass of the companion, when the inclination of the system is known, using the relationship

$$m_{\mathrm{true}} = \frac{m_{\mathrm{min}}}{\sin i}. \tag{1.3}$$

A direct prediction for the usage of RV measurements for the detection of sub-stellar companions was made by Struve (1952). The advance of spectrographs and telescopes, finally allowed Campbell et al. (1988) to claim that they detected a planet around the star Gamma Cephei, but the discovery was questioned by Walker et al. (1992). Therefore, the first confirmation of the existence of a planet around a main sequence came seven years later when, Mayor et al. (1995), announced the confirmation of planetary companion around the main sequence G-type star 51-Pegasi. The existence of the planet, with mass $0.47 M_{\mathrm{J}}$ in a 4.23 d orbit, was also confirmed, just a few days later, by G. Marcy and P. Butler.

The discovery of 51-Peg b introduced a planet category non-existing in the Solar System; i.e., the so called Hot-Jupiters. The existence of those planets was treated with great suspicion due to the lack of

a known, until then, mechanism for migration of giant planets from orbits further than the snow line, where they are getting formed (see,Pollack et al. (1996)), to closer to the star orbits. Nevertheless, the barrage of planetary discoveries that followed, convinced the majority of the astronomers that those objects are real *and* that they are planets.

1.4.2.5 Transits

The method of transit for planetary observations was known since 1627, when Kepler predicted the transit of planet Venus in front of the Sun for the year 1631. The application of such a method for the detection of extrasolar planets though, became possible at the dawn of the 20^{th} century. The existence of planets in close in orbits and the advance in imaging technology (CCDs) would allow, in principal, the detection of the imperceptible dimming of a star, while a planet orbiting around it is occulting in front of it. Based on that assumption, Charbonneau et al. (2000) and Henry et al. (2000), where able to detect, for the first time, the transit of the RV planet HD 209458 (see, Fig. 1.5).

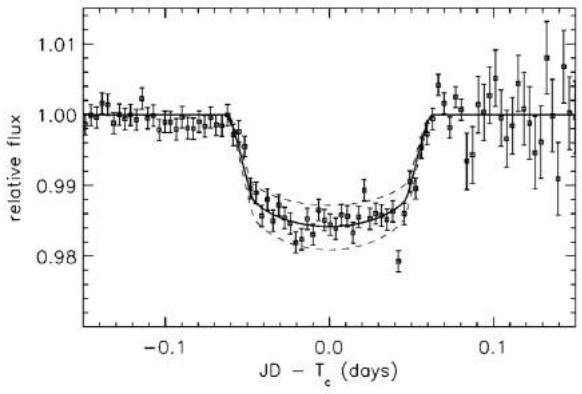

Figure 1.5: The light curve of the first exoplanet transit (Charbonneau et al. 2000).

The fundamental equations for the analytical model of a planetary transit are simple (Mandel & Agol (2002)). Considering the following non-linear system of equations and given the observed transit depth at mid-transit d_{obs}, we can compute the stellar and planetary radii (each scaled by the semi-major axis) $\tilde{R}_\star$ and $\tilde{R}_p$, in addition to the inclination of the orbit i normal with respect to the line of sight;

$$sin^2 i\, cos^2\left(\frac{\pi}{P}T_{14}\right) = 1-(\tilde{R}_\star+\tilde{R}_p)^2 \tag{1.4}$$

$$sin^2 i\, cos^2\left(\frac{\pi}{P}T_{23}\right) = 1-(\tilde{R}_\star-\tilde{R}_p)^2 \tag{1.5}$$

and

$$d_{obs}=\frac{(1-c_1-c_2)+(c_1+2c_2)\,\mu_c-c_2\mu_c^2}{1-\frac{c_1}{3}-\frac{c_2}{6}}\left(\frac{\tilde{R}_p}{\tilde{R}_\star}\right)^2 \tag{1.6}$$

Here P, T_{14} and T_{23} denote the observed period, the observed time between the first and forth contact and the time between the second and third contact respectively. Also c_1 and c_2 account for the quadratic limb darkening coefficients. Finally μ_c denotes the expression

$$\mu_c=\sqrt{1-\frac{cos^2 i}{\tilde{R}_\star^2}}. \tag{1.7}$$

A disadvantage of the transit method is the lack of information regarding the mass of an object. Due to that fact it is relatively easy to misinterpret the signal of a binary star, blended with the light

of another star, in the line of site. Thus, it is necessary to obtain RV measurements of the "candidate" in order to confirm if it is a planet or a false positive detection. Nevertheless the planets with both RV and transit measurements are considered to be the most well studied.

1.4.2.6 Transit Timing Variations

The accuracy with which it is possible to calculate the transit duration, allows for the systematic monitor of the position of the transiting planet. It is then possible to detect other bodies in the system, visible or not, In the same fashion as Le Verrier predicted Uranus (Agol et al. 2005).

A great advantage of this method is the fact that it allows for the measurement of the mass of the components of the system, while in addition it is possible for the most of the systems to calculate an upper limit for the mass, in order for the system to be stable in long term. This feature can work as a substitute of RV measurements, i.e., for systems with low photometric magnitude (see,Sect. 1.4.3).

1.4.2.7 Microlensing

A gravitational microlensing event occurs when, due to random random alignment between a background source star and a foreground star, which may host planet or planetary system. In principal, the background star is acting as source of light which is used to probe the gravitational field of the foreground stars. The relative motion of the source star and lens system allows the light rays from the source to sample different paths through the gravitational field of the foreground system. In the case of the existence of a planet around the lens star, the total gravitational lens magnification of the source star is irregular, due to the creation of caustic lines.

In 1991, Mao & Paczynski (1991) first proposed the use of gravitational microlensing in order to search for irregularities of the gravitational field of the lens star, in case of a microlensing event. The first detection of a planet with the microlensing method was made by Beaulieu et al. (2006) with data of the Optical Gravitational Lensing Experiment (OGLE).

A notable disadvantage of this method is the singularity of the events; the microlensing event cannot be repeated, due to the alteration of the alignment that produced it in first place. Also, the detected planets tend to be several kiloparsecs away from the Sun, a fact that is limiting the follow-up observations with other methods.

1.4.2.8 Direct Imaging

The most successful method for detection of planets in our solar system is by far their direct observation or imaging. Yet, the application of this method for detection of extrasolar planets is not trivial. The extrasolar planets are extremely faint light sources, compared to their host stars. Consequently, the small amounts of light, that originate from them, is lost in the glare from their parent star. So in principal, it is very difficult to detect them directly.

The first step, in order to achieve such a demanding detection, is to increase the contrast between the star and the planet. For most of the star-planet systems, this is not possible with our present means. Nevertheless, for low temperature stars or stars with circumstellar disk, the contrast of the planet can be substantially increased in the mid-infrared, with the help of a chronograph. A notable disadvantage of the observations in mid-infrared wavelengths is that, in contrast to visible or near-infrared observations,

the direct imaging of a planet is limited by the atmospheric emission rather than the site turbulence characteristics.

An other very important factor is the maximum resolving power of the telescope. The resolution power of a telescope is given by the relationship

$$A = \frac{12''}{D/1\ cm} \tag{1.8}$$

where D is the telescope diameter. The angular separation of a star-planet system is given by

$$\tan\theta = \frac{r}{d} \Rightarrow \theta \sim \frac{r}{d} \tag{1.9}$$

where r is the projection of the distance between the star and the planet and d is the distance to the system. Using Eqs. 1.8 and 1.9, it is possible to estimate that the angular separation of a planet, i.e. in distance of 1 AU from its star and 100 ly away from the Sun, is 0.03". A resolution of this order can only be achieved from telescopes with diameter larger than 4 m. In addition, the atmosphere of Earth is limiting the threshold of the best angular resolution to 0.5"-1.2", depending on the astronomical seeing of the telescope's construction area. The development of the adaptive optics (AO) systems allows for the improvement of a telescope's angular resolution. However, even with the largest ground-based telescopes, it is not possible to detect planets which are closer than a few tenths of AU to their host star. The first extrasolar planet ever to be seen was the companion of AB Pic (Chauvin et al. 2005).

Despite those limitations, the direct imaging of extrasolar planets comes with great benefits. Direct detection and direct spectroscopy, have potential for advancing the understanding of extrasolar planets. In combination with other methods of planet detection, direct imaging and spectroscopy can allow to eventually: 1) fully map out the architecture of typical planetary systems and 2) study the physical properties of exoplanets (colors, temperatures, etc.) in depth.

1.4.3 High accuracy photometry

Since the beginning of our our existence, in order to understand our environment, we tend to categorize everything, based in their phenomenology. A plethora of astronomical discoveries originate by this behavior, i..e. the H-R diagram. A very important prerequisite, in order for this method to produce scientifically substantiated results, is the existence of large amount of data from a variety of different objects, considering the time scale of the phenomenon to be studied.

Based on that principle, a vast number of "planet hunting" surveys has been set up, using different methods. For the same reasons described in Sect. 1.3.2.3, the easiest and less expensive way to search for planets is with photometry and, more specifically, the search for transit signals in light curves of stars.

The most successful ground-based surveys for the detection of planets, with the method of transits, it by this date the HATNet (Bakos et al. 2004) and the super-WASP (Pollacco et al. 2006) projects. The fundamental principal on top of which those surveys were built was the coverage of large area of the sky, with robotic, small aperture, telescopes.

Nevertheless, the database created by planets from those surveys, is greatly biased by the fact that the observational time is limited by the alteration between day and night and the accuracy limitation due to the atmosphere and the atmospheric conditions.

The disadvantages of the ground-based surveys were already well known at the time. The only solution would be the design of space-based surveys. Such surveys would in principal be free of systematics caused by the atmosphere while, in the same time, it would have been possible to avoid the day/night alteration and thus maintain constant observations for months or years.

1.4.3.1 The CoRoT satellite

The first space-based telescope, devoted to the search of extrasolar planet transit signals was the *CoRoT* satellite (Baglin et al. 2006). It was launched on 27 December 2006 and its first light was acquired on 18 January 2007. The satellite is equipped with a 28 cm optical tube which has 4 CCDs in its focal plane, two for asteroseismology measures and two for extrasolar planet detections. The observational strategy of *CoRoT* was complicated, with Long and Short runs of observations per field. The maximum observation time was 150 days.

Despite the high signal-to-noise ratio, the *CoRoT* project detected 26 planets in the same regime of semi-major axis as the ground-based observations. Nevertheless, the scientific value of the *CoRoT* light curves is still high as it revealed that such, long term continues observations of stars, would be possible to be used for activity studies.

The light curves of many stars, in the *CoRoT* database, show clear spot induced modulations, correlated to their rotational period of the star. A very well studied star, and planet host, with very profound activity modulations is the CoRoT-2 b. In the same fashion as Henry et al. (1995), Lanza et al. (2009) and Fröhlich et al. (2009) attempted to describe the modulations with spot models and also to detect differential rotation of the star.

Similar studies on CoRoT-2 b (e.g., Wolter et al. (2009), Czesla et al. (2009)) show that the activity of the stars can also have an impact in the transit profile of the planet, in the cases when the planet is occulting over spots. In addition, Huber et al. (2010), proved that it is possible to use the planet and such spot-crossing events in order to describe the variations in the host star's photosphere, in time.

1.4.3.2 The Kepler satellite

A great contribution of the *CoRoT* mission, next to the scientific discoveries, was the revelation of the large spectrum of research opportunities from a space-based survey for transits. As a result, on 7 March 2009, the *Kepler* space observatory was launched. The *Kepler* satellite is carrying a 1.4 m mirror, which with the 42 CCDs in its focal plane, allows for a field-of-view (FOV) equal to 115 deg^2. In contrast to the *CoRoT* observational plan, the *Kepler* observatory was designed to observe the same part of the sky (R.A. 19h 22m 40s and Dec +44° 30' 00") for at least three years. The large size of the mirror in addition to the uninterrupted monitoring of the same FOV for such a long time, offers the opportunity, at least in principal, to detect Earth like planets.

As of November 2015, the *Kepler* mission identified as planets the signal of 4696 objects, 1006 of which are confirmed[1] (cf., Fig 1.6). The distribution of planetary radii starts from Mars-like planets, up to a few times the size of Jupiter. The majority of the confirmed and planet candidates are Neptune-Sized objects (Borucki et al. 2011) .

An important contribution of the *Kepler* mission is the detection of a very large number of multiple planetary systems. Lissauer et al. (2012) and Lissauer et al. (2014) confirmed statistically that the

[1] According to the NASA Exoplanet Archive

majority of the multi planet candidates are real planets. Due to the gravitational interactions of the component of such multi planet systems, it is possible to study them with the TTV method and extract valuable informations for the system (Fabrycky et al. (2012), Steffen et al. (2013) etc.). Mazeh et al. (2013) extended this research, searching for TTVs in the total catalog of *Kepler* Objects of Interest (KOI).

The use of TTVs is not coming without problems though, especially in the cases of active stars. There are reports of low-amplitude TTVs, which are assumed to be caused by starspots in the transits (Sanchis-Ojeda et al. (2011), Fabrycky et al. (2012), Szabó et al. (2013), Mazeh et al. (2013)). In an attempt to explain the ∼3 min TTVs of the planet WASP-10 b, Barros et al. (2013), simulated the impact of such spot-crossing events on the TTVs measurements, while a more general approach was made by Oshagh et al. (2013), including a variety of configurations between the starspot and the planet.

As with the *CoRoT* data, the *Kepler* light curves are ideal for activity research likewise, as there are plenty of stars with modulations caused by the rotation of spots (Walkowicz & Basri 2013). An interesting approach to measure the differential rotation of active stars is presented by Reinhold et al. (2013), where they propose the use of the generalized Lomb-Scargle periodogram, in order to measure differential rotation, instead of a spot model.

Due to a computer failure, the *CoRoT* satellite is out of order permanently. In the same fashion, hardware problems on the *Kepler* satellite forced for reorganization of the observational strategy, ending the main observation phase and starting the K2 phase. The forthcoming missions, PLATO (Rauer et al. 2014) and TESS (Ricker et al. 2015), are meant to continue the high accuracy observations, in search of extrasolar planets.

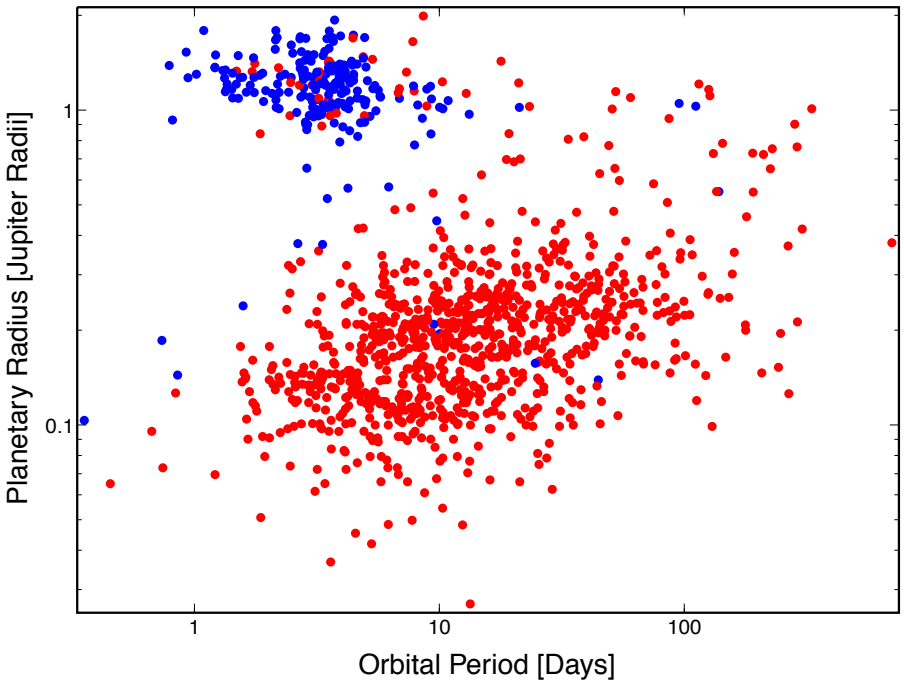

Figure 1.6: The contribution of the *CoRoT* and *Kepler* spaces missions in the discovery of transiting planets (red dots) in comparison to ground-based surveys (blue dots), according to the htp://exoplanets.org as of Dec. 2015

1.5 High speed photometry

The photometric accuracy of the time series produced by space-based telescopes proved to be 2 to 3 orders of magnitude better from equivalent ground-based telescopes. The profound reason for this discrepancy is the existence of the Earth's atmosphere and more specifically the, also known since antiquity, "twinkle" or scintillation of the stars.

The stars are twinkling due to wavefront curvature of the upper atmosphere. As a result, the light of any source that arrives in any photon collecting device, presents fluctuation in millisecond intervals. According to Reiger (1963) $\sim$ 70% of the of the amplitude of the intensity fluctuations originate to perturbations of the incoming wavefront, in the altitude of 7 to 15 km. The impact of those fluctuations in the time series is the introduction of correlated (red) noise, in addition to the present photon (gaussian) noise of the light curve.

Until the present day, a way to "fight" scintillation is the collection of a large number of photons, using very large telescopes (e.g. GTC, Keck, SALT, LBT, VLT etc.), in time intervals far from the millisecond regime. Nevertheless and despite the obvious advantages, such massive structures are very expensive to built and maintain. In addition, the wide spectrum of applications that those telescope offer, increases the demand for observational time. As a result the usage of such instruments is limited to very well pointed studies, eliminating the chances for more general studies such as surveys.

But, is there another way to beat scintillation? The first step in order answer this question was made, with a series of papers, by D. Dravins and colleagues (Dravins et al. (1997a), Dravins et al. (1997b) and Dravins et al. (1998)). In their work they attempt to unveil the statistical characteristics of scintillation, using a variety of telescopes equipped with photomultipliers and they concludes that the intensity of autocorrelation is aperture dependent for small apertures ($\simeq$ 5 cm) and the delay of its maximum value varies between 1 ms and 10 ms. Also they noticed that the frequency of the scintillation fluctuations becomes smaller for longer wavelengths.

Although, the photomultipliers are exceptional for scintillation studies, they suffer from a great disadvantage; their spatial resolution. Due to their construction, the photomultipliers are unable to spatially resolve the collected photons (i.e. they cannot create 2D images). Consequently, the observation of more than one sources simultaneously through the same optical instrument, is impossible. As a result, the cross correlation studies of the scintillation fluctuations of different objects, suffers from additional systematic errors due to the usage of different telescope-photomultiplier couples for each source.

Due to the advance of the silicon charge-coupled devices (CCD), which can store photons in N x N arrays of pixels and not in only one pixel, the photomultipliers were put aside. Yet, this property of the CCDs makes them inappropriate of scintillation studies, due to the time that it is needed for the read out (the process of the digitization of the stored electrons). Thus, the scintillation studies were stalled.

Hence, the second step towards beating scintillation noise was made, indirectly, by Qiu et al. (2013), with the introduction of complementary metal-oxide semiconductor (CMOS) devices for scientific astronomical use. In a CMOS chip every row of pixels has its own analog to digital converter. This allows each row to perform the readout procedure, while the other rows are still exposing (rolling shutter mode). Due to that function a CMOS camera has readout times to sub-millisecond regime.

1.6 Outline

The main focus of my research lies on the detection and characterization of extrasolar planets, with the method of transits. The study of those objects enables us to measure many of their characteristics and thus to create an impression about the planet formation and planetary population in our galactic neighborhood. Driven by this idea, I studied the structure of the multiple system Kepler-210, which was detected by the *Kepler* mission (see, Sect. 2). The main structure of the paper was conceived by me, in collaboration with my supervisor Prof. J.H.M.M Schmitt and some help from C. von Essen. The system stability analysis was performed by Ch. Avdellidou and by me. Finally, the TTV analysis was carried out by python scripts, written by me around the source code of Prof. E. Agol, for the computation of transit times and radial velocities of an N-body system.

The host star demonstrates periodic modulations with amplitude on the range of ∼2 % of its total flux. The most prevalent interpretation about the origin of those variations is the assumption that they are being caused by starspots. During the process of the determination of the characteristics of the planets Kepler-210 b & c, the question of "how much would the starspots affect the transit light curves?" emerged. The lack of an extended study on that subject motivated me to investigate the impact of spot crossing events, for a variety of star-planet configurations, on the measured TTVs. The published paper is presented in Sect. 3. The paper was written in collaboration with all authors. The simulations for the single transit study were performed with python scripts, written by me. K.F. Huber performed the simulations of the consecutive transits analysis, with his own algorithm, in an effort to validate the correctness of our analysis.

The active planet hosts are usually considered as "annoying" and difficult to study. As a result such system are avoided. A great example of this behavior is the exclusion, from the Kepler field, of the majority of the active stars. The motivation for my research so far is the understanding of the effects which the activity of a star can have on the transit light curves of its planets, in order to study them with the less possible uncertainty. Therefore, I fit the modulations of the Kepler-210 star with a five spot model, varying the starspot positions and sizes. In combination with other established methods I find calculate the differential rotation of the star and the life-time of the spots. Furthermore I identify preferably active longitudes and evidence of magnetic activity cycles. The submitted for publication paper is presented in Sect. 4.1). The full study is based on ideas both by me and by Prof. J.H.M.M Schmitt.

In Sect. 4.2 I use the method of unsharp masking to investigate the photometric light curves of planets with ambiguous TTVs and to compare the features in their $O-C$ diagram with the occurrence and in-transit positions of spot crossing events. As a proof of concept I apply this method to the light curve and the estimated eclipse timing variations of the eclipsing binary KOI-1452, for which I prove their non-gravitational nature. Furthermore, in collaboration with Prof. J.H.M.M Schmitt, we use the same method to study the rotation properties of the primary star of the system KOI-1452 and to show that the spots responsible for the timing variations rotate with different periods than the most prominent periods of the system's light curve. We argue that the main contribution in the measured photometric variability of KOI-1452 originates in g-mode oscillations, which makes the primary star of the system a γ-Dor type variable candidate.

Finally, I present the efforts for the design and operation of a fast photometry telescope, with main goal the study of scintillation effects in the light curves of multiple stars. To this end, I use a Zyla

4.2, sCMOS camera, mounted on the first focus of a Celestron 14 (14") optical tube. This equipment configuration allows for the observation of many targets simultaneously, using very high frame rates (∼100 fps). As is shown in Sect. 5, the scintillation study results show that with additional, systematic, observations it is possible to effectively increase the precision of ground-based observations, with small telescopes. In addition, the high frame rate in combination to the wide field of the fast imaging telescope, render it ideal for high precision measurements on bright variable stars. The idea for this experiment and the equipment configuration, belongs to Prof. J.H.M.M Schmitt. I carried out the observations and the photometry, along with the time series analysis, with the contribution of the B.Sc. student T. Klause and M.Cs. student Ch. Blohm.

1. Outline

Chapter 2

The planets around the active star Kepler-210

2.1 "*Kepler-210: An active star with at least two planets.*", P. Ioannidis, J. H. M. M. Schmitt, Ch. Avdellidou, C. von Essen and E. Agol AA, v. 564, A33, (2014)

2.1.1 Introduction

Since the launch of the *Kepler* Mission in 2009, a large number of planetary candidates has been found using the transit method in the high precision *Kepler* light curves. Specifically, 2321 planetary candidates in 1790 hosts stars have been reported, from which about one third are actually hosted in multiple systems (Batalha et al. 2012). The majority of these *Kepler* planetary candidates are expected to be real planets (Lissauer et al. 2012) and therefore those stars present an excellent opportunity for a more detailed study and characterization through the method of transit timing variations (TTVs). Ever since the first proposals of the method by Agol et al. 2005 and Holman & Murray 2005, TTVs have been widely used to search for smaller, otherwise undetectable planets in systems containing already confirmed planets. In multiple systems this method can be applied in order to confirm the physical validity of the system along with a rough estimate of the components' mass, which can otherwise be obtained only through radial velocity data. For the *Kepler* candidates the *Kepler* team has carried out and reported this kind of analysis for 41 extrasolar planet systems. For the last announcement of the series see Steffen et al. 2013.

In this paper we present our in-depth analysis and results for a particular system, Kepler-210 (=KOI-676), which was previously identified and listed as a planet host candidate in the catalog by Borucki et al. 2011. The specific characteristics of Kepler-210 that enticed us to perform a detailed study of this candidate system were the high activity of its host star coupled with the fact that the system harbors two transiting planets, which we validate using spectral and TTVs analysis, as well as stability tests.

The plan of our paper is as follows. In the first section we describe the methods used to determine the stellar and planetary properties. In the second section we discuss various scenarios to explain the detected discrepancies in the orbital elements of the planets. Furthermore, we describe the results of our TTVs analysis for both planets, and finally, we summarize with what we believe is the most probable scenario.

2.1.2 Data analysis

2.1.2.1 Stellar activity

The *Kepler* data of Kepler-210 were obtained from the STDADS archive and contain the data

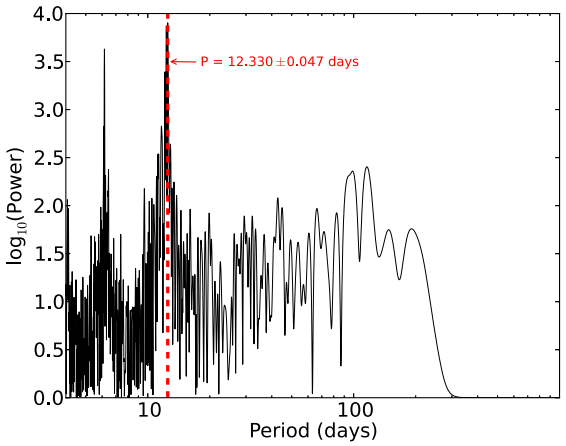

Figure 2.2: The Lomb-Scargle Periodogram for the raw light curve as logarithmic power (on y axis) vs. period. A polynomial fit was applied to remove systematics related to the rotation of the telescope.

recorded in the quarters Q1 to Q12. To achieve bet-

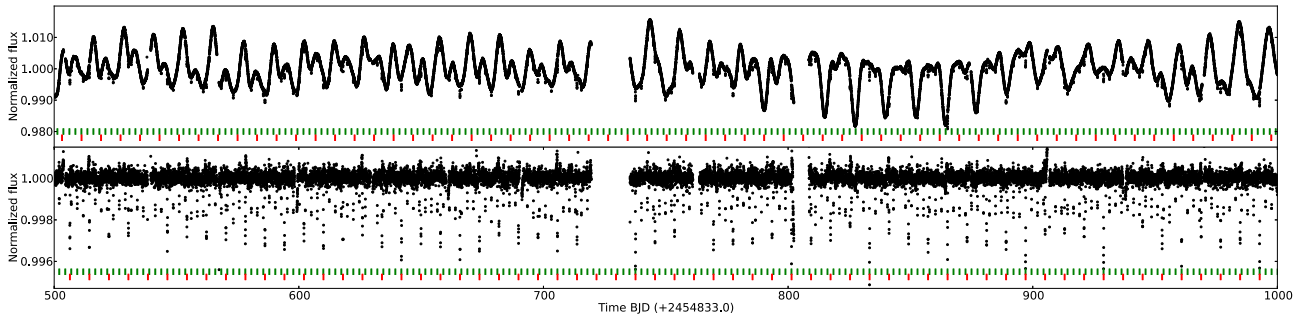

Figure 2.1: A fraction of the Kepler-210 light curve. Top: Part of the raw light curve demonstrating the activity of Kepler-210. Bottom: The transits of planet a (green) and b (red) for that particular time, with the stellar activity removed by using the kepflatten routine of the Pyke package for pyraf.

ter temporal coverage we used both long and short cadence data. We decided to use the SAP data for our analysis to avoid any artifacts introduced by the use of SAP_PDC data, given the obvious complexity of the Kepler-210 light curve (cf., Figure 2.1). Clearly, the host star of the Kepler-210 system is of particular interest by itself.

To give an impression of the activity of Kepler-210, a part of the overall *Kepler* light curve of Kepler-210 covering 500 days is shown in Fig. 2.1. Peak-to-peak variations on the order of 2% can easily be identified on time scales of a few days, and in addition, variations on longer time scales are also visible. To assess the dominant time scales of variability we computed a Lomb-Scargle periodogram over the full available data set, which we show in Fig. 2.2. Two peaks are clearly observable in the resulting periodogram. We interpret the most significant peak at 12.33 $\pm$ 0.15 days as the rotation period of the star, while the second, smaller peak at 6.15 $\pm$ 0.047 days is interpreted as an alias from the 12.33 day rotation period. We further note that both peaks are quite broad, with significant power residing at frequencies near the peak frequency.

2.1.2.2 Data Preparation

For our transit and TTVs analysis we must remove all effects of stellar activity as much as possible. In order to rectify the *Kepler* light curve of

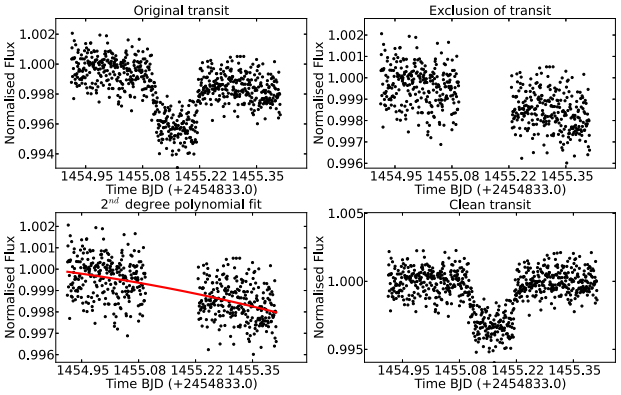

Figure 2.3: Demonstration of stellar activity removal procedure; see text for details.

Kepler-210 we proceed as follows: For each transit of each planet we select some part of the light curve centered at the estimated mid-transit time, including data points before and after ingress and egress, respectively (see Fig. 2.3, upper left). The obvious transit points are then removed (Fig. 2.3, upper right) and a second order polynomial fit is applied to the remaining data points (see Fig. 2.3 lower left). Finally, all selected data points including those obtained during transit are divided by the result of the polynomial fit (see Fig. 2.3 lower right) and we obtain a rectified light curve, normalized to unity for the data prior to the first and after the fourth contact.

Kepler-210	
KIC-ID	7447200
KOI-ID	676
T_{eff}	4300 K
logg	4.55
$R_\star$	0.69 $R_\odot$
$M_\star$	0.63 $M_\odot$
linear LD	0.7181
quadratic LD	0.0443

Table 2.1: Stellar parameters of Kepler-210 taken from Batalha et al. 2012. The limb-darkening coefficients where calculated for those values from Claret et al. 2012 for those parameters.

Planet	b	c
Period (d)	2.4532 ± 0.0007	7.9725 ± 0.0014
T_0 (LC)	134.0952 ± 0.0002	131.7200 ± 0.0002
$R_{pl}/R_\star$	0.0498 ± 0.0004	0.0635 ± 0.0006
$a/R_\star$	4.429 ± 0.077	11.566 ± 0.323
i	77.86 ± 0.26	85.73 ± 0.16
b	0.931 ± 0.038	0.861 ± 0.065
transits	431 lc / 243 sc	97 lc / 51 sc

Table 2.2: MCMC analysis transit model fit results and their "1 σ" errors.

In this fashion we prepare the transit data for both planets for an application of our transit model fit; we consider only transits by one planet and exclude any simultaneous transits from our analysis.

2.1.2.3 Model fitting

The effects of the host star's stellar activity are clearly visible also in the transit light curves, which are twofold: (see Figure 2.1): Star spots occulted by the planet on the one hand lead to bumps in the light curve as shown by Wolter et al. 2009, while star spots on the unocculted face of the star on the other hand lead to variable transit depths. Thus, both effects increase the dispersion of the transit data and the incorrect normalization leads to incorrect stellar and planetary parameters. In order to minimize the effects of stellar activity we therefore decided to use transits, following the following two rules:

1. We select those transits occurring close to maximum flux in the activity modulations, which corresponds to smaller spot coverage of the stellar surface
2. We model each transit separately, isolated the transit data and measure the χ^2-test statistics. Only the transits with acceptable fits are selected.

Thus, for the transit model fit of the inner planet 89 transits were used, while for the outer planet a total of 10; we rejected 154 transits by the inner planet and 41 transits by the outer planet for this analysis. To determine the best fit model we used the analytical transit light curve model by Mandel & Agol 2002 and Markov-Chain Monte-Carlo sampling[1] for the computation of the fit parameters and their errors. In this process we used the limb darkening coefficients for the model as calculated by integrating the values of the Claret catalog (Claret et al. 2012) for the parent star's nominal parameters T_{eff}, $logg$ and $[Fe/H]$ listed in Table 2.1 .

2.1.2.4 Fit results

In Figs 2.4 and 2.5 we show the full sample of the derived mean normalized *Kepler* transit light curves and our best fit model (red line; upper panel), the fit residuals for all data points (middle panel) and the mean values of the individual residuals as well as for blocks of twenty adjacent phase points (lower panel). The physical parameters

[1] http://www.hs.uni-hamburg.de/DE/Ins/Per/Czesla/PyA/PyA

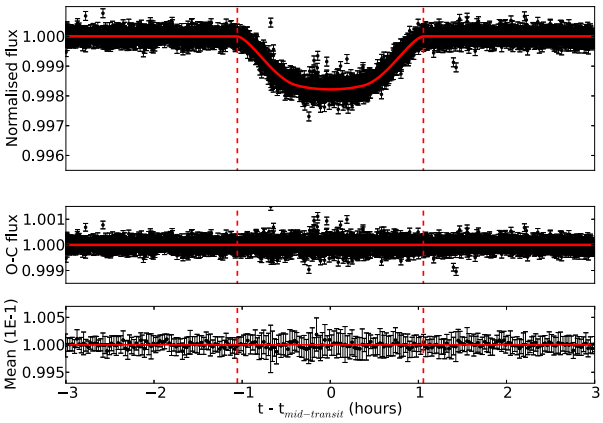

Figure 2.4: The folded lightcurve of planet b, using the total number of transits and the best fit model. The lower diagram shows the model residuals binned, which in this case is less obvious than in case of planet c (see Fig. 2.5.

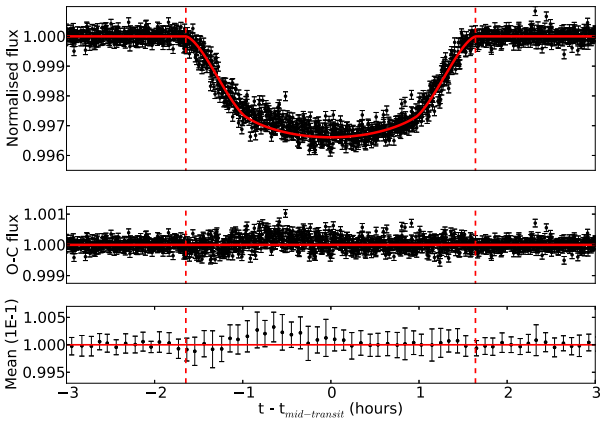

Figure 2.5: The folded light curve of planet c, using the total number of transits and the best fit model. The transit profile is affected by spots during and after ingress.

derived from our transit analysis are listed in Table 2.2; note that the inner, shorter period planet is smaller than the outer planet.

2.1.3 Transit Timing Variations

2.1.3.1 Timing variation analysis

After completion of the transit model fit procedure and the determination of the global parameters for each planet, we recalculated the mid-transit times for all transits of each planet, i.e., also those that had been rejected for the best model fit. To that end we reapplied the MCMC fitting algorithm for every transit separately, keeping all model parameters fixed except for the individual mid-transit times $t_{MT,i}$ $i = 1, N$. From the observed mid-transit times $t_{MT,i}$, their errors σ_i and the integer transit epochs N_i we derived a mean period P and time reference T_0, by minimizing the expression

$$\chi^2 = \sum_{i=1}^{N} \frac{(t_{MT,i} - t_{calc,i})^2}{\sigma_i^2} \Rightarrow$$

$$\chi^2 = \sum_{i=1}^{N} \frac{(t_{MT,i} - P\ N_i - T_o)^2}{\sigma_i^2} \Rightarrow$$

$$\chi^2 = \sum_{i=1}^{N} \left(\frac{OC_i}{\sigma_i^2} \right)^2 \quad (2.1)$$

with respect to P and T_0; the thus resulting O-C diagrams for planets b and c are shown in Fig 2.6; the appropriate data for the creation of those diagrams are available in electronic form at the CDS via anonymous ftp to cdsarc.u-strasbg.fr (130.79.128.5) or via http://cdsweb.u-strasbg.fr/cgi-bin/qcat?J/A+A/

2.1.3.2 TTVs results

While in the O-C diagram of planet b (Fig. 2.6) some modulation is visible, no clear variation is apparent for planet c. In order to assess to what extent TTVs might be caused by stellar activity, as for example the observed anomaly in the ingress of the transit of planet b (Fig. 2.4), we calculated the transit times using two different approaches, additional to the one described in 2.1.3.1:

- We recalculated the transit times using the method described in 2.1.3.1, but by excluding the affected areas of the transit phase.

- We used the analysis described by Carter & Winn 2009 in order to remove the spot anomalies, considering them as red noise.

The results in both cases were almost identical, thus we decided to use for our analysis the transit times which were produced with the simplest method (section 2.1.3.1). In addition we searched for correlations between the timing variations vs. the transit depth and duration, but in any case no correlations were found.

In order to quantify the significance of the observed O-C variations, we carried out a χ^2-analysis on the null hypothesis that there are no timing variations, on the long and short cadence data separately and on the joined long and short cadence data. We also carried out the same analysis by averaging the measured O-C values over ten consecutive epochs; the respective χ^2-values and the derived significance levels are listed in Table 2.3.

An inspection of Table 2.3 shows that the unbinned long cadence data show no evidence for any non-zero O-C values, while the short cadence data do; binning does greatly increase the significance of the non-zero O-C values.

Since the values of the χ^2-test statistics sensitively depend on the measurement errors σ_i, we carefully checked the errors of the derived mid-transit times by using two independent methods and convinced ourselves of the internal consistency of our error determination. In addition we checked that the derived χ^2-values are not produced by a few individual outliers. As a result we are confident that the observed TTVs are statistically significant.

2.1.4 Discussion

2.1.4.1 Examination of stellar properties

In order to better determine the stellar parameters of Kepler-210, a high resolution spectrum was acquired, using the CAFE instrument on the 2.2 m telescope of the Calar Alto Observatory in Spain. For our analysis we also used two spectra of Kepler-210, taken from the CFOP[1] web page. We specifically inspected the spectra for a second set of lines indicating the existence of a close unresolved companion but found none. For the same purpose we also examined the pixel area around the star using the Kepler target fits frames, but found again no evidence of any variable star in the vicinity of the central star that could create a contaminating signal.

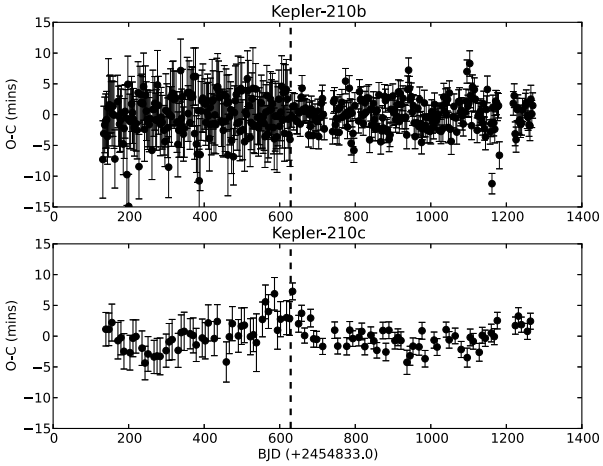

Figure 2.6: The O-C diagrams of planet b (upper panel) and c (lower panel), along with the best fit models. The dashed line discriminates the long from the short cadence data.

To measure the color index B-V, we observed Kepler-210 together with with two standard stars (HD 14827 and HD 195919), using the 1.2 m Oskar-Lühning-Telescope (OLT) from Hamburg Observatory and found B-$V_{Kepler-210} = 1.131 \pm 0.064$, consistent with the color derived from CFOP (1.088 ± 0.037) and other sources; thus the spectral type of Kepler-210 is in the late K range.

We then proceeded to estimate the stars age using the gyrochronology expression 2.2 derived by Barnes 2007

$$\begin{aligned} log(t_{gyro}) &= \frac{1}{n}\{log(P) - log(\alpha) \\ &- [\beta \cdot log(B - V - 0.4)]\}, \quad (2.2) \end{aligned}$$

[1] https://cfop.ipac.caltech.edu

Table 2.3: The null hypothesis χ^2 results with their P-values for the long cadence alone (left column) vs the short cadence alone (middle column) and the combined long and short cadence data (right column) for unbinned and binned data. In the square brackets are listed the degrees of freedom.

	Long Cad.	Short Cad.	L & S Mix
b	430.6 (0.47) [430]	347.5 (>0.99) [242]	447.9 (0.71)
c	111.6 (0.77) [96]	138.7 (>0.99) [50]	185.2 (>0.99)
b_{bin}	61.2 (0.88) [43]	63.5 (>0.99) [24]	47.5 (0.67)
c_{bin}	51.9 (>0.99) [10]	76.1 (>0.99) [5]	67.9 (>0.99)

where t is in Myr, B-V is the measured color, P (in days) is the rotational period, $n = 0.5189$, $\alpha = 0.7725 \pm 0.011$ and $\beta = 0.601 \pm 0.024$. By using Eq. 2.2 with P = 12.33 days and the B-V = 1.131, we estimate an age of 350 ± 50 Myrs for Kepler-210; this estimate appears reasonable given its high degree of activity.

2.1.4.2 Mean stellar density

When a planet is transiting in front of its parent star, we have the opportunity to accurately derive the ratio between the stellar radius $R_\star$ and the orbital semi-major axis a (cf., Table 2.2). Combining this information with Kepler's third law, we can compute an expression for the mean density ρ_{mean} of the host star through

$$\varrho_{\star,mean} = \frac{3\pi}{G}\frac{a^3}{R_\star^3\ P^2}, \tag{2.3}$$

with G denoting the gravitational constant in addition to the terms containing only the observed quantities a/R$_\star$ and period P. The value for a/R$_\star$ is derived from the transit modeling, given the large number of transits, for both planets, the values of a/R$_\star$ and P can be estimated with relatively high accuracy. Carrying out this computation using the observed parameters for planets b and c (cf., Table 2.2) we obtain densities of $\varrho_{\star,b} = 0.27 \pm 0.004$ g/cm^3 and $\varrho_{\star,c} = 0.46 \pm 0.038$ g/cm^3 , respectively for the host. On the other hand, based on the nominal stellar parameters of the host star we expect a mean density of $\varrho_o \approx 2.6$ g/cm^3. Thus the mean host star densities derived from planets b and c are, first, inconsistent with each other, and second, differ by almost an order of magnitude from the expected host star density. Since we firmly believe in Kepler's third law, there must be a physical explanation for both discrepancies.

2.1.4.3 Ellipticity of planetary orbits

So far our analysis has implicitly assumed circular orbits for both planets. For elliptical orbits the orbital speed and hence the transit duration change during the orbit and therefore there is no unique relation between transit duration and stellar and planetary dimensions. Assuming that the orbital velocity is constant during the actual transit, Tingley & Sackett 2005 relate the transit duration D_{ell} to the period P and the impact parameter b of a transit through the expression

$$D_{ell} = \frac{\sqrt{(1-e^2)}}{1+e\cdot cos(\phi_t)}\frac{P}{\pi}\frac{\sqrt{(R_\star+R_{pl})^2-b^2)}}{a}, \tag{2.4}$$

where ϕ_t denotes the true anomaly at the mid-transit, while $R_\star$, R_{pl} and a, denote stellar and planetary radii and semi-major axis respectively. Consequently, the transit duration D_{ell} of an elliptical orbit scales with the transit duration D_{circ} of a circular orbit (for the same system geometry and the same period) through

$$D_{ell} = \frac{\sqrt{(1-e^2)}}{1+e\cdot cos(\phi_t)} \times D_{circ} = g(e, cos(\phi_t)) \times D_{circ}. \tag{2.5}$$

It is straightforward to convince oneself that the derived sizes for star and planet scale with the scaling function $g(e, cos(\phi_t))$ introduced in Eq. 2.5. Since the mean stellar density scales with $R_\star^3$, we find

$$\varrho_{\star,ell} = \varrho_{\star,circ} \cdot \left(\frac{\sqrt{1-e^2}}{1+e\cdot cos\phi_t} \right)^{-3} \tag{2.6}$$

with $\varrho_{\star,circ} = \varrho_{\star,mean}$ from Eq. 2.3. Hence the discrepant stellar densities can be explained by introducing suitable eccentricities and true transit anomalies. By solving 2.6 for different values of e and ϕ_t it is thus possible to to constrain the range of permissible eccentricities as well as values for ϕ_t, for which the derived stellar density becomes equal to the density expected for the spectral type of the star for both planets; the corresponding curves are shown in Fig. 2.7, where we plot for each planet the combination of e and ϕ_t resulting in a nominal stellar density of 2.7 $g\ cm^{-3}$. Fig. 2.7 shows that eccentricities of 0.4 (for planet b) and 0.5 (for planet c) are required to produce the expected stellar densities.

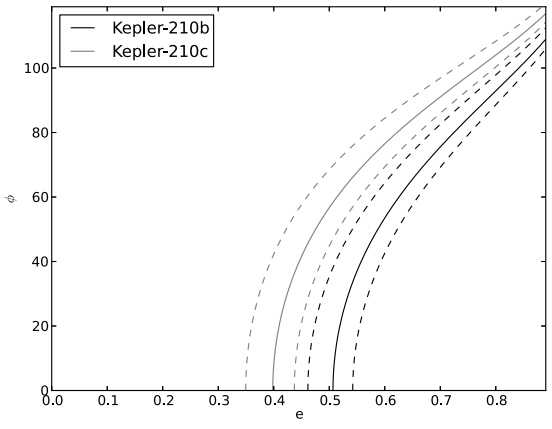

Figure 2.7: Contour plot of eccentricity versus true anomaly during the mid-transit (ϕ). For a circular system (e = 0) the density should equal $\varrho_o \backsimeq 2.6\ g/cm^3$, as can be calculated for the given values of $R_\star$ and $M_\star$. The derived from the $a/R_\star$ values of $\varrho_\star$ for the planets Kepler-210b (black line) and Kepler-210c (gray line) can be explained for eccentricities $\gtrsim 0.4$ and $\gtrsim 0.51$ respectively, depending on the true anomaly of the planet during the mid-transit. The dashed lines represent the uncertainty limits.

2.1.4.4 Second (third) light scenario

Despite the fact that neither the optical spectrum nor the centroid analysis of the *Kepler* data have shown any evidence for a companion or blend, it might still be possible that some third object in the background or foreground with flux F_3 contributes to the system flux in a way that the observed total flux F_{obs} is given by

$$F_{obs} = F^\star + F_3, \tag{2.7}$$

where $F^\star$ is the desired planet host's flux, which has to be used for the transit modeling. If this hypothetical third light contribution F_3 is substantial, the true transit depth d_{true} would be underestimated and an incorrect radius for the Kepler-210 host star would be derived. Assuming that the limb darkening coefficients are identical and equal to the values presented in Table 2.1 for all system sources, we calculate the influence of the third light source on the derived stellar density (as shown in Fig. 2.9), considering the following non-linear system of equations, which allows computing the stellar and planetary radii (each scaled by the semi-major axis) $\tilde{R}_\star$ and $\tilde{R}_p$ and, i, the inclination of the orbit normal with respect to the line of sight, given the observed period P, the observed time between the first and forth contact, T_{14}, the time between the second and third contact, T_{23} and the observed (relative) transit depth at mid-transit d_{obs}:

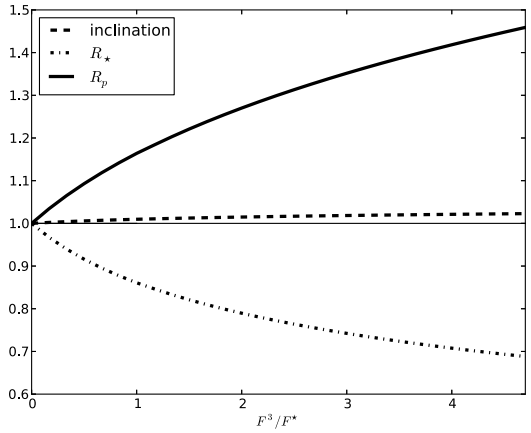

Figure 2.8: The variation of inclination, $R_\star$ and R_p, assuming third light interference F^3 for Kepler-210c

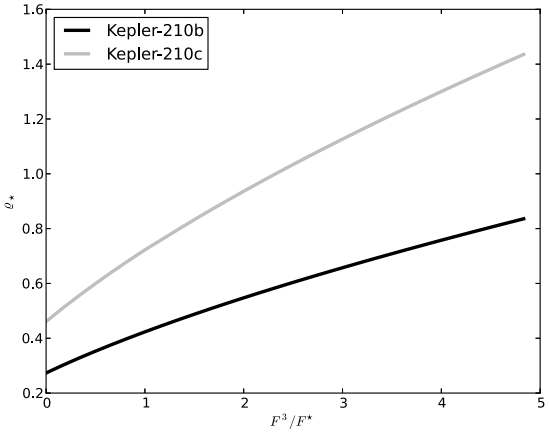

Figure 2.9: Derived stellar density versus assumed third light contribution F_3

$$sin^2 i\, cos^2\left(\frac{\pi}{P}T_{14}\right) = 1-(\tilde{R}_\star+\tilde{R}_p)^2 \quad (2.8)$$

$$sin^2 i\, cos^2\left(\frac{\pi}{P}T_{23}\right) = 1-(\tilde{R}_\star-\tilde{R}_p)^2 \quad (2.9)$$

and

$$d_{true} = \frac{(1-c_1-c_2)+(c_1+2c_2)\,\mu_c - c_2\mu_c^2}{1-\frac{c_1}{3}-\frac{c_2}{6}}\left(\frac{\tilde{R}_p}{\tilde{R}_\star}\right)^2 \quad (2.10)$$

Here c_1 and c_2 denote the quadratic limb darkening coefficients and μ_c denotes the expression

$$\mu_c = \sqrt{1-\frac{cos^2 i}{\tilde{R}_\star^2}}. \quad (2.11)$$

We clearly need the true transit depth d_{true} to compute the values of $\tilde{R}_\star$, $\tilde{R}_p$ and i, yet only the observed transit depth d_{obs} is available; the two depths are related, however, through

$$d_{true} = (1+d_{obs})\frac{F_3}{F^\star}. \quad (2.12)$$

Therefore, given the observed values of d_{obs}, T_{14} and T_{23} and the observed periods P for both planets, the derived values for $\tilde{R}_\star$ and hence $\varrho_\star$ will depend on the assumed third light contribution $F_3/F^\star$. The resulting system of equation is quite non-linear. In order to provide a feeling on how sensitive the solutions depend on the third light contribution $F_3/F^\star$, we plot in Fig. 2.8 the variation of the derived values for the inclination and stellar and planetary radii (for the planet Kepler-210c), relative to the case of no third light. As is clear from Fig. 2.8, the inclination increases only slightly (it cannot exceed 90 degrees), while the stellar radius decreases (as desired) and the planetary radius increases. Finally, we can derive the stellar density, for which our results are shown in Fig. 2.9, where we plot the derived stellar densities for both planets as a function of the assumed third light contribution $\frac{F_3}{F^\star}$. As is clear from Fig. 2.9, the third light contribution would have to be substantial, and in fact the third light would have to dominate the total system flux in order to obtain values of $\varrho_{\star c}$ as expected for stars on the main sequence in the relevant spectral range. Yet, the two planets still yield discrepant densities of their host, so one would have to introduce yet another host for the second planet, which appears at least a little contrived. Therefore we conclude that the introduction of a third light source does not lead to a satisfactory solution of inconsistency in the derived

stellar parameters.

2.1.4.5 Inflated star

Another possible scenario explaining the *Kepler* observations of Kepler-210 would be the assumption that the host is not on the main sequence, but rather evolved and in fact a giant or sub-giant. Such stars are usually not active, however, there are some classes of evolved stars which are quite active, for example, variables of the FK Com type. Those stars are highly active G-K type sub-giant stars with surface gravities log(g) of ~ 3.5. They show strong photometric rotational modulations caused by a photosphere covered with inhomogeneously distributed spots. An other important characteristic of these objects is their rapid rotation. Generally the $v\,sini$ derived from their spectra is between ~ 50 and 150 $km \cdot s^{-1}$ (Berdyugina 2005). In the case of Kepler-210 $v\,sini$ is ~ 4 $km \cdot s^{-1}$, and thus we believe that a FK-com scenario does not provide a suitable explanation for the observed density discrepancy.

2.1.4.6 Kepler-210 TTVs

As described in sec. 2.1.3, TTVs are detected in both planets. In order to further examine the properties of these variations we searched for any periodicities in the O-C data by constructing a Lomb-Scargle periodogram on every set. For the outer and larger planet, the Lomb-Scargle periodogram shows a leading period of about 690 days, which is apparent in the modulation of the O-C curve in Fig. 2.6, while for the inner and smaller planet the periodicity results remain ambiguous, most probably due to the large scatter in its O-C diagram.

What would be a physical scenario consistent with these O-C diagrams? We first note that the orbital period ratio of the system is very close to a 13/4, if we consider that the errors in periods in Table 2.2 are also affected by the TTVs. This ratio is not close to any low order mean motion resonance so the amplitude of any TTVs is expected to be relatively small for both planets (Agol et al. 2005).

In order to verify this and to model the TTVs we use the N-body code as presented in the same paper. The N-body code requires the planetary masses which are unknown. Assuming ad hoc that the planetary densities are below 5 g/cm^3, it is clear that the masses of the two planets are substantially below 0.5 M_J. Furthermore, in order to roughly estimate the planetary masses below that limit, we use a general mass vs. radius law as described by Lissauer et al. 2011 in the form

$$M_p = R_p^{2.06} \tag{2.13}$$

With the masses thus specified, we first considered only the two transiting planets for our TTVs simulations. Assuming non-eccentric orbits resulted in TTVs of less than a minute, which is far from the observed variations for both planets. The TTVs would remain in that state even if we assume higher masses, under the limit of 12 M_J. As discussed in detail by Lithwick et al. 2012, the TTVs amplitude can also be affected by eccentricity. Implementation of eccentric orbits for both planets, Kepler-210b and Kepler-210c, improved the fit substantially; the modeled TTVs together with the data are shown in Fig. 2.10, the fit results in terms of fit quality measured through χ^2 are given in Table 2.4.

Clearly, also the TTVs analysis supports a scenario of two planets with rather eccentric orbits similar to our discussion in 2.1.4.3. However, in order to produce the observed TTVs the system configuration must be such that the true anomaly, of both planets at the time of transit, ϕ_t, should exceed 40°, while also the difference in true anomaly $\Delta\phi_t$ should be $\sim 60°$, However, this configuration appears impossible due to the physical constraints in Fig. 2.7. Furthermore, our stability tests, (which performed with the **swift_rmvs3** algorithm (Levison & Duncan 1994), show that this configuration is unstable on time scales in excess of ~ 1 Myear. Finally we note that the probability of observing a

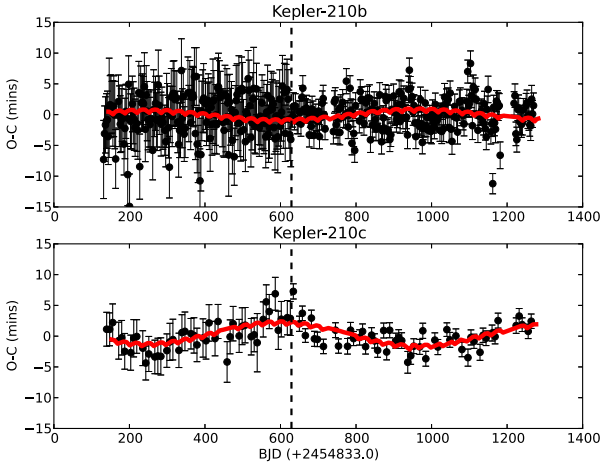

Figure 2.10: TTVs expected for two planets assuming eccentric orbits with $e_b = 0.44$ and $e_c = 0.50$.

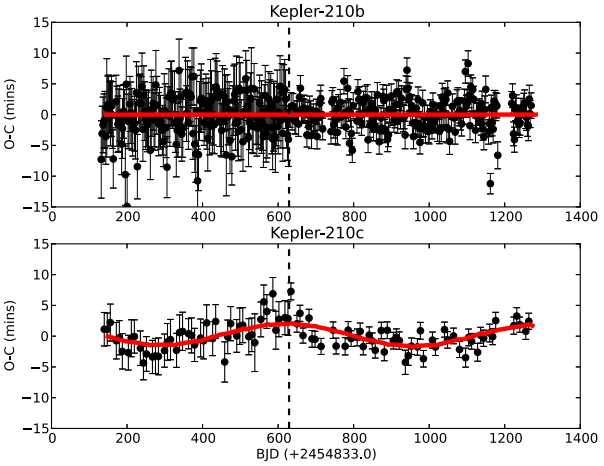

Figure 2.11: TTVs expected for three planets with non-eccentric orbits for all components of the system. The third planet's period for that case is P_{03}= 63.07 days.

transit is higher for small values of true anomaly, i.e., for the times near periastron passage.

We therefore conclude that a scenario with only two planets with eccentric orbits is unlikely and introduce a third, hypothetical planet KOI-676.03 in order to stabilize the system. We consider both eccentric and non-eccentric orbits for Kepler-210b and Kepler-210c. In order to determine period, mass and eccentricity for the hypothetical planet KOI-676.03, we considered several possible system configurations.

We emphasize that we cannot derive a unique solution for the physical parameters of this hypothetical planet. Most importantly, we need to assume a mass for this planet, which controls the strength of the gravitational interaction with the observed planets Kepler-210b and Kepler-210c. Thus, given the observed TTVs amplitude and

given the assumed mass of KOI-676.03, a certain value of semi-major axis and hence period is derived. The higher the assumed mass, the longer the resulting period, and thus there is more than one configuration to account for the detected TTVs signal.

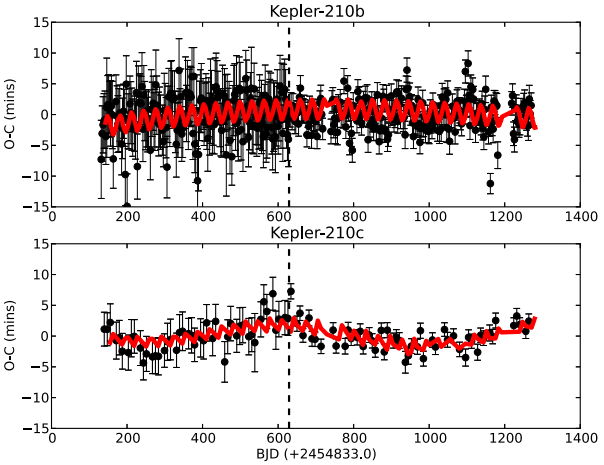

Figure 2.12: TTVs expected for three planets assuming eccentric orbits with $e_b = 0.45$, $e_c = 0.51$ and $e_{03} = 0.23$. The Third planet's period for that case is $P_{03} = 63.29$ days.

In order to produce possible candidate systems, we carried out simulations assuming some given mass for KOI-676.03, considering periods between 20 to 300 days, masses in the range $M_{03} \sim$ 0.1-0.6 M_J and eccentricities e $\simeq$ 0.1-0.3. A particularly promising configuration, but by no means unique solution, consistent with all *Kepler* data, has a period P $\simeq$ 63 days; in Fig. 2.11 and again Table 2.4

Table 2.4: χ^2 results of the model for 2 eccentric planets hypothesis, 3 non eccentric planets and 3 eccentric planets. In the square brackets are listed the degrees of freedom.

	2 ecc Planets	3 non ecc Planets	3 ecc Planets
b	489.57 [420]	447.9 [415]	443.9 [415]
c	116.22 [86]	112.4 [81]	117.59 [81]

(for the case with zero eccentricity) and in Fig. 2.12 and Table 2.4 (for the eccentric case) we show that such a scenario provides results consistent with the available *Kepler* data. As is clear from Fig. 2.11 and Fig. 2.12, as well as Table 2.4, the difference between the non-eccentric and eccentric case is marginal at best, while (statistically) preferable over a two planets scenario. In addition, the eccentricities of the planets Kepler-210b and Kepler-210c give a high frequency TTVs signal, which might better explain the higher dispersion of the TTVs in Kepler-210b. In that case the model also suggests ϕ_t values around zero with $\Delta\phi < 30$ °, which are in line with Fig. 2.7. Also the system's stability exceeds 10^7 years.

In the case of non eccentric orbits the system would reach fatal instability once masses above 5 M_J are chosen. For eccentric orbits the upper limit for the masses of the system becomes lower. While this fact suggests a planetary nature of the system components, it also introduces an additional factor of concern about the long term stability of the system. We do point out that this third stabilizing planet does produce a radial velocity signal in the system. For our nominal case we plot in Fig. 2.13 the expected RV signal in a synthetic radial velocity diagram, which shows peak-to-peak variations in excess of 60 m/sec; clearly such RV variations ought to be detectable despite the high activity level of the host star, and therefore, the detection of a RV-signal would significantly constrain the possible configuration space of the system.

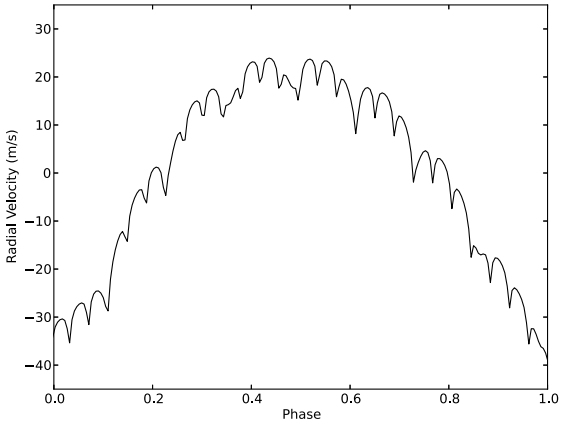

Figure 2.13: The predicted, synthetic, radial velocity diagram for the system Kepler-210 for P_{03} = 63 days, M_{03} = 0.4 M_j, e_{03} = 0.23 and $i_{03} = 60°$.

2.1.5 Summary

We report the detection and characterization of two transiting Neptune-sized planets, Kepler-210b and Kepler-210c with periods of 2.4532 days and 7.9723 days respectively around a presumably quite young and active K-type dwarf. These objects were first listed as planetary candidates by the *Kepler* team. We show that the transits of both planets are affected by spots. From the observed transit parameters and in particular from the observed value of $a/R_\star$ it is possible to calculate the mean density of the host star using the Kepler's 3^{rd} law. Interestingly, the two planets yield discrepant mean host star densities, which in addition are inconsistent with the densities expected for a K-type dwarf. Having explored various scenarios we conclude that the assumption of quite eccentric orbits for both planets provides the currently most probable scenario.

In addition, both planets show transit timing variations. Using N-body simulations we constructed possible system configurations consistent with the *Kepler* data. While it is possible to explain the observed TTVs with a two planet scenario, such

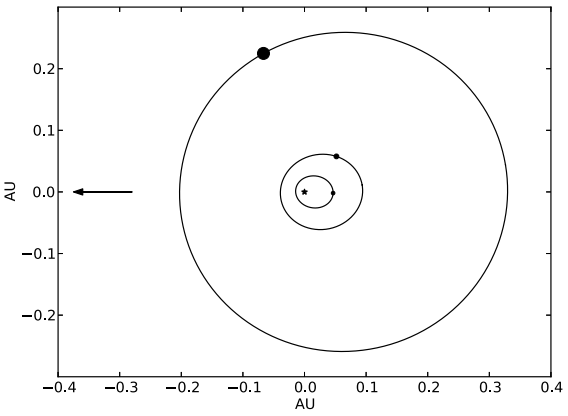

Figure 2.14: The suggested system configuration. The earth is at the direction of the arrow.

a scenario requires a very special geometrical configuration and is unstable on time scales of 10^6 years. As a result we believe that there exists a third planet, KOI-676.03, with a mass between $\sim$ 0.3-0.6 M_J in a slightly eccentric (e $\simeq$ 0.2) orbit with period $\sim$ 63 days, which stabilizes the whole Kepler-210 planetary system.

Different configurations are also possible, yet this stabilizing hypothetical planet should produce a detectable RV signal. We therefore suggest RV monitoring of Kepler-210, which is likely to provide a substantially increased insight into the Kepler-210 planetary system.

2. Ioannidis et al. (2014): *Kepler-210: An active star with at least two planets.*

Chapter 3

Transit Timing Variations and activity

3.1 "*How do starspots influence the transit timing variations of exoplanets? Simulations of individual and consecutive transits.*", P. Ioannidis, K. F. Huber and J. H. M. M. Schmitt AA, v. A72, 585, (2016)

3.1.1 Introduction

The transits of a planet in front of its host star contain a wealth of fundamental information both on the planet and its host star. Using mid-transit times and studying their variations it is possible to measure the gravitational interaction of additional bodies that orbit the same center of mass. These transit timing variations (TTVs) can be used to determine the masses of planets in a multi-planet system and can even be used to infer the existence of additional (even low-mass) companions as has been shown, for example, by Agol et al. (2005). Although masses and additional companions can also be inferred from precise radial velocity (RV) measurements, the importance of the TTV method increases for planets around faint stars where accurate RV measurements are difficult to obtain.

Depending on the actual system configuration, TTVs can reach differences with respect to the linear period ephemeris of up to a few hours, especially for systems close to low-order mean motion resonances (Nesvorný et al. 2013). Although the determination of TTVs is possible from ground-based observations, the high precision of the data from the *CoRoT* (Baglin et al. 2006) and *Kepler* (Koch et al. 2010) space missions, along with the possibility of uninterrupted sequences of transit observations, is better suited for this task and has provided evidence of statistically significant TTVs in about 60 cases.[1]

In addition, space-based photometry has shown that the light curve of a star can also be substantially disturbed by the effects of stellar activity. In particular, the transit profiles of planets with active host stars can be heavily distorted by dark spots as observed, for example, in Tres-1 b (Rabus et al. 2009) or CoRoT-2 b (e.g., Wolter et al. 2009, Huber et al. 2009). This effect can be severe enough to introduce large systematic errors in the determination of the physical parameters of the planets, which can greatly exceed the formal statistical errors (Czesla et al. 2009, Oshagh et al. 2013).

Recently, there have been reports of the detection of low-amplitude TTVs, which are assumed to be caused by starspot signatures in the transit profiles (Sanchis-Ojeda et al. 2011, Fabrycky et al. 2012, Szabó et al. 2013, Mazeh et al. 2013). A first approach to studying the effect of starspots on TTVs was therefore made by Barros et al. (2013) to explain the ∼3 min TTVs of the planet WASP-10 b, while a more general approach, including a variety of configurations between the starspot and the planet, was presented by Oshagh et al. (2013).

In this paper we simulate light curves of exoplanetary transits including spot-crossing events for a wider variety of the properties of the underlying star, starspot, and planet, and investigate the influence of these starspot signatures on the determination of mid-transit times. Furthermore, we study sequences of consecutive transits affected by starspots and evaluate the possibility of detecting a statistically significant signal in the TTVs that could mimic the TTV signal of a physical body.

The structure of our paper is as follows. In Sect. 3.1.2 we describe our approach for generating light curves in general, including our basic as-

[1] according to the list provided by http://exoplanet.org as of May 2015

sumptions on the properties of the stellar surface and the planet. In Sect. 3.1.3 we state the specific questions we want to investigate and describe the individual simulation setups in detail. In Sect. 3.1.4 we present the results for each of our previously described simulation setups. In Sect. 3.1.5 we explore the possibility for the spot-crossing events to create spurious TTVs in transit sequences. In Sect. 3.1.6 we present a comparison of our results with real TTV observations. Finally, in Sect. 3.1.7 we discuss our results, and conclude with a summary in Sect. 3.1.8.

3.1.2 Light curve simulations

3.1.2.1 Light curves of stars with spots

A rotating star with a persistent dark spot on its surface produces a periodic modulation of its light curve. However, the exact shape of the photometric variation depends on the properties of the star and of the spot. If the life time $\tau_{\rm sp}$ of the spots (or rather active regions) is much longer than the stellar rotation period $P_\star$, the observed flux variations will be similar from one rotation to the next.

In many of the *CoRoT* and *Kepler* light curves of active stars with $\tau_{\rm sp}/P_\star > 1$, the observed photometric variations consist of one or two pronounced dips per rotation, usually without the presence of any intervals where the stellar flux stays constant. This suggests that there are always at least a few spots located on the star that rotate on and off the visible hemisphere. The peak-to-peak amplitude of such photometric variations can be as high as several percent of the total flux (Basri et al. 2013).

Throughout our simulations we make the simplified assumption that the stellar surface is covered by only one large spot with a temperature lower than the photospheric temperature. We also assume that the spot properties do not change, i.e., we do not consider spot evolution effects or any internal spot structure such as penumbra and umbra. We adopt a center-to-limb intensity variation of the stellar photosphere according to the specific temperature, which is parameterized using a quadratic limb-darkening law.

3.1.2.2 Spot-crossing events

In the following we briefly explain our mathematical description of the photometric effects we expect during a spot-crossing event. During a planetary transit the total flux F_0 of the star decreases to $F_{\rm tr}$ because the planet covers part of the stellar disk. We obtain for the ratio $F_{\rm tr}/F_0$ the expression

$$\frac{F_{\rm tr}}{F_0} \;=\; 1 \;-\; \frac{R_{\rm pl}^2}{R_\star^2} \;=\; 1 \;-\; f_{\rm pl}, \qquad (3.1)$$

where $R_{\rm pl}$ denotes the planetary radius and $R_\star$ the stellar radius. We call $f_{\rm pl}$ the planetary filling factor. For the sake of simplicity, we assume that the planetary disk is completely dark; we ignore the limb-darkening (LD) effects and the ingress and egress phases when the stellar disk is only partially covered by the planet; however, the formalism is easily extended to cover these effects.

We now consider a spotted star with a spot filling factor $f_{\rm sp}$, which denotes the relative area covered by spots. We also introduce the relative spot temperature $t_{\rm sp} = T_{\rm sp}/T_\star$, where $T_{\rm sp}$ and $T_\star$ denote the temperatures of the spot and the photosphere, respectively. In this case the observed normalized flux of the star is not F_0, i.e., the flux seen from an undisturbed photosphere; rather, we see the "spotted" flux $F_{\rm sp}$ given by the expression

$$\frac{F_{\rm sp}}{F_0} \;=\; 1 \;-\; f_{\rm sp}(1 - t_{\rm sp}^4)\;. \qquad (3.2)$$

Now we consider the case of a spot-crossing event during a planetary transit and assume that the transiting planet is occulting a starspot either partially or totally. We let $df_{\rm pl}$ denote the fraction of the planetary disk covering a spotted surface area, while $(1-df_{\rm pl})$ denotes the fraction of the planetary disk covering unspotted photosphere. In this case, the observed flux during the transit $F_{tr,sp}$ is given by the spotted flux $F_{\rm sp}$, diminished by the relative flux of spotted and unspotted photosphere covered by the planet, i.e.,

$$\frac{F_{\rm tr,sp}}{F_0} \;=\; 1 - f_{\rm sp}(1-t_{\rm sp}^4) \;-\; f_{\rm pl}\left[1 - df_{\rm pl}\left(1-t_{\rm sp}^4\right)\right]. \tag{3.3}$$

We usually work with transits normalized to the out-of-transit flux, which means we divide this equation by the contribution of the spot (Eq.3.2). This normalized flux d is then defined by

$$d \;=\; \frac{F_{\rm tr,sp}}{F_{sp}} \;=\; 1 \;-\; \frac{f_{\rm pl}\left[1 - df_{\rm pl}\left(1-t_{\rm sp}^4\right)\right]}{1 - f_{\rm sp}(1-t_{\rm sp}^4)}\;. \tag{3.4}$$

If the starspot only insignificantly contributes flux with respect to the unspotted surface ($t_{\rm sp} \approx 0$), and if that spot is large enough that the planet covers only spotted surface regions ($df_{\rm pl} = 1$), Eq. 3.4 becomes unity, i.e., the spot-crossing event would increase the flux to the out-of-transit level. We are not aware of any observations presented so far where this has been seen and we propose several reasons for this. First, although starspots are likely to be much cooler than photospheric temperatures, they still contribute a significant amount of flux. Second, most individual starspots are probably not as large as a planet. When we talk about starspots, we usually do not think of one large uniformly dark spot but of a densely spotted region made up of umbra, penumbra, and photospheric parts. However, such an active region might easily be much larger than the occulting planet, although the very dark (umbral) parts of the region are not. Third, a planet crossing over such a spotted area does not always have to cover the darkest parts of the spot but can cross near the periphery as well.

We introduce the height H of the spot-crossing anomaly in a transit, which is given by the comparison between the relative flux d in the cases with and without ($d_{df_{\rm pl}=0}$) a spot-crossing event.

$$H \;=\; \frac{d \;-\; d_{df_{\rm pl}=0}}{1 \;-\; d_{df_{\rm pl}=0}} \;=\; df_{\rm pl}(1-t_{\rm sp}^4). \tag{3.5}$$

Figure 3.1 illustrates the dependence of H on $df_{\rm pl}$ and $t_{\rm sp}$; for $H = 0$ there is no spot-crossing anomaly, while $H = 1$ means that the increase is equal to the transit depth and, thus, the flux returns to the out-of-transit level. As discussed before, values of $H > 0.5$ have not been observed so far and seem to be unlikely; therefore, we select those combinations of $df_{\rm pl}$ and $t_{\rm sp}$ in our simulations that produce an increase in flux of 50 % of the mid-transit depth (see Fig. 3.1, dashed line).

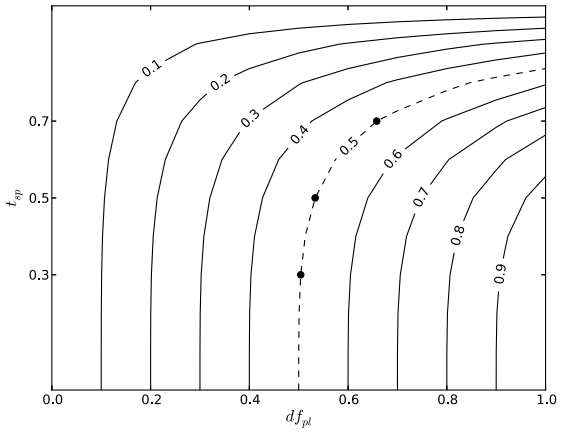

Figure 3.1: Spot-crossing anomaly height H (contours) as a function of the fraction of the planetary disk, which covers spotted surface area $df_{\rm pl}$ and the spot temperature $t_{\rm sp}$. For our simulations we use values of $df_{\rm pl}$ that correspond to spot temperatures equal to 0.3, 0.5, and 0.7 in order to reach $H = 0.5$ (black dots along the dashed line).

3.1.2.3 Model calculations

Given the assumption that a spot has either a circular or an elliptical shape with a total area $A_{\rm sp}$, our algorithm calculates analytically the light curve modulations due to stellar rotation using the relationship

$$\frac{F_{\rm sp}}{F_0} \;=\; 1 - \frac{A_{\rm sp}\cdot\cos(\theta)}{\pi R_\star^2}\,(1-t_{\rm sp}^4)\cdot I(\theta, c_1, c_2)\;, \tag{3.6}$$

where θ denotes the angle between the normal to the stellar surface and the line of sight towards the observer. The factor $I(\theta, c_1, c_2)$ accounts for the LD of the disk, which depends on the angle θ and,

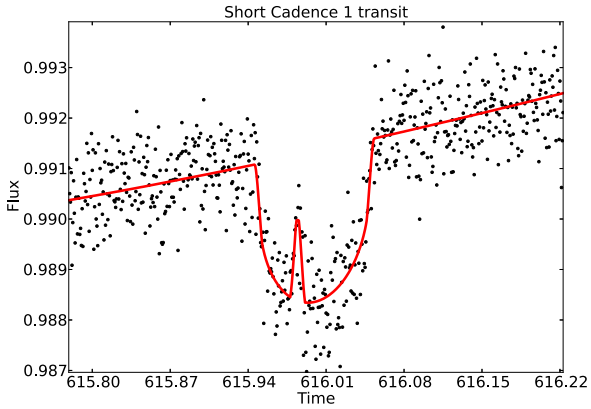

Figure 3.2: Simulated transit of a Neptune-sized planet. The red line represents the infinite signal-to-noise data, while the noise of the black dots is similar to that of *Kepler* short cadence data. During the transit there is a spot-crossing event right after the ingress.

because we choose to use a quadratic LD parameterization, on the limb-darkening coefficients (LDC) c_1 and c_2.

When a planet transits in front of the star, our algorithm uses the model of Mandel & Agol (2002) to calculate the transit-induced flux reduction. In Fig. 3.2 we show an example of some typical light curves that our algorithm produces. In this example the light curve of a Neptune-sized planet orbiting a K-type dwarf is shown; its noise level is adjusted to a star with a *Kepler* magnitude of $K_p = 13$ (black dots) along with the infinite signal-to-noise case (red line).

The calculation of spot-crossing events involves inter-subsections of circles and an ellipse, which we choose to perform numerically. To the left of the transit center there is an anomaly caused by a spot-crossing event. The overall light curve slope is caused by the flux variation due to the rotation of the star.

3.1.2.4 General assumptions

We briefly summarize the basic assumptions for the simulated light curves we use to study the effects of spot-crossing events on TTVs:

1. The planet crosses only one uniformly dark spot per transit.
2. The shape of the spot is either circular or elliptical.
3. We consider relative spot temperatures $t_{\rm sp}$ of 0.3, 0.5, and 0.7.
4. The fraction of the planet that covers the spotted area is chosen in such a way that the flux increment at mid-transit yields 50 % ($H = 0.5$), assuming an impact parameter $b = 0$.
5. The noise level is adjusted to the precision of *Kepler* short cadence photometry for a $K_p = 13$ mag star (Gilliland et al. 2010).
6. We introduce the parameter signal-to-noise ratio of the transit (TSNR), which is the transit depth divided by the out-of-transit light curve noise level (see assumption 5).
7. Each data point represents an integration over 60 seconds.
8. The rotation period of the star is fixed to 10 days.

3.1.3 Simulation strategy

Spot-crossing events cause deformations of the transit shape which, potentially, lead to a shift of the measured mid-transit time. We set up individual light curve simulations to address three questions:

1. How much are the measured mid-transit times affected by the longitudinal position of a spot during a spot-crossing event?
2. How do the orbital characteristics of the planet, i.e., its orbital period and impact parameter, influence the shift of mid-transit times?

3. Does the influence of a spot-crossing event on timing measurements vary for different stellar types?

3.1.3.1 Spot position

The strength of the deformation of a transit profile caused by a spot-crossing event depends on the longitude of the spot. To study the effect on mid-transit times, we first consider a transit of a planet with an orbital period equal to the stellar rotation period. The planet has an impact parameter of $b = 0$ and, thus, transits the center of the stellar disk. A spot with a relative temperature of $t_{\rm sp} = 0.3$ is placed on the stellar equator at longitude $\lambda_{\rm o}$, which is the longitude of the spot at the epoch of the observation; $\lambda_{\rm o} = 0$ denotes the sub-observer point at the center of the disk, with $\lambda_{\rm o} = -90$ being the leading edge and $\lambda_{\rm o} = 90$ the trailing edge of the disk.

We adopt a K-type dwarf host star ($T_{eff} = 4300\ K$) with a quadratic LD law and use LDCs of $c_1 = 0.690$ and $c_2 = 0.034$ as provided by Claret et al. (2012) for the *Kepler* mission. We simulate light curves based on three different assumptions for TSNR: one for infinite TSNR, and two more with TSNR values equal to the expected precision for planets with $R_{\rm pl}/R_\star = 0.05$ and $R_{\rm pl}/R_\star = 0.1$ (see assumptions 5 and 6 in Sect. 3.1.2.4).

3.1.3.2 Planetary orbit

If the planet's orbital period $P_{\rm pl}$ is much smaller than the stellar rotation period $P_\star$, the spot's position hardly changes while the planet is crossing over it. If $P_{\rm pl}/P_\star$ increases, the spot starts to move significantly during its occultation by the planet. To estimate the strength of this effect on the measurement of mid-transit times, we study simulations with orbital periods of 5, 10, 20, 40, 80, 150, 300, and 600 days. We also consider different impact parameters of $0 \leqslant b < 1$ in combination with different spot longitudes $\lambda_{\rm o}$. The sizes of our test planets are $R_{\rm pl}/R_\star = 0.1$ and $R_{\rm pl}/R_\star = 0.05$. For this simulation the stellar inclination is fixed to zero and the host star has the same properties as described in Sect. 3.1.3.1.

3.1.3.3 Stellar limb darkening and inclination

Even though the effect of a spot-crossing event on TTV measurements should be dominated by the properties of the spot and the planet, we also investigate the influence of LDCs in detail. We consider main-sequence stars with effective temperatures of $3500\ {\rm K} \leqslant T_{\rm eff} \leqslant 10\,000\ {\rm K}$ and use the corresponding LDCs of the *Kepler* band pass (Claret et al. 2012). Furthermore, we investigate how different stellar inclinations influence the measurement of mid-transit times. The planet in this setup has a size of $R_{\rm pl}/R_\star = 0.1$ and an impact parameter of $b = 0$. We vary the inclination of the star and the spot latitude.

3.1.4 Results

The light curves simulated in Sect. 3.1.3 generally contain a slope caused by the starspot located on the rotating surface (see Fig. 3.2). In order to remove this trend, we first identify the transit in the light curve, remove those parts of the light curve affected by the transit, fit a second-order polynomial to the remaining out-of-transit data, and divide the fit from out-of- and in-transit data to produce a normalized transit light curve. We then compute the mid-transit times and errors from these normalized transit light curves by using the model described by Mandel & Agol 2002 combined with a Markov chain Monte Carlo (MCMC) sampler where the only free parameter is the mid-transit time.

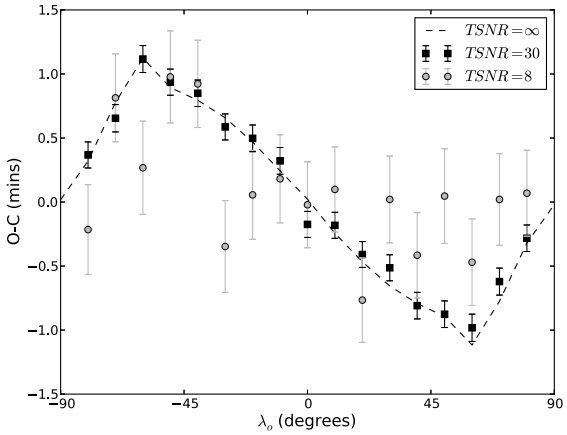

Figure 3.3: $t_{\rm sp} = 0.3$ simulation for different TSNR levels. The dashed line represents the case of infinite TSNR. The measurement error for transits with TSNR=30 is still small enough for the underlying modulation caused by the spots to be seen, whereas for TSNR=8 the spot signal vanishes in the noise.

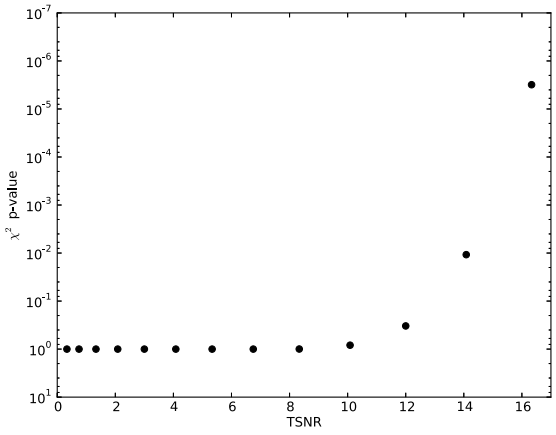

Figure 3.4: p-values of the null hypothesis χ^2 analysis for mid-transit times of transits with different TSNR values. The transits with TSNR < 15 do not show statistically significant evidence of variations. As a result, the mid-transit times of better resolved light curves are more vulnerable to deviations caused by spot crossing events.

3.1.4.1 Spot position

Here we present the results derived for the simulations described in Sect. 3.1.3.1. In Fig. 3.3 (dashed line) we show the difference $(O - C)$ between mid-transit times determined from our simulated light curve and the input times for the different longitudes $\lambda_{\rm o}$ of the occulted spot.

Figure 3.3 (dashed line) also illustrates that the maximum deviation of TTV measurements caused by spot-crossing events is ~ 1.2 minutes in this particular case. The maximum values are encountered when the spot is located between the center and the limb of the stellar disk at about $\lambda_{\rm o} \sim \pm 70^{\circ}$. An anomaly at the transit center has no influence on the derived mid-transit times. The spot-induced deviations also decrease towards the limb of the star because the projected size of the spot decreases and LD reduces the flux contributing from these parts of the stellar disk.

The spot-crossing anomalies introduce positive variations when they occur before the mid-transit time and negative ones in the opposite case. When the planet occults a spot during ingress or egress, the measured transit duration is affected mostly because there is a pseudo-shift of the first or fourth contact time; the transit seems to start later or end earlier, respectively. Thus, there is a shift of the mid-transit time into the opposite direction of the spot-crossing event.

So far we have dealt with the case of infinite TSNR. Naturally, measured mid-transit times have errors that we determine using a MCMC algorithm. Measurements and their errors for the case of a planet with $R_{\rm pl}/R_{\star} = 0.1$ are shown in Fig. 3.3, which corresponds to an TSNR of 30 and $R_{\rm pl}/R_{\star} = 0.05$ equivalent to TSNR=8. For the larger planet the spot-induced deviations of the mid-transit times from the input is still detectable within the relatively small errors and follows the same pattern as for the infinite TSNR case. However, the errors for the smaller planet are much higher and a systematic modulation caused by spots is no longer clearly visible.

Assuming as a null hypothesis that no TTVs are produced by the spot, we perform a χ^2 analysis on

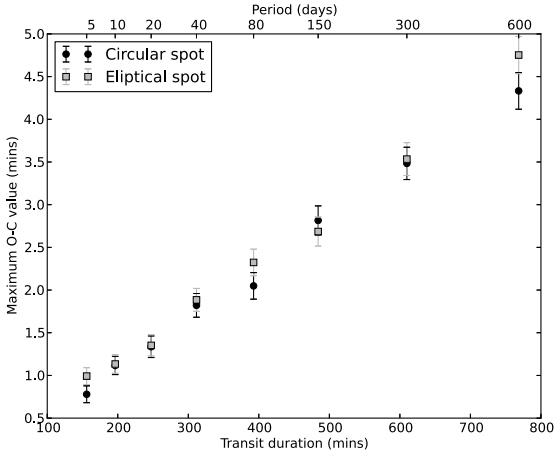

Figure 3.5: Maximum deviation in the mid-transit time of a planet with TSNR=30 for different transit durations. As the period and hence the transit duration increase, the maximum deviation grows larger. The black dots refer to the maximum values caused by circular spots; the gray squares refer to elliptical spots.

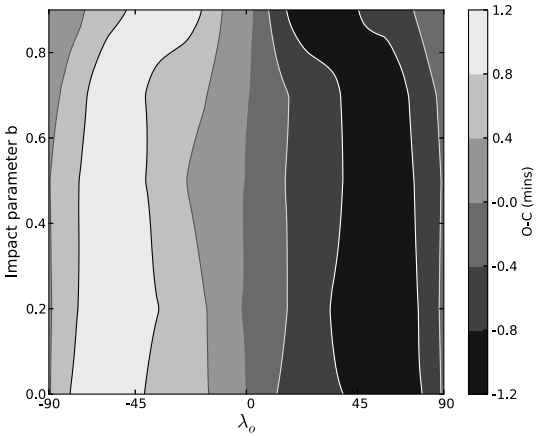

Figure 3.6: TTVs for a simulation of a planet with TSNR=30 (contour map) as a function of the longitude λ_o and the impact parameter b. As shown in Fig. 3.3, $O-C$ has positive values for spot-crossing events before $\lambda_o = 0$ and negative values otherwise. While there is almost no difference in the maximum values, their positions shift to longitudes closer to the center of the star for higher impact parameters.

the TTVs (see Fig 3.3) of transits with different TSNR. As shown in Fig. 3.4, the deviations caused by spot-crossing events start to disappear in the measurement noise for transits with TSNR$\lesssim$15.

3.1.4.2 Planetary orbit

Based on the simulations described in Sect. 3.1.3.2, Fig. 3.5 presents the maximum deviation of mid-transit time measurements caused by spot-crossing events for different values of $P_{\rm pl}/P_\star$. The TTV maximum increases linearly with the transit duration, which in turn increases with the period ratio. For the same spot-crossing event a longer transit duration leads to a larger shift (e.g., Sanchis-Ojeda et al. 2011).

We also consider the possibility that spots might not always be circular. In Fig. 3.5 we also show our results for elliptical spots, which indicate that circular and elliptical spots with equal filling factors lead to virtually identical results.

We conclude that the precise spot geometry appears to be of minor importance. Next we consider how the derived transit times depend on the impact parameter of the transits. Figure 3.6 shows how the difference between measured and calculated mid-transit times changes with the impact parameter of the planet. Owing to the LD of the stellar disk and to geometrical effects, the transit profile becomes more V-shaped for larger impact parameters, and the maximum of the residuals moves closer to the center of the star. The change of the transit shape increases the influence of the spot-crossing event on the measurement of the mid-transit time. On the other hand, for high values of the impact parameter, the amplitude of the $O-C$ becomes smaller due to the shorter transit duration (see Fig. 3.5). Therefore, the additional deviation that the deformation of the transit introduces is canceled by the reduction of the transit duration. As a result, there is no significant difference in the amplitude of the residuals for different impact parameters.

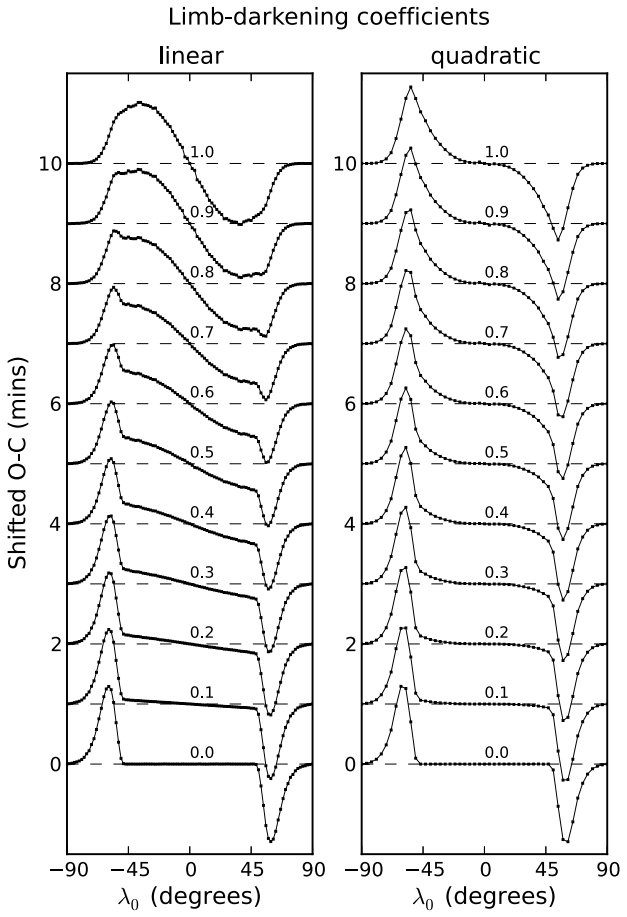

Figure 3.7: Effect of different LDCs on the measured mid-transit time for transits with infinite TSNR and spot-crossing events in various longitudes λ_o. The panels refer to linear (left) and quadratic (right) LDCs with values between unity (top) and zero (bottom).

3.1.4.3 Stellar limb darkening and inclination

In order to study how LD affects the the timing deviations we used a planet size of $R_{\rm pl}/R_\star = 0.1$ and a relative spot temperature of $t_{\rm sp} = 0.3$, assuming a period ratio equal to unity. The strength of the measured deviations does not significantly depend on the LDCs. However, for lower effective temperatures the region of large deviations introduced to the mid-transit time is larger and its inner boundary moves closer to the center of the star.

To better illustrate the influence of LD on the effect of transit time measurements, we simulated light curves with different linear and quadratic LDCs in the range of zero to unity. The results are presented in Fig. 3.7, where the left panel shows the results for different linear LDCs with $c_2 = 0$ and the right panel for different quadratic LDCs with $c_1 = 0$. While the spot-crossing anomaly moves from one side of the transit to the other, the measured shift changes in a similar way to what has been shown in Fig. 3.3. However, Fig. 3.7 illustrates that the influence of LD on the shape of the curve is rather large. For small LDC values there is only a spot-induced shift of the transit time at ingress and egress and hardly a shift in between because, in the absence of LD, the transit has a box-shaped profile and is flat at the bottom. The model does not have the flexibility to compensate an anomaly caused by the spot in the flat part of the transit. Thus, this anomaly cannot be fitted and the best fit results ignore the spot.

However, this changes for larger LDCs because the transit shape becomes rounder and the bottom is no longer flat. The stronger the LD, the higher the curvature, and a shift of the model can lead to a better fit even if the spot signature is closer to the center. This effect is stronger for the linear component because it influences the center of the transit much more than the quadratic LDC does. The latter has its largest influence at the ingress and egress which is the reason why in this case the curves show greater change in the outer parts and only a little at the center. Although the influence of LD appears to be large (see Fig. 3.7), for the relevant temperatures considered in our simulations the LDCs change very little and stay at roughly $c_1 = 0.7$ and $c_2 = 0.1$. For small changes in the LDCs, the curves in Fig. 3.7 change only slightly.

Finally, we also investigated how different values for the inclination of the rotation axis of the star affect the measured transit times. However, we could not detect a dependence in the maximum

amplitude of the spot-induced TTVs on the stellar inclination.

3.1.5 Sequence of consecutive transits

So far we have studied only the effects of a spot-crossing event on the TTV measurements of a single transit for different parameter combinations. However, we have not yet investigated series of consecutive transits of the same system. According to our previous results, a spot-crossing event can cause deviations of the mid-transit times of up to a few minutes. The amplitude alone, however, does not tell us whether it is possible to produce a spurious signal in the timing measurements from a sequence of transits that could mimic the signal of a true physical companion in the system. In this case the activity would lead to a false positive detection of a body that does not actually exist.

It is rather difficult to study such problems in simulations because the results always sensitively depend on the selected input parameters. If we choose some specific spot configuration with spot lifetimes and differential rotation, etc., our results would strongly depend on these assumptions. We try to minimize this by choosing a simple, straightforward approach which considers a worst-case scenario: We assume that for all transits in a light curve the spot is always occulted if it is located on the visible hemisphere and that the spot has an infinite lifetime. This is certainly not what one expects to actually find; spots are not always located exactly under the planet path and they certainly have limited lifetimes. Furthermore, we adopt a comparatively large spot. However, in this way our results will give an estimate of what might be observed in the most problematic cases.

3.1.5.1 Simulation setup

We set up 7500 simulations in such way that for each individual simulation a series of 100 consecutive transit light curves of the same system are calculated. We consider different TSNR values and orbital periods of the planet (measured in days), which are both randomly drawn from a uniform distribution between 1 and 30. The stellar rotation period is always fixed to 10 days. We assume only one spot on the surface which is always occulted when located on the visible hemisphere. If the planet crosses an unspotted disk, its transit will not be deformed by any spot-crossing feature; nonetheless, the transit will continue to be part of the sequence. The spot lifetime is assumed to be infinite and its covered area is set to follow the assumption given in item 4 in Sect. 3.1.2.4.

We then measure the mid-transit times of the simulated transits as described in Sect. 3.1.4 (including their measurement uncertainties using MCMC) and calculate the residuals by subtracting the expected values $(O-C)$. Additionally, we calculate the mean of the residuals and subtract it. The Generalized Lomb-Scargle periodogram (Zechmeister & Kürster 2009) is then used to determine the period $P_{\max}$ in the TTVs with the smallest false alarm probability (FAP) for each individual simulation. Finally, for each simulation we calculate the amplitude of the TTVs using the relationship

$$A_{\max} = [(O-C)_{\max} - (O-C)_{\min}]/2. \qquad (3.7)$$

3.1.5.2 Simulation results

In Fig. 3.8 we show the FAP of the most significant period as a function of the TSNR for each of our simulations. The average FAP decreases with increasing TSNR. This reflects the fact that transit times calculated from light curves with small TSNRs have relatively large uncertainties which leads to higher FAPs when searching for periods. The majority of periods for transits with TSNRs $\gtrsim$ 15 have FAPs $\lesssim 10^{-3}$, which we considered significant enough not to be spurious signals.

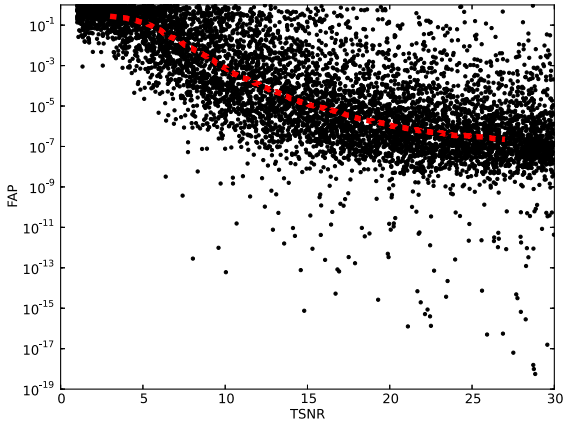

Figure 3.8: FAP of the highest peak in the Generalized Lomb-Scargle periodogram over the TSNR of the planetary transits for all 7500 simulation. On average, the strongest periods in the simulations become more significant for higher TSNRs. The red line demonstrates the running median of the FAP in TSNR bins of six. Most of the points larger than TSNR $\gtrsim 15$ have FAPs below 10^{-3}.

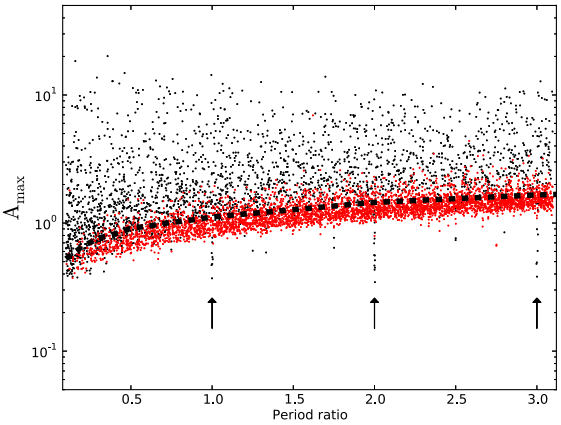

Figure 3.9: Amplitude of the TTV measurements over the period ratio for all individual simulations. The red points indicate all simulations for which the determined period has a FAP $< 10^{-3}$, which are the simulations with high TSNRs (see Fig. 3.8). The black dashed line indicates the maximum amplitude values given by Fig. 3.5. The arrows indicate the localized drops in amplitudes at integer period ratios (see Sect. 3.1.5.2).

Although in our simulations these periods are caused by spots, a reliable distinction of whether such a period is caused by spots or additional bodies in the system might be quite complicated in real observations.

Figure 3.9 shows $A_{\max}$ as a function of the period ratio for all individual simulations. We divided the results into two groups, amplitudes coming from simulations with a FAP $< 10^{-3}$ (red points) and amplitudes with larger FAPs (black points). For the latter group the uncertainties of the transit time measurements are high (TSNR is usually small) and the amplitude primarily reflects the scatter of the TTVs due to noise. For the first group the systematic variation due to spots is larger than the uncertainties (high TSNR) and the amplitude represents the effect the spots have on the measurement of the TTVs. The FAP $< 10^{-3}$ points show much smaller scattering and are limited to a region close to the lower edge of the measured amplitudes. As expected, the majority of these points lie under the maximum deviation values (dashed line), which we present in Fig. 3.9.

This region is basically defined by the planetary period and therefore the transit duration, because the maximum amplitude of a spot-crossing event becomes smaller for smaller transit durations. An interesting feature of Fig. 3.9 is the localized minima of amplitudes at integer period ratios. At these resonance periods the spot-crossing feature hardly changes position in the transit profile and the spot-induced timing variation are small. A period ratio of exactly one (two, three, etc.) means the TTVs are all on one level and vary only because of noise.

In Fig. 3.10 the period with the highest FAP determined from the $O-C$ diagram of each individual simulation is plotted over the period ratio. The lower envelope is determined by the Nyquist frequency. The highest periods that can be determined are roughly defined by the time span covered by the TTVs. The up-and-down patterns shown in Fig. 3.10 result from the different TSNRs of the simulations. For low FAPs (red points) maxima at resonances of period ratios (0.5, 1, 1.5, etc.) and minima in between can be seen. In a system

where the periods of star and planet are not integral multiples, the position of the spot-crossing event changes from one transit to the next. As the period ratio $P_{\rm pl}/P_\star$ moves closer to a resonance, the difference between the longitudes $\lambda_{\rm o}$ of the spot-crossing events in two consecutive transits becomes smaller. This leads to a lower frequency TTV, which is interpreted as a higher TTV period by the periodogram. Exactly at the resonance the TTVs are flat and the periods go down to the Nyquist frequency. This is also true for period ratios at 0.5, 1.5, and so on; however, not every transit shows a deformation caused by a spot. At ratio 0.5, for example, the spot is seen only every second transit, which results in one level of transits that are not disturbed by the spot and a second level of transits which are all shifted by the same value. For very low noise the amplitude is then basically given by the difference between the two levels.

Going to larger FAPs, we see a second pattern (made up of red and black points in Fig. 3.10), which is reminiscent of the previous structure but peaks only at integer resonances and goes down to the Nyquist frequency at 0.5, 1.5, and so on. This happens when the uncertainties of the individual mid-transit time measurements are about equal to the amplitude caused by the spot-crossing effect. For simulations with even higher FAPs, we end up with the points that are randomly distributed because the uncertainties of the mid-transit times are larger than potential spot-induced variations.

3.1.5.3 Can spots mimic bodies in transit sequences?

We emphasize again that our simulations show a worst-case scenario. In the majority of planetary systems, periodic signals in TTVs caused by spots should be much weaker and less coherent. In reality, the spots grow and decay, change their positions, and are probably smaller than we assume in our simulations. Such changes will always lead away from the clear patterns shown in Fig. 3.10 (red points) to a random distribution of points.

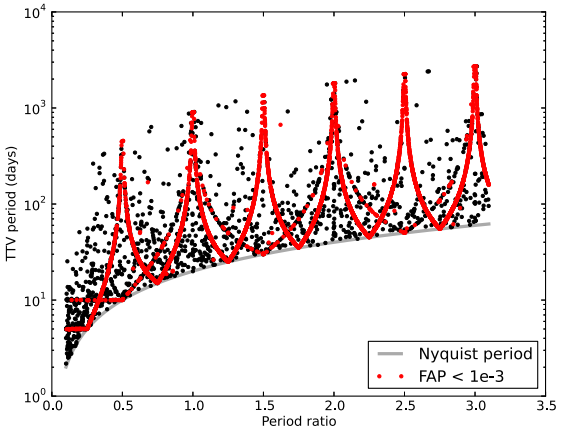

Figure 3.10: For each individual simulaiton, the most significant period is determined from the TTVs over the input period ratio. The gray line indicates the lower limit of possible periods defined by the Nyquist frequency. The red points indicate periods with FAP $< 10^{-3}$.

However, we argue that it is possible to observe a periodic signal mimicking TTVs of a potential companion in the planetary system caused by spot-crossing events. For high TSNRs, period ratios close to resonances are particularly dangerous. A careful inspection of the transit shapes and their deformations should provide additional information on whether the determined mid-transit times are reliable or subject to dispute. In many cases the TTVs due to spots should show odd behavior such as the splitting of points into two or more levels or alternating intervals of strong and weak variability, which could be valuable indications that the TTVs are possibly due to spots. Unfortunately, depending on the exact properties of star, spot, and planet, TTVs do not necessarily have to show such odd behavior.

Whenever a significant periodic signal is found in noisy TTVs, it should be interpreted carefully especially if the star shows signs of activity. If small-scale features in the transit profiles are hard to discern and if the errors in the transit times are on the order of (or even larger than) the deviations due to potential spots, one could still end up with

a significant period. Whether this period is caused by spots or a yet unknown body in the system will be hard to determine.

3.1.6 Comparison to observations

In Fig. 3.11 we show the cases of TTV detections as presented by Mazeh et al. (2013). In their discussion regarding those TTVs detections Mazeh et al. (2013) suggest that three of them show a correlation between the period of the TTVs and the rotational period of the star that was determined from its light curve. The TTV amplitudes for these planets lie well below the upper limit we calculated from our simulations, which supports our result that larger amplitudes caused by spots are unlikely. Larger TTV amplitudes might also be modified by starspots but are hardly exclusively created by them.

In a recent article Masuda et al. (2015) present the light curve of the KIC 6543674 triple star system, which consists of a short-period (2.4 days) inner binary with a companion in a wide eccentric orbit. Their study of the system presents eclipse timing variations (ETVs) with amplitudes of ~ 4 mins which do not seem to be caused by any known companion. They imply that these ETVs can be explained by the existence of starspots; however, they do not model them. Although we do not study ETVs of stars in this paper, a spot-crossing event of a star should be comparable to our simulations with planets. Spot-eclipses should cause shifts from the expected mid-eclipse time due to the deformation of the eclipse shape as well.

The residual ETVs resemble quite closely the longitude-dependent spot-crossing pattern we show in Fig. 3.3. In order to create such ETVs, the period ratio between the orbital period of the occulting body and the rotational period of the occulted star must be very close to, but not exactly equal to an integer value. Interestingly, the ETVs do not show flat regions with no modulation, which one would expect if no spot is on the visible hemisphere. Instead the pattern continues very regularly, which

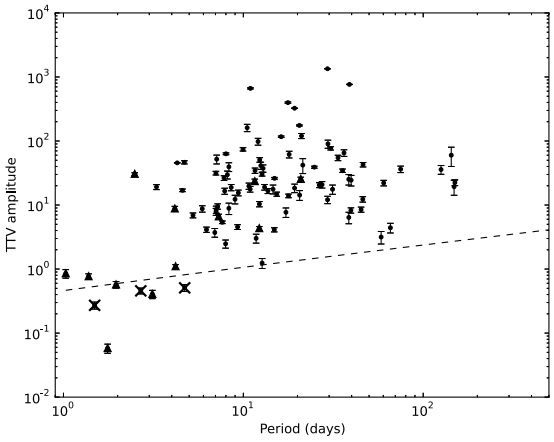

Figure 3.11: TTV amplitudes reported by Mazeh et al. (2013). The dashed line denotes a linear fit to the maximum amplitudes for TSNR=30 (see Fig. 3.5). The points marked with X are found to have periods related to the stellar rotation; all of them lie well below our predicted amplitude maximum caused by spots. The points marked with triangles are taken as spurious which could have been caused by other sources capable of inducing TTVs (i.e., sampling or eclipsing binaries).

indicates the existence of two or more large active regions, non-uniformly distributed on the surface of the occulted star. Another interesting feature is the long lifetime of these active regions. The modulation in the ETVs evolves so slowly that a reminiscent pattern repeats for about three years before it significantly changes.

The amplitude of the measured ETVs appears to be larger than predicted by our simulations for exoplanetary transits with equal duration times; the eclipses of the inner KIC 6543674 system last about 360 min, which according to Fig. 3.5 should lead to maximum amplitudes of about 2 mins. To check if we could reach the amplitude of the Masuda et al. (2015) ETVs, we run a simulation setup with the properties of this system and obtain ETVs with comparable amplitudes in quite a few cases. This result also agrees with the amplitudes of spot-induced ETVs from other binaries shown by Orosz (2015). There are two reasons for the deviation between the maximum amplitudes of spot-induced

TTVs and ETVs, the shape of the eclipse and the area of spots covered by the occulting body. The eclipses of binary stars with comparable sizes usually show only the ingress and the egress and not the flat part in between. Therefore, spot-crossing anomalies can cause significant TTVs for spots at all possible longitudinal positions. Owing to the large size of the occulting body, it is also likely that large areas of spots on the occulted body are eclipsed, which also leads to stronger ETVs.

A detailed modeling of this system, including spots, is needed to evaluate whether these two arguments are sufficient to explain the observed ETVs - or even if spots are an appropriate explanation for these ETVs at all. Although this is beyond the scope of this work on exoplanets, we emphasize that if these ETVs are really due to starspots they resemble the results of our simulations quite nicely and demonstrate that clear repetitive modulations due to spots over timescales of years are possible, and the probability of misinterpreting them as signals of an unknown body is not negligible.

3.1.7 Discussion

Our simulations of spot-induced transit timing variations suggest that even large spot-crossing anomalies in transit profiles should not lead to TTV amplitudes larger than a few minutes (Figs. 3.5 and 3.9). The amplitude depends very strongly on the transit duration and the position of the spot-crossing event. As shown in Fig. 3.3, the uncertainties of the measured mid-transit times primarily depend on the TSNR and transit duration, but only little on the characteristics of the spot-crossing events. Specifically, the uncertainties do not depend on the position of the spot at the time of the transit, whereas the TTV amplitude clearly does. Thus the uncertainties should not be used as a diagnostic for spot-induced TTVs, despite the deformation of the transit light curve, even for the rather large spots assuming in our simulations.

The amplitude of the spot induced TTVs is independent from the inclination of the star, as we discuss in Sect.3.1.4.3. Nevertheless, in the case of low stellar inclination it is possible that a spot-crossing event can occur at the cross subsection of the planetary orbit and the active latitudes of the star. This has an impact on the results given in Sect. 3.1.2; due to the fixed position of the spot-crossing events, the values of the TTVs amplitudes are going to be distinct and not continuous. Such $O-C$ diagrams produce periodicities that have very little significance which have a low probability of being considered real.

The maximum mid-transit time deviations derived from our simulations are significantly smaller than the maximum $O-C$ values calculated from Mazeh et al. (2015) and Oshagh et al. (2013). The reason for this discrepancy is our assumption that the in-transit flux increment due to the spot occultation is not larger than 50 % of the mid-transit depth. In our opinion this value is a better representation of observational evidence, since we do not know of a single case where the induced anomaly is $\gtrsim 50$ % of the transit depth.

3.1.8 Conclusions

Our simulations were geared to study TTVs induced by starspots using high-precision photometric data without any red noise sources. While it is relatively safe to apply our results to data obtained by space missions, it is difficult to estimate the behavior of such spot-induced TTVs on light curves with significant contribution of red noise (i.e., scintillation).

Finally, we summarize the most important results of our simulations on spot-induced TTVs of exoplanets:

- In agreement with the results of Oshagh et al. (2013) and Barros et al. (2013), spot-crossing events can cause shifts of the measured mid-transit times. These shifts can cause a specific pattern depending on the longitude λ_o of the spot during the crossing event (see Fig. 3.3).

- The amplitude of the shift is determined by the temperature of the spot relative to the photospheric temperature, the fraction of the planet covering spots, and the duration of the transit.
- The shape of the spot or the stellar inclination during a spot-crossing event do not seem to significantly affect the mid-transit times.
- We find only a weak dependence of the measurement uncertainties on longitude λ_o. We conclude that they are no reliable indicators for how much individual timing measurements are affected by spots.
- The impact parameter of the planet and the limb darkening of the star influence the shape of the transit profile, which affects the TTV measurements. However, this seems to be a minor contribution compared to the other influences.
- A sequence of transits affected significantly by spots can create a statistically significant periodical signal. In special cases the spot-induced TTVs could even show a clear, persistent modulation imitating the existence of a sub-stellar companion. However, these cases should be rare and a careful analysis of the data should indicate a potential influence of starspots, especially for systems with high TSNR.
- Extra attention should be paid to TTVs with amplitudes $\lesssim$1% of the transit duration (see Figs. 3.5, 3.9, and 3.11).
- The detection of significant spot-induced periods in TTVs depends on the TSNR, and according to our simulations is unlikely for TSNR $\lesssim$ 15. A detection of periods for TSNR $>$ 15 should be treated cautiously, especially if they are attributed to unknown bodies in the system.

3. Ioannidis et al. (2015): *How do starspots influence the transit timing variations of exoplanets?*

Chapter 4

Sneak peeking at stellar surfaces.

4.1 "*Sneak peeking at stellar surfaces II: Spot evolution and differential rotation of the planet host star Kepler-210* ",

P. Ioannidis and J. H. M. M. Schmitt

Submitted for publication in Astronomy & Astrophysics

4.1.1 Introduction

The nature and role of the magnetic dynamo with regard to the differential rotation of dwarf main-sequence stars is not yet fully understood. While these stars often exhibit substantial photometric activity, the amplitude of their surface differential rotation is expected to be small (Küker & Rüdiger 2008). The inability of the small or absent differential rotation to organize the global magnetic field of those stars may result in the absence of activity cycles as observed in the Sun (Chabrier & Küker 2006). As a result, the study of photospherically active stars and the measurement of their differential rotation rates is a crucial ingredient for all dynamo theories.

The rotational period of stars has been measured using a variety of techniques including the monitoring of the variations in the intensity of Ca H+K lines, spectral line broadening (for cases with known stellar radius and inclination) and the analysis of pseudo-periodic photometric modulations as a result of surface inhomogeneities in the form of photospheric activity (spots). The successful operation of the space missions *CoRoT* (Baglin et al. 2006) and *Kepler* (Borucki et al. 2010) in combination with their high accuracy and long, non-interrupted observations revolutionized the studies of stellar rotation with period measurements for a very large number of field stars (Reinhold et al. 2013, McQuillan et al. 2014). Furthermore, the analysis of the photometric light curves of *CoRoT* and *Kepler* using a variety of techniques, including power spectrum analysis (Reinhold & Reiners 2013) and spot modeling (Fröhlich et al. 2009, Huber et al. 2009, Frasca et al. 2011, Bonomo & Lanza 2012) makes it possible to measure differential rotation and other physical characteristics of star spots.

In this paper we use the light curve phenomenology of Kepler-210 (i.e., the variations of the light curve between the stellar rotations) in combination with spot modeling and power spectrum analysis to study its photospheric activity. In Sect. 4.1.2 we describe the data and the properties of Kepler-210. In the second part of this section we present the details of the spot model used in our analysis and explain our choices regarding the number of free parameters in our model. In Sect. 4.1.3 we show the results of our combined analysis and in Sect. 4.1.4 we attempt to explain our results physically. Finally, we conclude with a summary in Sect. 4.1.5.

4.1.2 Data and Analysis

4.1.2.1 Light curve and periodogram

The Kepler-210 system consists of a K dwarf with at least two planets orbiting around it (Ioannidis et al. 2014). The light curve of the system was obtained from the STDADS[1] archive and contains the long cadence data from quarters Q1 to Q17. The removal of instrumental systematics from the *Kepler* light curves is quite cumbersome (Petigura & Marcy 2012, McQuillan et al. 2012, Kinemuchi et al. 2012), thus we chose to use the so-called corrected PDC-MAP data for our analysis. In Figure 4.1 we show the approximately 1500 days long

[1] http://archive.stsci.edu/kepler/data_search/search.php?action=Search &ktc_kepler_id=7447200

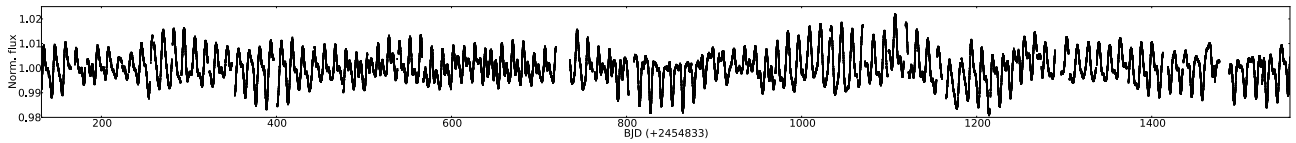

Figure 4.1: The complete light curve of the Kepler-210 (1400 days), normalized and with the planetary transits excluded (see text for details).

light curve of Kepler-210 with each quarter normalized by the mean value of its data **and** the planetary transits removed (using the parameters calculated by Ioannidis et al. (2014)). There are clear modulations with an amplitude of $\sim 2\%$, similar to photospherically active stars, e.g., CoRoT-2 b (cf., Huber et al. 2009). To analyze those modulations we use the generalized Lomb-Scargle (L-S) periodogram (Zechmeister & Kürster 2009) of the total light curve of Kepler-210. The peak with the highest power corresponds to a period of $P = 12.28$ days (see, Sect. 4.1.3.2), however, we find evidence for additional power on various time scales which we would like to explore in the following.

4.1.2.2 Light curve modeling

Basics

To describe the relative stellar flux reduction ($F_{\rm sp}/F_0$) due to the presence of an active region on the stellar surface, given the rotational period $P_{\rm sp}$ of the region, we adopt a simple spot model, given by the expression

$$\frac{F_{\rm sp}}{F_0} = 1 - \frac{A_{\rm sp}\cdot\cos[\,\theta(t)\cdot 2\pi/P_{\rm sp}+\theta_{\rm t=0}\,]}{\pi R_\star^2} \times (1-t_{\rm sp}^4)\cdot I[\,\theta(t)\,,c_1,c_2]\,. \quad (4.1)$$

The terms $A_{\rm sp}$, $R_\star$ and $t_{\rm sp}$ denote the spotted surface, the stellar radius and the relative spot temperature (i.e., the ratio between spot temperature and photospheric temperature) respectively. The term $\theta(t)$ accounts for the angle between the line of sight towards the observer and the normal to the stellar surface, at the time t of the observation. The factor $I[\,\theta(t),c_1,c_2\,]$ denotes the limb darkening (LD) of the stellar disk, which depends on the angle $\theta(t)$. We choose to use a quadratic LD parameterization, with the parameters c_1 and c_2 as limb-darkening coefficients (LDC).

For simplicity, we assume dark circular spots ($t_{\rm sp} = 0$) and note that the spot temperature can easily be calibrated later by increasing the values of the spot radius. Due to the fact that Kepler-210 hosts a planetary system we feel secure to assume that the stellar inclination is $\simeq 90^\circ$ (Tremaine & Dong 2012, Figueira et al. 2012, Johansen et al. 2012, Fang & Margot 2012, Fabrycky et al. 2014, Morton & Winn 2014), which we adopt in the following. While the latitude of an active region can be regulated by its size $A_{\rm sp}$, the term $\theta(t)$ can be used to express the longitude of the region during the observation $\lambda_{\rm o}$; $\lambda_{\rm o} = 0^\circ$ stands for the sub-observer point at the center of disk, with $\lambda_{\rm o} = -90^\circ$ being the leading edge and $\lambda_{\rm o} = 90^\circ$ the trailing edge of the disk.

Spot modeling

In order to describe the light curve changes, we consider chunks of the overall light curve (cf., Fig. 4.1), equal to the leading period of the L-S periodogram, separated by a quarter of that period, i.e., the individual light curves are not independent. The light curve modulations are not sufficiently stable from one rotation to another, so none of the light curve chunks are identical. To cope with this problem we use spot models in order to describe the modulations. Each spot model represents a unique passage of this region over the visible hemisphere of the star. It is well known that the problem of modeling

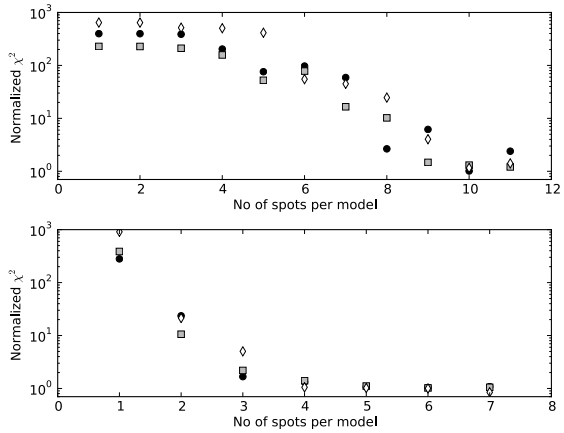

Figure 4.2: χ^2 goodness of the fit for models with different number of equally separated spots (upper panel) and free spots (lower panel). It is clear that the normalized χ^2 is approaching close to unity for models with at least 10 free parameters (see text for details).

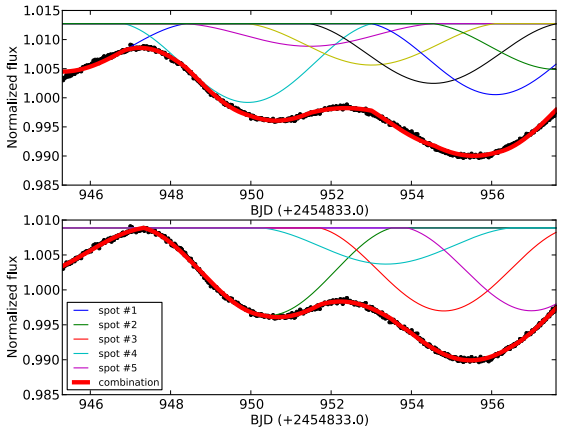

Figure 4.3: Top: Visual representation of the ten fixed spot model. Each of the thin colored lines represents the flux reduction caused from each of the spots during a full rotation. The combined flux reduction is given from the aggregation of the five spots models (thick red line). Bottom: As for top panel, but for the five spot model.‘

the spot distribution on a two-dimensional surface into a one-dimensional light curve is ill-posed, i.e., in general there is more than one model to appropriately describe the observed light curve modulations. Although the quality of model fits increases with the number of spots, i.e., the number of free parameters available, this number should be as low as necessary.

For light curve modeling we consider two different approaches: In the first approach we consider N circular dark spots, where the i^{th} spot has a radius R_i and is located on the equator at some longitude λ_i; in a second approach we consider again N circular dark spots, this time however, at fixed, equidistant locations around the stellar equator. Since the star appears to be always covered by some spots and since stitching of the individual quarters may not be fully correct, it is impossible to know the correct normalization of the light curve. As a result we include an estimate of the level of the unspotted flux in our model. To assess the goodness of fit, we compute the χ^2-values of our fit for all models.

In the upper panel of Fig. 4.2 we first consider the χ^2-values for models with a given number of fixed spots at equidistant locations around the equator for three randomly chosen light curve chunks (described by different symbols). As the spots have only one free parameter (their respective radius), the number of spots is equal to the number of free parameters of the model plus one (for the normalization factor). It is clear that around ten such spots are required to obtain acceptable fits.

In the lower panel of Fig. 4.2 we consider models with a variable number of spots at variable positions along the equator and plot again the χ^2-values as a function of spot number. Clearly, Fig. 4.2 suggests that one needs about five free spots to describe the observed modulations appropriately. A typical fit to one of our light curves using 10 equidistant spots is shown in the top panel of Fig. 4.3. Note that each colored curve represent the passing of one spot from the visible hemisphere of the star while the thick red line shows their sum, i.e., the actual model fit of the light curve. The same light curve fitted with a five spot model with

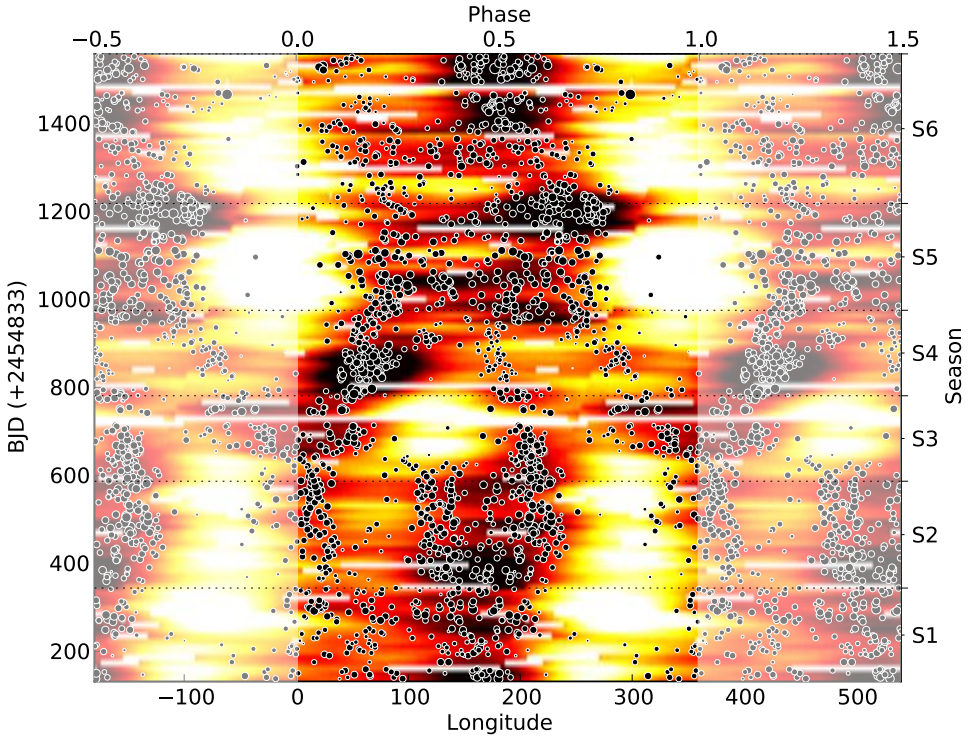

Figure 4.4: The phase folded data, with over-plotted the calculated spot longitudes. The plot is extended half phase in each direction in order to become more readable (shaded areas).

variable positions is shown in the lower planel of Fig. 4.3. One can immediately identify the models for spots #3, #4 and #5. Spot #1 cannot be not seen as it is covered under the combined model (thick red line). It is obvious that without spot #1, which shares the same characteristics with spot #4, the section of the light curve with <947.5 BJD (+2454833.0) would have been impossible to cover. We conclude that one needs about 10 free parameters to arrive at an adequate fit to the observed light curves.

The total light curve is affected by data dropouts in various parts. As a result the number of data available points fluctuates from one light curve chunk to the next. To avoid errors in our calculations we model only those light curve chunks with a phase coverage larger than 70%. The final number of analyzed chunks is thus 379 out of 462. Two adjacent light curve chunks are obviously correlated since they share 75% of their data points, hence, the estimate of the size and longitude for each spot is done more than once. We finally use a MCMC (Marcov-Chain Monte-Carlo) approach to estimate the size and the longitude of each spot, as well as the errors thereof.

4.1.3 Results

4.1.3.1 Spot configurations and stellar "spot seasons"

Since we are interested in localizing the spots on the stellar surface we choose to use a five spot model with variable positions and radii in the following. In Fig. 4.4 we show the results of our spot analysis for Kepler-210 by plotting the calculated positions of the modeled spots vs. time (on the

y-axis). The color-coded plot represents the phase -folded light curve, and the calculated spot longitudes are over-plotted at the appropriate spot longitudes. The size of each dot corresponds to the calculated size of the spot. The star spot sizes and longitudes show some interesting features in the behavior of the spots on Kepler-210. In the following we will refer to time as the number of days elapsed from the date BJD = 2454833.0.

At the beginning of the Kepler observations the activity on Kepler-210 is concentrated into two regions centered at around 0°-20° longitude and 180°-200° longitude. As a result one hemisphere is very active, i.e., the one between 0°-180°, while the other half of the star remains almost spotless. At ∼ day 350 the region at 180° appears to split up in two parts, one apparently moving towards smaller longitudes and the other towards larger longitudes. At day ∼630 the region moving towards smaller longitudes disappears and the region remains spotless for about 200 days. At the same time activity appears at longitude 200°-300°, i.e., a region that was found inactive before. Also, the activity region at 0°-20° starts drifting towards larger longitudes. At day ∼800 the activity in the longitude range 200°-300° disappears again and remains more or less spotless for the rest of the Kepler-210 observations. Between 800 days and 1000 days three activity concentrations are visible, two at about 200° and 300° longitude moving towards smaller longitudes and the already mentioned region at 0°-20° which is now moving towards larger longitudes. Between days 1000 and 1250 the activity appears to be concentrated more and less homogeneously between longitudes 50°-250°. At around day 1200 the activity near longitude 120° starts thinning out and the recognized two activity complexes are drifting towards smaller longitudes. Based on this phenomenology we divide the data of Kepler-210 into six seasons S1 .... S6: S1: 130 days - 350 days, S2: 350 days - 600 days, S3: 600 days - 800 days, S4: 800 days - 1000 days, S5: 1000 days - 1250 days and S6: 1250 days - 1600 days.

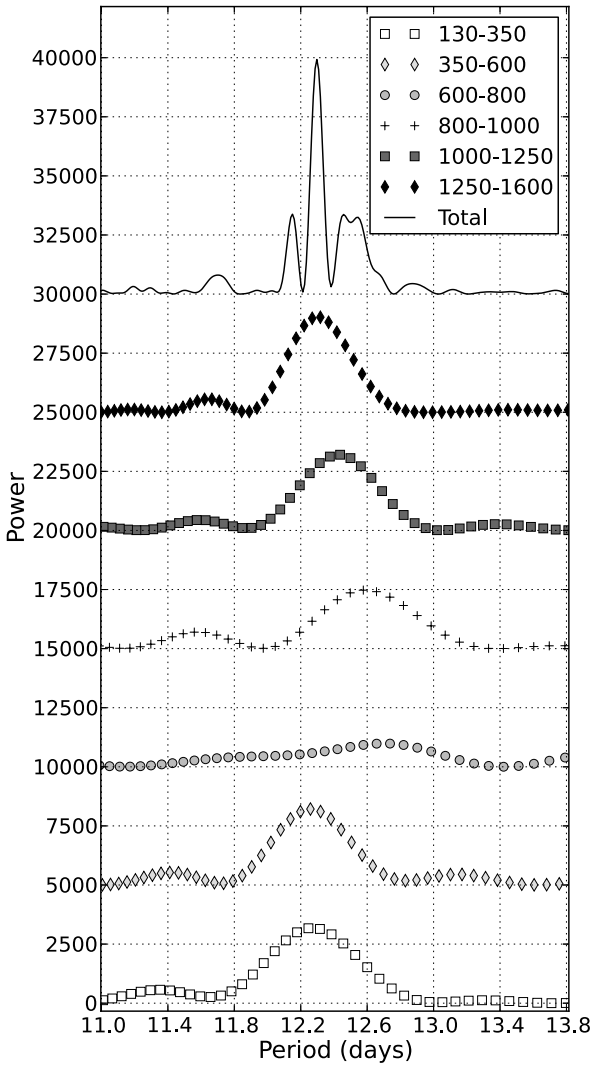

Figure 4.5: The L-S periodograms of each stellar "season". The solid line represents the total L-S periodogram of the light curve. The transition from small periods to longer and then gradually to small again resembles the "*Butterfly diagram*" of the Sun (see Sects 4.1.3.2 & 4.1.4.2).

4.1.3.2 Power spectrum analysis

The introduction of the "seasons" in Sect. 4.1.3 was performed purely phenomenologically. We now calculate the L-S periodogram for each season (shown in Fig. 4.5) and note that the value of the maximum

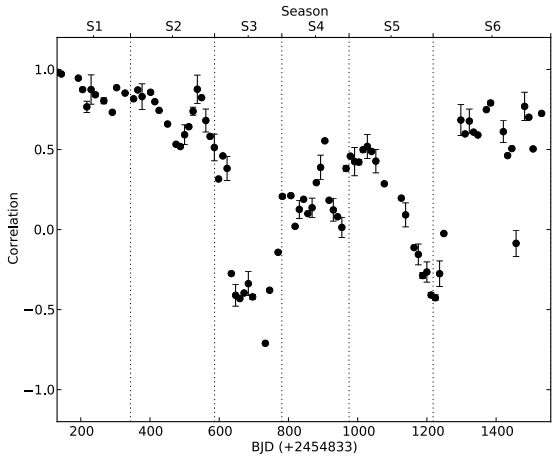

Figure 4.6: Cross-correlation between the different phases with period $P = 12.28$ days. The outlying points in times ∼750 days and ∼1450 days originate to anomalies in the light curve due to the transition from one *Kepler* observation quarter to the next.

power periods varies from season to season, with exception of seasons S1 and S2. The L-S of season S3 has the weakest power, due to the existence of multiple periodicities and the maximum power of this season appears to be at periods slightly larger than 12.6 days. Starting from season S3 and up to S6, there is an obvious diminution of the prominent period value from ∼12.6 days to ∼12.3 days. In general, the period range which we calculate for the different seasons explains the structure of the L-S diagram of the total light curve (continuous line), with exception of the peak at ∼12.1 days, the origins of which we are not able to clarify.

4.1.3.3 Cross correlation between the different light curve portions

Another method adequate to quantify any differences between the observed seasons is to compare the time evolution of the light curve modulations. To that end, we separate the light curve in parts (phases) equal to the leading period of the L-S periodogram (i.e., 12.28 days) following the expression

$$\Phi_{\rm i} = [t_0 + {\rm i}\cdot P\,,\, t_0 + {\rm i}\cdot P + P] \quad \text{with} \quad {\rm i} = 0, 1, 2...N, \tag{4.2}$$

where P, T_0 and N denote the period, the time of the first observation and the total number of phases respectively. In Fig. 4.6 we show the cross-correlation between the different phases $\Phi_{\rm i}$ of the light curve and the phase Φ_0 (reference phase). The error bars are inversely proportional to the common number of points per phase couple, i.e, zero error denotes equal number of points between the reference and the examined phase. In the same fashion as with the L-S periodogram, the seasons are also easily distinguishable in Fig. 4.6, marked by rapid changes in the cross-correlation between the phases.

4.1.4 Physical interpretation

So far we have shown that the rotational period of the active regions of Kepler-210 appears to vary in time. But what is the physical interpretation of the results of Sect. 4.1.3?

4.1.4.1 Active longitudes

There is a clear preference in the longitudes where the spots appear, while other surface areas remain more or less spot-less. Using our algorithm we find that there is an area between 150 and 200 degrees in longitude which is covered by spots in every observed rotation of the star. On the other hand about 100 degrees in longitude are covered by spots only during 20% of the total observation time.

4.1.4.2 Differential rotation

As discussed in Sect. 4.1.3, the leading period of the activity modulations of each season is different (cf., Fig. 4.5). Thus, in agreement with the claims of Reinhold et al. (2013), we interpret those changes as evidence for differential rotation. Our argument is supported also by the visible drifts of active regions in Fig. 4.4; the spot groups with larger peri-

ods than the phase folding period (P = 12.28, cf. Fig. 4.5), appear with a small delay from one phase to the next, while the spot groups with shorter periods appear earlier. A nice example of such motions can be found in season S4, between 800 and 1000 days.

Assuming a solar like differential rotation pattern, i.e., longer rotation periods near the equator, the difference in periods can be directly linked to differences in stellar latitude: Spotted areas with smaller periods must then be located closer to the equator, while the spots with longer periods should be located further away from the equator and more closely to the poles.

A characteristic of the Fig. 4.5 worth mentioning is the "jump" of the spots from small latitudes (season S2) to larger latitudes (season S3), which is then followed by a smooth "migration" of the spots back to smaller latitudes. This behavior resembles the behavior of sun spots as they appear in the famous "*Butterfly Diagram*" for the Sun. During an 11-year magnetic cycle, the latitudes of the appearing sunspots first increase rapidly and then, gradually, move closer to the equator.

Given the fact that the peak to peak amplitude of the modulations is not reduced dramatically during season S3, we assume that the maximum latitude $\phi_{\max}$ of the spots ought to remain close the equator of the stellar disk, in order for the reduction of the spotted areas (due to their projection) to remain insignificant. To test the above hypothesis we calculate the differential rotation α as a function of the stellar latitude ϕ using the equation

$$\alpha = \left(1 - \frac{P_{\rm eq}}{P_{\rm obs}(\phi)}\right) \cdot \frac{1}{\sin^2 \phi}, \qquad (4.3)$$

where $P_{\rm obs}(\phi)$ is the rotational period at a given stellar latitude ϕ and $P_{\rm eq}$ denotes the equatorial rotational period. In Fig. 4.7 we plot our estimates for the differential rotation assuming different stellar latitudes ϕ for spots with rotational period 12.6 days (i.e., the spots which are assumed

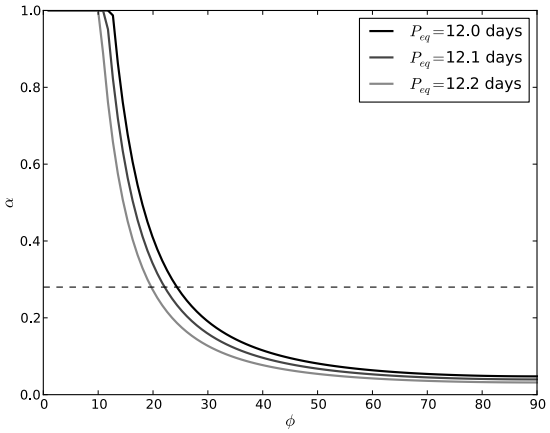

Figure 4.7: Estimate of the differential rotation α of the star, assuming spots with rotational period $P_{\rm rot} \simeq 12.6$ days for latitudes between 0° and 90°. The dashed line indicates the value of the differential rotation of the Sun.

to be responsible for the peak close to ∼12.6 days in the L-S of season S3) given three different values for the equatorial rotation period of the star. The dashed line in the same digram indicates the value of the solar differential rotation, i.e., ∼ 0.28 (Howard & Harvey 1970, Snodgrass & Ulrich 1990). Figure 4.7 suggests that the spots of season S3 with rotational period $P_{\rm rot} \simeq 12.6$ days ought to have latitudes in the range between $25^\circ \lesssim \phi_{\max} \lesssim 35^\circ$ while the differential rotation of the star is similar and slightly smaller in comparison to the differential rotation of the Sun.

During Season S3 another abnormal event takes place: It is the only time during the Kepler-210 observations, when the area between ∼200° and ∼360° is covered by spots. In the same time the rest of the usually spotted stellar surface becomes free of spots. Although the connection of this event to a physical process might not be trivial, it is an evidence that a dramatic change happened to the star during that season (see, Fig. 4.4).

4.1.4.3 Spot formation and spot life times

The observed flux variations of Kepler-210 are similar from one rotation to the next (cf., Figs 4.6).

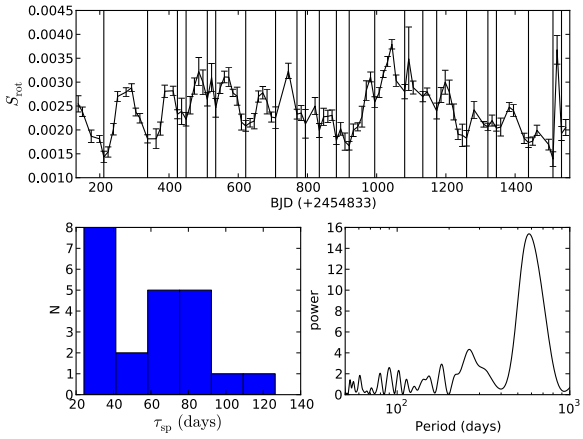

Figure 4.8: Top: The evolution of the size of the total spotted area, calculated as the summed area of the spots which define the model for each light curve chunk. The vertical lines indicate the local minima of the curve. Bottom-left: The distribution of the spot life times (see text for details). Bottom-right: The L-S periodogram for the evolution of the spotted area size.

The latter fact suggests that the life time $\tau_{\rm sp}$ of the active regions is much longer than the stellar rotation period $P_\star$.

In Figs 4.1 we observe parts of the light curve where the peak to peak amplitude of the modulation is larger. Due to the lack of a plateaued part in the light curve we conclude that there is no time, during the *Kepler* observations of Kepler-210, with complete absence of spots on the visible hemisphere of the star. As a result we assume that the short term variations of the total spot coverage are the result of simultaneous occupation of stellar longitudes closer than the half visible hemisphere from different spot groups.

There are two possibilities for such an association to occur; either a spot appears in an area with a neighboring longitude to a preexisting spot or two spots with different stellar latitudes "meet" due to their differential rotation. From a visual examination of Fig. 4.4, we observe that both effects are taking place, with the former effect being more dominant. Therefore we suggest that it is possible to estimate the life time of the spots by measuring the duration of the simultaneous appearance of spot groups in the visible stellar hemisphere.

Using the estimated spot radii we can calculate the total covered area ($S_{\rm rot}$) for each of the light curve chunks (see, Sect. 4.1.2.2 for details). The top panel of Fig. 4.8 shows the evolution of the total covered area as a function of time. As the duration of each fluctuation we consider the range between two local minima of the covered area curve, which are marked with vertical lines in Fig. 4.8.

In the lower left pane of Fig. 4.8 we show the suggested spot life time distribution which ranges between ∼25 days and ∼130 days. There are two maxima, one close to ∼25 days and an other around ∼90 days. After visual examination of Fig. 4.4 we can confirm that the duration of the dark features (spotted areas) varies between ∼60 days and ∼90 days. The peak close to ∼25 days (see, Fig. 4.8) is probably a bias caused by the detection of consecutive local extrema in the curve of the total covered area.

The L-S periodogram of the spotted area, shown in the lower right panel of Fig. 4.8, shows several low significance peaks for periods in the range between ∼60 days and ∼90 days. The most significant peak is found for a period around ∼600 days.The long term variation responsible for this peak is visible in the upper panel of Fig. 4.8, where the total spotted area appears to become larger close to the end of season S2, then drops for seasons S3 and S4 and raises again in season S5.

4.1.5 Conclusions

Using the phenomenology of the Kepler-210 light curve in combination with the results of a five spot model, we study the behavior of the spotted areas on the star (i.e., their relative periods and the longitudes at which they appear) and their changes with time (cf., Fig. 4.4). Based on the spot phenomenology we identify six different "spot seasons" and demonstrate that there are differences in the dominant periods of the L-S periodograms corresponding to each season (cf., Fig. 4.5). Addition-

ally we show that the seasons also manifest themselves as differences in the correlation between the corresponding parts of the light curve (cf., Fig. 4.6).

According to Fig. 4.5, the relative period of spots in the subsequent seasons appears to change in the same fashion as the relative rotational period of sunspots during the solar cycle, i.e., the relative starspot period appears to change from lower to higher values between seasons S2 and S3, while it diminishes gradually from season S4 until the end of the *Kepler* observations. A common characteristic between all seasons, with the exception of seasons S3 and S4, is the persistent appearance of the spots in a specific longitude range of the star.

Additional observations of Kepler-210 are needed in order to conclude if this behavior is the result of a magnetic cycle. However assuming solar-like differential rotation, we show that the value of the differential rotation α should be similar or lower to that of the Sun, while the spots with the higher period should have latitudes in the range between $25^\circ \lesssim \phi_{\max} \lesssim 35^\circ$ (see Fig. 4.7). Furthermore, we estimate the spot life times using the radii of the spots which were computed with our model fit. As a result we find that the life time of the spots of Kepler-210 varies between $\sim$60 days and $\sim$90 days (see Figs 4.4 & 4.8).

The behavior of the active regions on the photosphere of Kepler-210 (i.e., the shift from small asterographic latitudes to higher and vice versa) is comparable to the migration of sunspots during an 11-year solar magnetic cycle (cf., Fig. 4.5). We estimate that the duration of this phenomenon on Kepler-210 is similar or somewhat longer than the total *Kepler* observation time (i.e., 4 years), however, additional long-term observations are clearly needed to check whether this behavior of Kepler-210 as observed by *Kepler* is actually periodic and the result of a magnetic cycle.

4. Ioannidis & Schmitt: *Sneak peeking at stellar surfaces II: Spot evolution and differential rotation of the planet host star Kepler-210*

4.2 "*Sneak peeking at stellar surfaces: Origins of the photometric modulations and timing variations of KOI-1452* ",

P. Ioannidis and J. H. M. M. Schmitt

Submitted for publication in Astronomy & Astrophysics

4.2.1 Introduction

One of the most efficient ways to study the physical parameters of an exoplanet is by studying their transits in front of their parent star. As shown by Agol et al. (2005), it is even possible to infer the existence of additional low mass and otherwise unobservable companions with the measurement of the mid-transit times and their deviations from linear period ephemeris. Depending on the actual planetary configuration such Transit Timing Variations (TTV) can reach differences up to a few hours w.r.t. the linear period ephemeris of the planet, especially for systems close to low order mean motion resonances. Although additional system components can also be inferred from precise radial velocity (RV) measurements, the importance of the TTV method increases with the number of planets around fainter stars, where the quality of RV measurements is decreasing. While the measurements of TTV are possible with ground-based observations, the high accuracy, continuous light curves from the *CoRoT* (Baglin et al. 2006) and *Kepler* (Koch et al. 2010) space missions provide evidence for statistically significant TTV in more than 60 cases.[1]

Despite its success the study of exoplanets with the method of transits using high precision photometry can be somewhat problematic in the case of active host stars. The transit profile of planets orbiting around spotted stars become distorted when the planet is passing over dark star spots during its transit (e.g., Rabus et al. (2009), Wolter et al. (2009)). The severity of this effect can be such that quite large systematic errors are introduced in the calculation of the physical parameters of the planets (cf., Czesla et al. (2009) and Oshagh et al. (2013)). Furthermore, Ioannidis et al. (2016) show that the influence of such spot-crossing events on the estimates of the mid-transit times of a planet can lead to statistically significant false positive TTV detections under certain conditions, and there are several cases where the detected low amplitude TTV are actually believed to be caused by spot-crossing events (e.g. Sanchis-Ojeda et al. (2011), Fabrycky et al. (2012), Szabó et al. (2013), Mazeh et al. (2013)).

The identification of the spot-crossing events and their correlation with the TTV of a planet can be cumbersome, especially for planets with small periods and thus large number of transits. Here we show that the method of unsharp masking, i.e., examining the transit light curve produced by subtracting out the mean transit model (cf., Sect. 4.2.2) is a suitable tool to compare the measured $O-C$ mid-transit time variations with the transit light curves and to identify correlations between the occurrence of spot-crossing events and the measured TTV. In order to demonstrate the power of this method we present a case study of the TTV of KOI-1452 in sect. 4.2.3, and finally we discuss our results in sect. 4.2.4 and summarize with our conclusions in sect. 4.2.5.

[1] According to data list acquired by the web page http://exoplanet.org

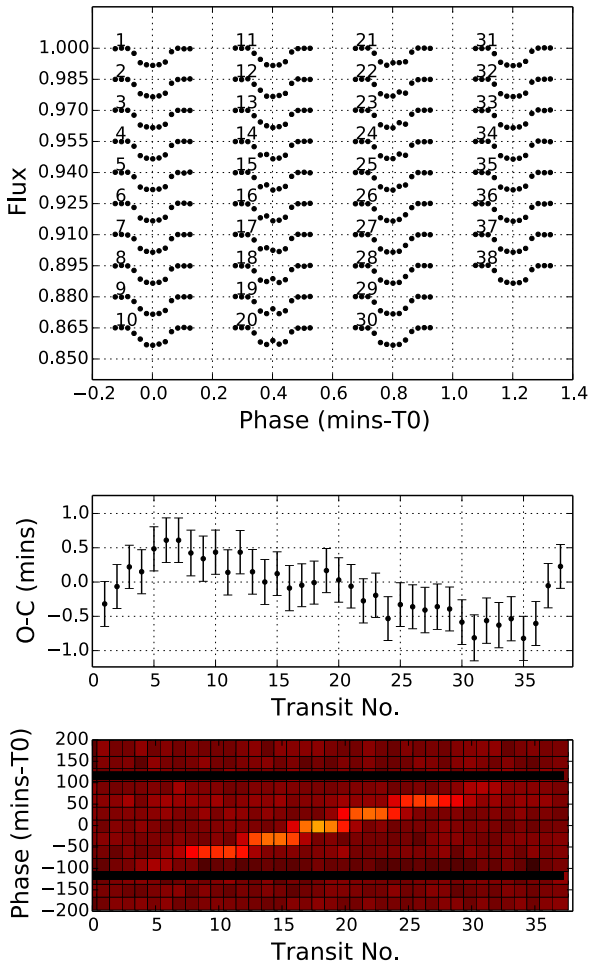

Figure 4.9: Top: Consecutive simulated transits of a planet with an orbital period $P_{\rm orb}$ = 1.0132 $P_{\star}$. Each light curve is affected by spot crossing events; see text for details.
Middle: Estimated mid-transit times of the transits in the top panel. The sinusoidal shape of the $O-C$ diagram is the result of spot crossing anomalies in the transits Ioannidis et al. (2016).
Bottom: Unsharp masking transit residuals of the planet; note the correlation with the sinusoidal O-C diagram in the middle panel.

4.2.2 Unsharp masking of transit light curves

As discussed by Ioannidis et al. (2016), when planets cross over cool star spots during the transit, the resulting transit profiles show an increment of stellar flux compared to a "pristine" un-spotted transit. Due to the continuous evolution of starspots, these spot-induced in-transit anomalies cannot be included in the model fit of the transit light curve. As a result, the spot crossing events can potentially alter the mid-transit time estimate, which is derived using a spot-free transit light curve. The position of the spot crossing event in the transit profile influences the amplitude and the sign of the spot-induced variation. The resulting maximal amplitude of this fake TTV depends on the physical properties of the star, the planet and the spot.

In consecutive transits of the same planet the position of the spot crossing event can change from one transit to the next, depending on the period ratio between the orbital period $P_{\rm orb}$ and rotational period $P_{\rm rot}$ of the star. Fake TTV may result if $P_{\rm orb}$ and $P_{\rm rot}$ are not identical. In particular, the time needed for a spot to cross the total transit profile is equal to half of the beating period and it is given by the expression

$$D_{\rm sp} = \frac{P_{\rm orb}}{2} \cdot \left(\frac{P_{\rm orb}}{P_{\rm rot}} - 1 \right)^{-1}, \qquad (4.4)$$

assuming parallel orbital and rotational axes Sometimes it is useful to express the value of $D_{\rm sp}$ from eq. 4.4 in terms of the number of transits needed for a spot crossing, which is given by

$$D_{\rm sp\_tr} = \frac{D_{\rm sp}}{P_{\rm orb}}. \qquad (4.5)$$

The sign of $D_{\rm sp}$ value is related the direction of the spot motion: If $D_{\rm sp}>0$, the spot crossing events occur in the direction from transit ingress towards egress ($P_{\rm orb} > P_{\rm rot}$) and vice versa. We note that this relation between the sign of $D_{\rm sp}$ and the spot motion in consecutive transits is valid for a pro-

grade planetary orbit; in the case of a retrograde orbit the above correlation is reversed.

To demonstrate the effects of spot crossing events we carry out a simulation of a sequence of transits with a spot crossing event. The simulation is geared towards a typical transit signal-to-noise ratio (TSNR) and integration times of a long cadence *Kepler* light curve of a star with magnitude $K_p = 13$ mag (Jenkins et al. 2010). We specifically assume a ratio between the orbital period of the planet $P_{\rm orb}$ and the rotational period of the star $P_{\rm rot}$ of $P_{\rm orb}/P_{\rm rot} = 1.0132$. We further assume a dark star spot ($R_{\rm sp} = 0.06\,R_\star$) on the visible hemisphere and kept fixed on the stellar surface, which is occulted by the planet ($R_{\rm pl} = 0.08\,R_\star$) during every consecutive transit. The resulting transit light curves are shown in the top panel of Figure 4.9. Since orbital and rotational periods differ slightly, the position of the spot crossing event slowly changes from one transit to the next, which leads to changes in the derived mid-transit times shown in the middle panel of Fig. 4.9.

The identification of the spot crossing events and the correlation of their occurrence and in-transit position to the $O-C$ diagram is one of the most efficient ways to distinguish between real and spot-induced TTV. Although we know that the $O-C$ variations in Fig. 4.9 are produced by spot crossing events, it is not trivial to locate the in-transit anomalies which are responsible for each one of the TTV. Given the correct global parameters for the transit model, the light curve residuals, calculated by subtracting the model from the data, should appear featureless and just show uncorrelated noise. Yet, when spot crossing events occur, clearly visible features appear (cf., Fig. 4.9, bottom panel), which are straightforward to identify and using the unsharp masking method allows for an easy juxtaposition of the in-transit anomalies with the $O-C$ diagram; furthermore it can reveal important informations regarding photospheric structures (e.g., cold spots) in the band of the star that is occulted by the planet.

4.2.3 Application: KOI-1452

4.2.3.1 Light curve analysis

In the following we apply the unsharp masking technique to the *Kepler* data of KOI-1452. KOI-1452 was first listed as planet host candidate by the *Kepler* satellite survey after the identification of a transit-like signal with a period of $P_{\rm orb} = 1.1522$ days. We show the *Kepler* light curve of KOI-1452 in in the upper panel of Fig. 4.10, which demonstrates that in addition to the transit-like signals (marked with ticks) the light curve of KOI-1452 shows significant modulations on the order of $\sim$2%, suggesting an active star like CoRoT-2 (cf., Huber et al. 2009). Analyzing these modulations with a Lomb-Scargle (L-S) periodogram (Zechmeister & Kürster 2009), shown in the middle panel of Fig. 4.10, we find a plethora of significant periodicities with the most prominent peak at $P_{\rm rot} \simeq 1.516$ days, and the equally separated peaks in the frequency domain with periods smaller than one day can be identified as harmonics of the orbital period P_{orb}.

Soon after its detection with the *Kepler* satellite, the KOI-1452 system was, however, marked as a stellar binary system due to the presence of visible secondary eclipses in its light curve. In Fig. 4.11 we show the primary (upper panel) and secondary (lower panel) eclipses of KOI-1452, phase folded using the calculated period $P_{\rm orb}$ =1.152 days; the model shown as red curve in Fig. 4.11 is constructed

Table 4.1: System parameters for KOI-1452.

Period (days)	$1.152 \pm 7{\cdot}10^{-6}$	this work
R_B/R_A	0.122 ± 0.002	this work
a/R_A	2.858 ± 0.012	this work
i	$73.189^\circ \pm 0.085^\circ$	this work
L_B/L_A	$7.14 \times 10^{-4} \pm 3.53 \times 10^{-4}$	this work
M_A ($M_\odot$)	1.6 ± 0.3	this work
M_B ($M_\odot$)	0.2 ± 0.1	this work
a (au)	0.0265 ± 0.0015	this work
$T_{\rm eff_A}$ (K)	7268 ± 487	Armstrong et al. (2014)
$T_{\rm eff_B}$ (K)	3582 ± 546	Armstrong et al. (2014)

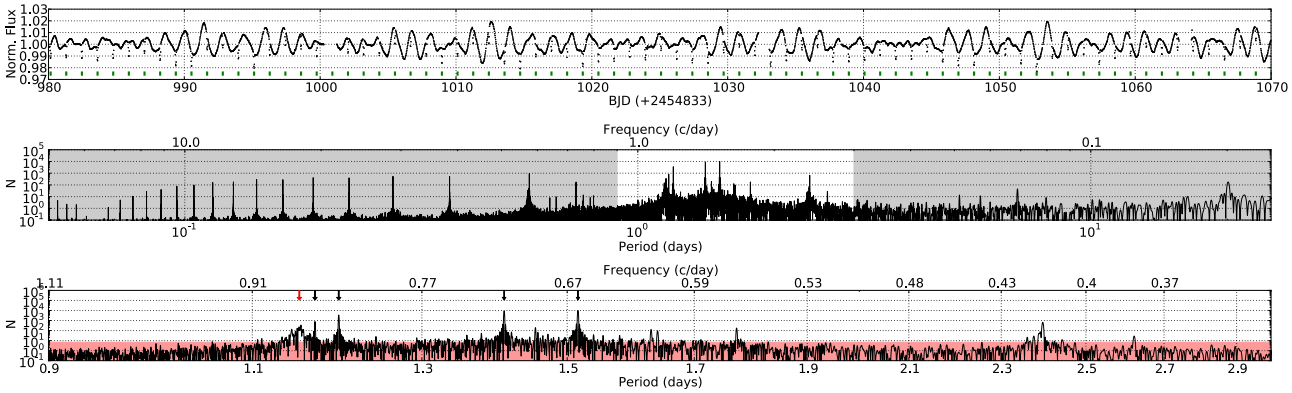

Figure 4.10: Top: Part of KOI-1452 light curve. There are clear periodic variations suggesting the appearance of spots in the visible stellar hemispheres (see text for details). The primary eclipses are marked with green markers.
Middle: The L-S periodogram of the total *Kepler* light curve. The unshaded part around the area with the most significant periodicities is shown enlarged in the lower panel.
Bottom: The red shaded area shows the values of the periodogram with false alarm probability higher than 10^{-3}. The four most prominent periods of the L-S periodogram with periods of $P_1 = 1.516$ days, $P_2 = 1.4097$ days, $P_3 = 1.1978$ days and $P_4 = 1.1702$ days are marked by black arrows, while the red arrow indicates the orbital period of the system ($P_{\rm orb} = 1.1522$ days).

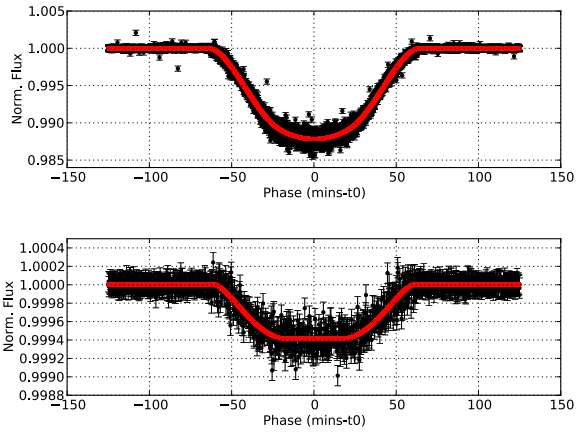

Figure 4.11: Phase folded primary (top) and secondary (bottom) eclipses of KOI-1452 (black dots) and the global eclipse model (red line); see text for details.

using the analytical eclipse light curve model by Mandel & Agol (2002) and a summary of our model fit results is given in Table 4.1. Clearly, the shape of the primary eclipse looks very similar to that of a planetary transit. The model of the secondary eclipse (red curve in the lower panel of Fig. 4.11) requires identical parameters as the model calculated from the primary eclipse, assuming an inverted flux ratio and zero limb-darkening coefficients. We finally note that the increased dispersion of the in-transit data points is an indication of spot crossing events in the light curves (see, Czesla et al. (2009)).

4.2.3.2 Stellar characteristics

Due to the fact that the durations of both eclipses are identical (cf., Fig. 4.11) we are confident that the orbit of the binary system is circular, while the flat-bottom shape of the secondary eclipse shows that the fainter companion is totally eclipsed by the primary star. Retrieving radial velocity (RV) data for the KOI-1452 system from the public archive CFOP (https://cfop.ipac.caltech.edu) and folding the data with the orbital period $P_{\rm orb} = 1.1522$ days, we can construct an (admittedly sparse) RV curve for KOI-1452 shown in the top panel of Fig. 4.12,

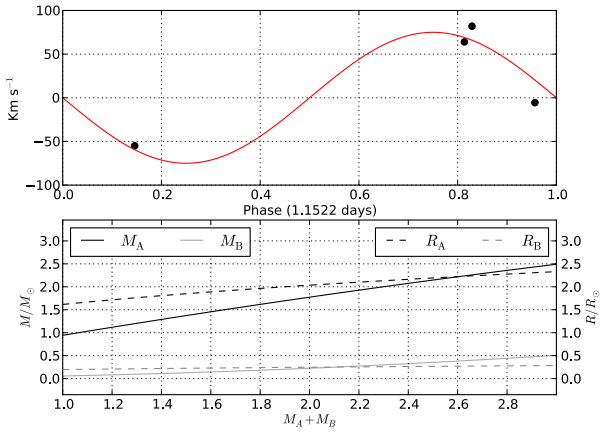

Figure 4.12: Top: Radial velocity measurements of KOI-1452 phased with the orbital period $P_{\rm orb}$ = 1.1522 days. The red line shows the expected RV curve for a system of an F-type and an early M-type star, primary eclipses occur in phase zero. The expected RV amplitude of K$\sim$ 75 $km\,s^{-1}$ agrees well with the data, excluding the possibility for the companion to be a planet.
Bottom: Estimated masses (solid lines) and radii (dashed lines) for the components of the system as a function of the total mass $M_A + M_B$; see text for details.

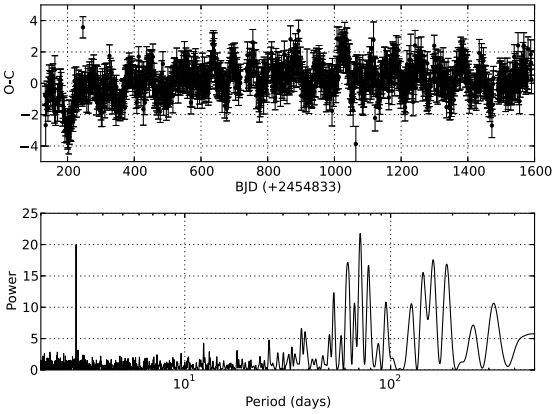

Figure 4.13: The $O-C$ diagram of KOI-1452 (top) and its L-S periodogram (bottom). Many significant signal periods between 60 and 100 days appear, the peak close to 3 days is caused by the data sampling.

which suggests a RV semi-amplitude of K$\simeq$ 75 $km\,s^{-1}$. With this value of K we use the mass function and Kepler's third law in combination with the measured values for the orbital inclination i and radius ratio R_B/R_A (see, Table 4.1) to calculate an estimate for the components' masses and radii of the system components as a function of the assumed total system mass. The resulting curves are shown in the lower panel of Fig. 4.12. Using the observed color index ($B-V \simeq 0.4$), we can set a constraint for the total system mass in the range $1.6\,M_\odot \lesssim M_A + M_B \lesssim 2.2\,M_\odot$. For values of total mass outside this range the expected mass-radius combinations appear to be unusual.

Comparing the flux reductions observed during the primary and secondary eclipse, we calculate the ratio of the effective temperatures of the two components as $T_{eff_A} = 2.11\ T_{eff_B}$. This estimate is in good agreement with the $T_{\rm eff}$ values calculated by Armstrong et al. (2014).

Taking into account the masses and radii estimates (cf., Fig. 4.12) in combination with the ratio of the effective temperatures we argue that the system consists of a slightly inflated F-type star and an M-dwarf star.

4.2.3.3 False positive timing variations

The preparation of the *Kepler* light curves and the eclipse timing variation (ETV) analysis follow the same principles described by Ioannidis et al. (2016). In the top panel of Fig. 4.13 we plot the $O-C$ diagram of KOI-1452[1], which shows clear variations with an amplitude of ∼2-3 mins (Mazeh et al. (2013) and Szabó et al. (2013)). In addition, the LS-periodogram (Zechmeister & Kürster 2009) of the derived $O-C$ values, shown in the bottom panel of Fig. 4.13, reveals a variety of high power

[1]The system was introduced to us by Dr. Howard M. Relles, http://exoplanet-science.com

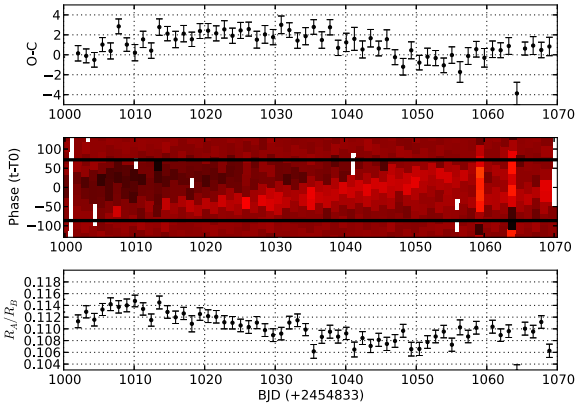

Figure 4.14: Top: Part of $O-C$ diagram of KOI-1452 between 1000 days $\leqslant$ BJD (+2454833) $\leqslant$ 1070 days.
Middle: Concurrent unsharp masking transit light curve residuals. The bright stripe is due to spot crossing anomalies, which change their position from one transit to the next due to the small period difference (cf., Fig. 4.9). The white areas indicate no data. The black lines indicate the first and fourth contact of the eclipse.
Bottom: Variation of the measured radii R_B/R_A for each eclipse. During the strongest observed TTV the star appears to be larger because of spot coverage during the transit (Czesla et al. 2009).

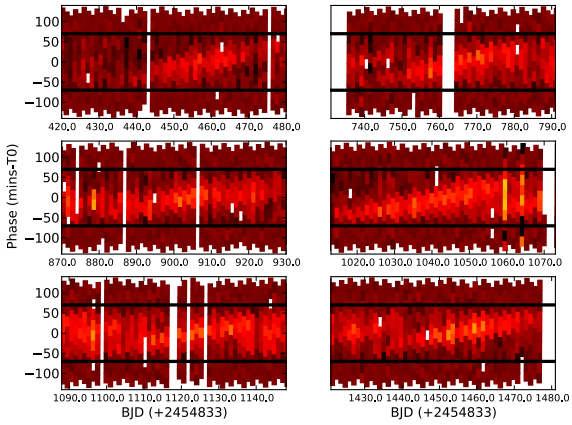

Figure 4.15: Collection with the clearest spot crossing features from the light curve of KOI-1452; white regions are due to data absence. The black lines indicate the first and fourth contact of the eclipse.

periodicities, with the most prominent peak at a period P_{O-C} ≈71 days. The coordination of the rotation period of the system, in combination with the small number of in-transit points, periodically affect the mid-transit timing measurements; this effect is visible as the high peak close to ∼3 days in the L-S periodogram.

In Fig. 4.14 we zoom in on a small portion of the $O-C$ diagram of KOI-1452 in that part of the light curve between 1000 days $\leqslant$ BJD (+2454833) $\leqslant$ 1070 days to juxtapose the phased light curve residuals with the the $O-C$ diagram and the derived stellar parameters. We choose this particular part of the light curve since in that time period the clearest features in the $O-C$ diagram are found. The bright, stripe-shaped feature is the result of many spot crossing events, which appear in different, in-transit positions due to the small difference between the orbital and rotational periods. A comparison between the $O-C$ diagram and the phased unsharp masked light curve shows that the ETV occur at the same time as those features, in good agreement with our simulations (cf., Fig. 4.9). The discrepancies of the $O-C$ diagram and our simulation are introduced by other spots, in different positions in the transit profile (e.g., a new feature appears in the phased color-plot after BJD (+2454833) $\simeq$ 1040 days).

As a second step we calculate the depth for each observed eclipse; the relative measurements for KOI-1452 are presented in the bottom panel of Fig. 4.14. According to Czesla et al. (2009), the presence of cold spots during the transit of a planet, or in this case the eclipse of an other "cold" star, can cause an overestimate of its radius. As a result, when the occulting body appears to be larger than average (increased transit/eclipse depth), the possibility of a spot crossing event occurrence also becomes large. The comparison of the bottom panel of Fig. 4.14 with the top and middle panels shows the correlation of the individual occultation depths

with the measured ETVs of the system and the existence of spot crossing events, respectively.

Spot crossing events are visible during the total *Kepler* light curve of KOI-1452, with similar characteristics and correlation to the measured ETV and eclipse depth. Additional examples of such spot crossing events in the eclipses of KOI-1452 are shown in Fig. 4.15.

4.2.4 Discussion

4.2.4.1 The different periods of KOI-1452

Given our results presented in Sect. 4.2.3, it is very clear that we are dealing with an eclipsing binary system as already known prior to our study. As far as the observed light curve modulations of KOI-1452 are concerned, the most straightforward interpretation would attribute them to starspots and one would interpret the different peaks in the L-S diagram as indicators of differential rotation (e.g., Reinhold et al. 2013). Also, if KOI-1452 was a very active star as suggested by its *Kepler* light curve (cf., Fig. 4.11), one would also expect spot crossing events as observed, for example, for CoRoT-2 (e.g., Wolter et al. 2009), and, indeed, our unsharp masking analysis (cf., Fig. 4.14 and Fig. 4.15) does suggest spot crossing events. Considering the spots affected by the spot crossing events using the average of the $D_{\rm sp}$ values of the spot crossing features shown in Fig. 4.15, we estimate $D_{\rm sp} \simeq 35 \pm 5$ days; note that the sign of $D_{\rm sp}$ is positive as we observe the spots to drift with direction from ingress to egress (see, Sect. 4.2.2). Using Eq. 4.4 we then compute the period of the spots responsible for the spot crossing features in the eclipses of KOI-1452 as $P_{\rm rot} = 1.1357 \pm 0.003$ days, assuming a prograde orbit, or $P_{\rm rot} = 1.1687 \pm 0.003$ days, assuming a retrograde orbit.

Given the short period and small separation between the system components (see, Table 4.1) it is reasonable to assume that the two stars are tidally locked, i.e., the rotational periods of (actually both) stars coincide with the orbital period of the system, and thus the rotational period ought to be close to 1.15 days. However, the highest peak in the LS periodogram is found at $P_{\rm rot} \simeq 1.512$ days (cf., Fig 4.10). If this peak was produced by star spots rotating with this period, these spots cannot be responsible for the spot crossing events observed in the transits of KOI-1452, since for such a period ratio the difference between the transit positions of the spots in consecutive transits would be much higher. Using Eq. 4.5 we calculate that a spot with a period of $P_{\rm rot} \simeq 1.512$ days requires $D_{\rm sp\_tr} = -1.6$ rotations in order to cover the total transit profile, which would lead to two problems: First, such spots would not be visible continuously from one rotation to the next resulting in completely different ETV patterns and spot crossing features, and second, the spots should occur with a direction from egress to ingress, opposite to the direction they appear to drift (cf., Fig. 4.15).

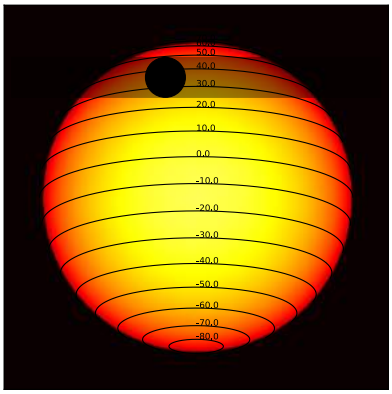

Figure 4.16: Artist's impression of the KOI-1452 system during a primary eclipse. The horizontal lines indicate the latitudes of the system's primary, which appears tilted according to our hypothesis of zero system obliquity. The semi-transparent band represents the latitudes occulted during an eclipse.

4.2.4.2 Differential rotation ?

In Fig. 4.16 we show an artist's impression of the KOI-1452 system during a primary eclipse, using

the estimated orbital characteristics shown in Table 4.1 and assuming that rotational and orbital angular momenta are aligned. The semi-transparent black band represents the eclipsed part of the primary in the stellar latitude range between $25\circ \lesssim \phi_\star \lesssim 50\circ$. The equatorial regions at $0\circ$ are assumed to rotate with a period of 1.15 days.

It is hard to see where regions rotating with 1.51 days should be located on the star, also the level of differential rotation required (period difference of ∼30% between neighboring latitudes) is very large. Balbus & Weiss (2010) discuss the possibility of zonal stellar surface flows, i.e., flows similar to those observed on the surfaces of the giant planets in our Solar system. Following this hypothesis, one would have to account for the non linear evolution of the differential rotation along the stellar latitude. As a result one might explain the required rapid alternations in the rotation period. Also, in the case of the giant planets in the solar system the velocity differences observed in the zonal bands are in the percent range, but not 30%.

An even more exotic hypothesis would be that the differential rotation of the star is opposite to that of the Sun, i.e., the star rotates more slowly in the equator. Anti-solar differential rotation would explain the fact that the spots occulted by the companion spots, which are slower, appear in high latitudes. In addition it would explain the dominance of the slow spots in the modulations of the light curve, as they would appear closer to the equator and thus larger (due to projection effect). Although this is a fitting explanation, anti-solar differential rotation is proposed for evolved stars (Brun & Palacios 2009).

4.2.4.3 Gravity-mode pulsations ?

Both the area of the Hertzsprung-Russell diagram, where the main component of the KOI-1452 system is located, and the nature of the periodicities found in the *Kepler* light curve make it a candidate for a γ Dor type variable star. Such stars are slightly more massive than the Sun (1.4-$2.5 M_\odot$) and show multi-periodic oscillations with periods between 0.3 and 3 days, which are the result of gravity-mode (g-mode) pulsations (e.g., Kaye et al. 1999). The mechanism responsible for the g-mode pulsations is related to the fluctuations of the radiative flux at the base of the convective envelope of the stars (Guzik et al. 2000). Assuming a non-rotating star with a chemically homogeneous radiative envelope, one should expect pulsations with identical spherical degree l and a variety of radial orders n with equidistantly spaced periods (Tassoul 1980). Furthermore, stellar rotation introduces frequency splitting, which results in separated period spacing patterns, relative to the azimuthal order m. Van Reeth et al. (2015) present a survey of a few dozen of γ Dor variable stars. While the majority of these stars have a little shorter pulsation periods and have period spacings again somewhat shorter than the period spacing of P = 0.1063 days observed for KOI-1452 (cf., bottom panel of Fig. 4.10), the observed parameters for KOI-1452 do not fall completely outside the range observed for γ Dor variable stars. While an in-depth asteroseismic analysis of KOI-1452 is beyond the scope of this paper, the hypothesis that stellar pulsations and not stellar activity is responsible for the observed light curve modulations of KOI-1452, appears to be the simplest hypothesis and would not require the introduction of somewhat exotic differential rotation scenarios. Yet, the spot crossing events visible in the primary eclipses of the binary suggest that in addition there must exist activity modulations which are probably described by the part of the L-S periodogram in the period range between 1.13 days and 1.17 days.

4.2.4.4 Retrograde orbit ?

The assumption that the most dominant features in the L-S periodogram of the KOI-1452 system are the result of g-mode pulsations could explain the large discrepancy between the measured periodicities, i.e., the difference between $P_{\rm orb}$ and P_1 in Fig. 4.10. However, the fact that the spot cross-

ing features in the eclipses of KOI-1452 rotate with $P_{\rm rot} = 1.1357 \pm 0.003$ days or $P_{\rm rot} = 1.1687 \pm 0.003$ days, assuming a prograde or retrograde orbit respectively, requires some additional discussion.

The assumption that the stars are tidally locked and the equatorial rotation of the main star is equal to the value of $P_{\rm orb}$ requires a non-solar differential rotation law in order to explain the existence of high latitude spots with smaller rotational period than the orbital period, and thus equatorial period of the star. However there is no feature in the L-S periodogram close to period with value $P_{\rm rot} = 1.1357 \pm 0.003$. Yet one does find a peak in the L-S periodogram at a period $P_{\rm rot} = 1.1687 \pm 0.003$. Since the value of this peak is very close to the suggested rotational period of the occulted spots $P_{\rm rot} = 1.1687 \pm 0.003$ days, it is tempting to identify the two, however, this requires to assume that the primary star rotates in the opposite direction of the orbital motion of its companion, which is in contradiction to the hypothesis of tidal locking.

4.2.5 Summary

In this paper we discuss the technique of unsharp masking as a tool for transit light curve analysis in order to locate spot crossing anomalies and compare their occurrence with the estimated $O - C$ diagram of the mid-transit times. We apply the method to the *Kepler* light curve of KOI-1452, where we show the correlation between the timing variations and spot crossing events in the primary eclipses of the system.

Furthermore, we use the same method to show that it is possible to extract information about the properties of the spots which are occulted during a transit/eclipse. As a result we argue that the spots occulted by the faint companion in the KOI-1452 system are very likely not responsible for the modulations in the *Kepler* light curve of KOI-1452. We argue furthermore that the hypothesis that KOI-1452 is a γ Dor variable can naturally explain the light curve variability for periods of 1.19 days and larger, while star spots are responsible for the spot crossing events in the primary eclipses of the system and might explain the 1.17 days feature in the periodogram. Clearly, ground-based observations are called for to better determine the physical parameters of the KOI-1452 system. A more densely sampled RV curve would yield more precise estimates of the component masses, a high-resolution spectrum would allow a better estimate of the effective temperature, and finally, a measurement of the Rossiter-McLaughlin effect during primary eclipse would elucidate the rotational properties of the primary component of KOI-1452.

4. Ioannidis & Schmitt: *Sneak peeking at stellar surfaces: Origins of the photometric modulations and timing variations of KOI-1452*

Chapter 5

Beating down the scintillation noise

5.1 Motivation

So far I have presented the results of my research regarding extrasolar planets around active stars, using photometric observations data from space based telescopes. There are two main reasons for the superiority of the observations from space in comparison to observations from Earth based telescopes: the ability to observe, usually uninterruptedly, parts of the sky for large amounts of time and the high accuracy of the observations due to the lack of the atmosphere.

Due to the alternation between day and night, in addition to the variations of the weather conditions over any ground based observatory, it is not possible to perform uninterrupted, long term observations. Likewise it is impossible to avoid the effects which are introduced to the photometric light curves of the stars as a result of the atmospheric turbulence, even with the use of very large telescopes (see, Gilliland et al. 1993). Although we cannot influence the weather conditions and the rotation of the Earth, is it possible to improve the precision of ground based photometric light curves?

The influence of atmospheric turbulence on the observed starlight has been studied since the beginning of systematic observations of stars with photometers. For example, Pont et al. 2006 shows that the main reason for the low detection rate of exoplanets from ground based surveys is the result of "red" (or non-Gaussian) noise in the light curves, mainly due to "atmospheric scintillation" effects.

While the fundamental effects of scintillation on stellar light curves were studied thoroughly by Dravins et al. 1997a, the instrumentation limitations of their time did not allow them to efficiently compare the light curves of multiple targets. The replacement of the photo-multiplying devices with the more efficient CCDs eliminated this problem thanks to their imaging abilities. The simultaneous observations of multiple stars allows for the correction of their long-term systematics by comparing them with each other. This process is known as *differential photometry*.

A surprising aftermath of the transition from the photomultipliers to CCDs is the abandonment of the photometric studies around bright stars. The differential photometry of bright stars using CCDs, is not trivial due to their limited dynamic range[1] which influences the observations in two ways; with the requirement for small exposure times in order to avoid overexposure of the chip and the absence of comparison stars in the same field of view (FOV) of the telescope. As shown by Dravins et al. 1997a the amplitude of scintillation noise can be considerably high in time scales smaller than 100 msec. As a result, due to the small exposure time and in addition to the slow read out process of the regular CCDs, the scintillation effects are not zeroed out efficiently, resulting in low accuracy light curves. A functioning solution regarding this matter is the performance of observations with the telescope slightly unfocused. This way the image of the star spreads to a larger number of pixels, which allows for larger exposure time. An other, more intrusive, method is the partial coverage of the telescope, in order to reduce the collecting area of the mirror. Yet, the usual absence of comparison stars with similar brightness in the telescope's FOV, may require the application of more complicated photometric methods, i.e., absolute photometry.

A fact which clearly points out those problems is the lack of recent photometric observations of bright variable stars, while there are less than 100 confirmed transiting planets around stars with $J_{2MASS} \leqslant 10$ mag, discovered from ground based surveys[2]. A comparison between the transit detections

[1]The real dynamic range of CCDs can be several times smaller than the one named by the manufacturer due to the non-zero brightness of the sky.

[2]There are $\sim 2.2 \times 10^6$ stars with $J_{2MASS} \leqslant 10$ mag

from ground-based and satellite surveys is demonstrated in Fig. 5.1. The vast majority of the planets which were detected from the ground have Jupiter-like radii and they orbit stars with visual brightness in the range between $8 \leqslant J_{2MASS} \leqslant 10$ mag. The smallest planet in that range of magnitudes is the super-Earth 55 Cnc e, which was discovered with RV measurements and later its transit was detected with ground-based observations.

The anticipated space missions PLATO 2.0 (Rauer et al. 2014) and TESS (Ricker et al. 2015) are designed with the prospect to search for small planets around bright stars. Ricker et al. 2015 proposes that, based on the *Kepler* mission results, the TESS satellite is expected to detect thousands of planets with sizes comparable to Neptune, some hundreds super-Earths and a few tens of Earth-like planets, around stars with $J_{2MASS} \leqslant 10$ mag.

Although the importance of space observatories is indisputable, it is of great importance to improve our observation techniques in order to produce light curves with similar levels of precision from the ground. To that end, the main goal of this study is to verify that it is possible to perform high speed observations with advanced imaging systems (see, Sect 5.4), in order to identify the characteristics of scintillation noise and remove it from the light curves. Based on the results of this study (Sect. 5.7), we conclude that our fast imaging telescope is capable to produce high precision photometric light curves of bright stars, while further fast imaging observations will possibly allow us to detect and perform follow up observations on exoplanets as small as our Earth[1], with the method of transits from the ground (Sect. 5.8).

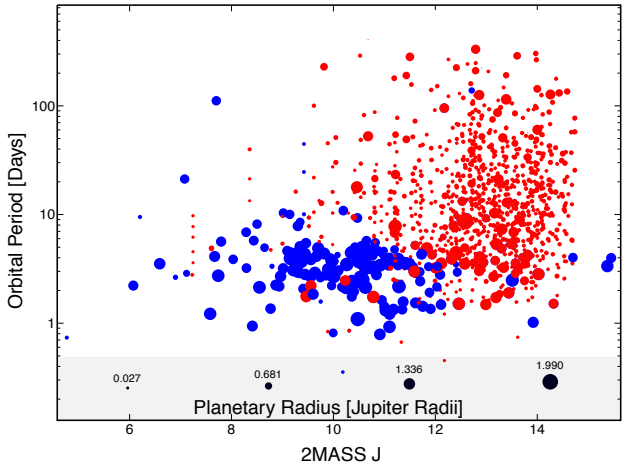

Figure 5.1: Comparison between the transit detections from satellites (red dots) and ground-based surveys (blue dots), according to htp://exoplanets.org as of Dec. 2015. The size of the dots demonstrates the scaled radius of the planets. Most of the detections from ground-based surveys are Hot-Jupiters (see, Sect. 1.4.2.4). Assuming that the rate of lower size planets to the Hot-Jupiters which were detected by satellites is stable, one expects to find numerous small planets around stars with $8 \leqslant J_{2MASS} \leqslant 12$. In addition there is an obvious lack of detections for stars with $J_{2MASS} \leqslant 8$

[1] around main sequence dwarf stars

5.2 Scintillation theory

The term atmospheric scintillation refers to the rapid fluctuations of light as a result of turbulence in the upper layers of the atmosphere. The Earth's atmosphere can be separated in a sequence of very thin layers, each with thickness δh. Every electromagnetic wave, propagating through the atmosphere, is phase shifted due to the refracting index n of each one of these layers (modeled as a turbulent scalar field). The phase shift $\phi_{\rm n}$ of a given wave-function with spacial coordinates x and y is equal to

$$\phi_{\rm n}(x,y) \;=\; \frac{2\pi}{\lambda}\int_{h}^{h+\delta h} n(x,y,z)\,{\rm d}z\,. \tag{5.1}$$

for a layer in altitude z (e.g. Roddier 1981). The final phase shift and the power spectrum of the variations is subject to the total height. Due to the turbulence in the distribution of n in the atmosphere, the phase shift of a wave is also position dependent. The phase of a wave with initial phase of unity, is given by

$$\psi_{\rm n}(x,y) \;=\; 1 + i\phi_n(x,y), \tag{5.2}$$

assuming $|\phi_n(x,y)| << 1$. A wave field at altitude $z = 0$, where a ground based telescope might be located, can be described by a Fresnel convolution of $\psi_{\rm n}(x,y)$ as

$$\psi_0(x,y) \;=\; \psi_{\rm n}(x,y) * \frac{1}{i\lambda h}\, e^{i\frac{\pi(x^2+y^2)}{\lambda h}}\,. \tag{5.3}$$

The amplitude and the phase shift of the wave are then given by the real and imaginary part of Eq. 5.3 as

$$R(x,y) = \phi_n(x,y) * \frac{1}{\lambda h}\,\cos\left(\frac{\pi(x^2+y^2)}{\lambda h}\right) \tag{5.4}$$

and

$$I(x,y) = \phi_n(x,y) * \frac{1}{\lambda h}\,\sin\left(\frac{\pi(x^2+y^2)}{\lambda h}\right) \tag{5.5}$$

respectively. The phase shifts of the wave field follow a Gaussian distribution and due to their multiplicative combination their logarithms add linearly. As a result the distribution of the intensity flux shifts should follow a log-normal distribution. When the wavefront does eventually reach the ground, it consists by moving bright and dark zones. The observed result is known as *twinkling* of the stars as well as the effect of "flying shadows" during solar eclipses.

For observations from a telescope with aperture D, greater than the diffraction Fresnel-zone size $\sqrt{\lambda h}$, the amplitude of the expected scintillation intensity fluctuations is independent from the wavelength and proportional to $D^{-7/3}$:

$$\sigma_I^2 \propto D^{-7/3}\int_0^{\infty} h^2 C_n^2(h)\,dh \tag{5.6}$$

where $C_n^2(h)$ is the the height-dependent structure function for the refraction index. The variance σ_I^2 demonstrates the power of scintillation in a light curve. Due to its dependence on the structure of the refraction index, weighted by h^2, it is expected that the main contribution to scintillation noise originates by high altitude turbulence. For telescopes with apertures close to the cut-off frequency $f_c = \frac{2\pi}{D}$ of the telescope, the variance σ_I^2 is wavelength dependent.

Naturally the atmosphere is not stable in time. The relative movements of the atmospheric layers depend on the wind velocity vector of each layer. When a wind gust moves a layer to a given direction during the observation of a star, the produced dark or bright light zone is crossing the telescope aperture and the observed starlight will *gradually* dim and brighten with respect to the structure of the zone. Consequently it is possible to study directly the spatial properties of the zones by measuring the autocorrelation function of the starlight intensity. The lifetimes of the scintillation zones are proportional to the differences of the wind speeds between various atmospheric layers, i.e., for a given velocity difference of 10 m/s results to a dark or bright zone with a typical Fresnel size ∼10 cm, with lifetime ∼10 ms. Is that a valid approximation though? A lot of ink has been spilled over the "frozen atmosphere" assumption of Taylor 1938, regarding the evolution time scales of the movement between various layers of the atmosphere. Thus I will not attempt to answer that question here. Yet, despite the true nature of atmospheric turbulence, the coherence of the scintillation zones should be preserved only if the velocity vectors of all atmospheric layers were identical. Therefore, it should be unusual to observe cross-correlated scintillation variations, even in stars with small angular separation (see Sect. 4 of Dravins et al. 1997a, for further details).

5.3 Previous observations

While the assets of CCDs make them superior to photomultipliers, the time which they need in order to complete their read out process, rendered the majority of them unable to perform high speed observations. As a result, most of the studies on scintillation and its effects on ground based photometry were performed before the 2000s.

As I mention in Sects 1.5 and 5.1, the effects of scintillation in photometric light curves (for a variety of telescope apertures, wavelengths, zenithal angles, etc) were studied thoroughly by Dravins et al. (1997a, b & c). While the series of papers from Dravis and colleagues covered the fundamental properties of scintillation noise in single star light curves, the limitations of the astronomical instrumentation at that time did not allow them to perform detailed studies in more than one targets simultaneously. In particular in Dravins et al. 1997a they mention; "the discussion in Sec. 5 should perhaps be seen as a pilot study for exploring the limits to statistical determinations, possibly to be revised as more perfect detectors become available", referring their difficulty to understand the significance of subtle detector effects in their data, because of the non simultaneity of different measurements.

The same authors propose that simultaneous observations of multiple targets would yield additional information about scintillation, as an ensemble of different statistical distributions. Based on those statements, we use the advances in imaging device technology, in order to perform simultaneous high speed observations (with the same instrument) in more than one stars.

5.4 Our equipment

The main idea behind the assemble of the fast telescope imager, is the study of scintillation effects in the light curves of more than one stars, simultaneously. Consequently the equipment was configured in favor of this idea.

As an optical tube we use the 14" (∼35.56 cm) Schmidt-Cassegrain from Celestron, which is mounted on a standard equatorial mount (10Micron, GM-2000). The focal length of the telescope, using the Cassegrain focus, is 3910 mm (f/11). Mounting the camera on the Cassegrain focus leads to the limited FOV of ∼11' (0.34"/pix). To cope with that issue we chose to mount the camera on the main focus of the telescope, with the Starizona's HyperStar imaging system. The HyperStar contain a configuration of lenses, in such way so the focal length is reduced to 684 mm (f/1.9). As a result, the final FOV of the system is increased to ∼1.1° (1.96"/pix).

The cameras used for our experiments are the sCMOS Andor Neo 5.5 and Andor Zyla 4.2. Due to the technical advantages of the sCMOS chips, in comparison to regular CCD chips, these cameras can reach frame rates up to 100 fps, in full frame operation. In addition the size of their chips, 2560 x 2160 pixels and 2048 x 2048 pixels respectively, allows for wide field imaging, if combined with the proper optics and telescope.

The camera is connected on a linux pc and it is operated with a C++ software based on the Andor's Software Developer Kit (SDK). The major development of the main part of this software was made by Andres Wass (in the context of his diploma thesis), in order to perform observations with the Andor Neo 5.5. Additional modifications and adjustments made by me, mainly for the transition from the Andor Neo 5.5 to the Andor Zyla 4.2.

Figure 5.2: The Andor NEO 5.5 on the main focus of the C14.

Figure 5.3: A sequence of the consecutive shots of the star Alcor with a rate of 400 fps. The star images are represented as speckles rather than the regular PSF, due to the seeing turbulence (see, Roddier 1981).

5.5 Data analysis

The first consideration regarding the functionality of our fast imaging instrument is the vast amount of data which are produced and stored, e.g. the storage space needed for 1 min observations in full frame, using 100 fps, is 48 Gb. To test our equipment we observed several times, using various camera settings, the field around the star Alcyone in the cluster of Pleiades. The Andor Neo 5.5 camera was not able to keep up with the desired data rate, due to its slow connection to the PC. As a result the internal buffer of the camera was full after a few seconds. To overcome this problem, we purchased the Andor Zyla 4.2. In order to obtain high rate, continuous observations, for more than a few minutes I use subframes 512 x 512 pixel. This way the size of the frames is reduced dramatically, while it is possible to operate the camera in higher rates than 100 fps.

Special consideration needs to be placed on the photometry procedure. The reasons are again the very large number of frames (more than 400000 per run) and the lack of the usual point spread function of the stars due to the atmospheric seeing (e.g., in Fig. 5.3 are demonstrated consecutive images of the star Altair). To that end, iI perform the photometry of the data with the algorithm SExtractor (Bertin & Arnouts 1996) bundles in a python based main script. In particular, after several tests, I found that the best results were produced with SExtractor's isophotal photometry (setting $FLUX\_ISO$). In order to create the light curves, the standard photometry procedure is followed; first the data are being reduced by the flats and bias frames and then the algorithm performs the photometry for each frame. The final light curves of the stars require further corrections, as they are influenced from systematics, e.g. the long term drift of the FOV, due to mount tracking errors. Such systematics are not identical from one star to the other and their impact to the light curves (which can reach up to a few percent in flux) depends on the SNR of the stars. To eliminate these sources of noise I remove, from the light curves, the correlated trends between the measured flux, the area (in pixels) and the x & y image coordinates of the star.

5.6 Observations

The results presented in this thesis are consisted by two observations; one containing the stars Alcor & Mizar and an other one containing the δ scuti star ϵ-Cep. The observation of the Alcor ($V_{mag} = 4.0$) & Mizar ($V_{mag} = 2.2$) lasted 26 mins in total and the main goal was to measure the autocorrelation and cross-correlation functions of non-variable stars. Thus I set the frame rate in 400 fps. In the same field (see, left-panel of Fig. 5.4) is also visible a third star, Stella Ludoviciana ($V_{mag} = 7.5$). The

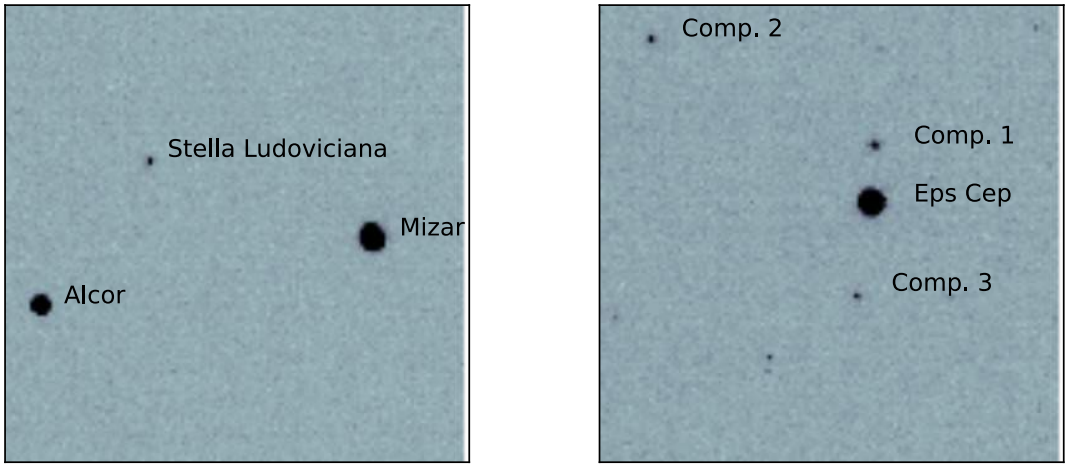

Figure 5.4: Left: The field including the stars Mizar, Alcor and St. Lud. Mizar B is responsible for the excess of light on the top of Mizar A. Right: The field of -Cep. The brightness of the comparison stars range between $V_{mag} = 9.2$ and $V_{mag} = 11$. Due to the longer exposure time, more stars are visible, in comparison to the Alcor & Mizar field.

signal to noise (SNR) of this star in the frames is ∼70. Mizar A is a double star with a companion, Mizar B ($V_{mag} = 3.9$), at angular distance of 14.41 arcsec. With the deblending function of SExtractor, the photometry of both objects is possible. Nevertheless, due to the small angular separation, the photometry of this star is still influenced by Mizar A, so I excluded it from the results.

The second field was chosen in order to test the ability of our fast imaging instrument to detect a signal with amplitude in the regime of 1-2%, i.e. the average depth of transit from a Hot-Jupiter. To that end I selected the δ-scuti star, ϵ-Cep ($V_{mag} = 4.4$). The pulsations of ϵ-Cep were reported from Seeds & Price 1983 to have amplitude of ∼2% and period between 0.036 days and 0.042 days. The results of Seeds & Price 1983 are also supported by latter observations using the ground based photometer of Observatorio de Sierra Nevada (OSN) along with observations from the WIRE satellite from Bruntt et al. 2007, who discovered multiple periodicities in the light curves of ϵ-Cep. Our set of observations lasted for 90 mins, in order to observe at least 1.5 times the reported period. There are no stars with similar brightness in the field of ϵ-Cep (cf., right-panel of Fig. 5.4). Consequently, I set the frame rate to 79 fps, in order to improve the SNR of the field's comparison stars. I summarize my observations in Table 5.1.

Target	Obs. Time (mins)	fps	No. of Stars
Alcor & Mizar	26	400	3
ϵ-Cep	90	79	4

Table 5.1: A table with the observed fields, the total observation time and the frame rate per target.

5.7 Results

5.7.1 Auto- and cross-correlation

The observations of the Alcor & Mizar field were performed with 400 fps, in order to test the efficiency of our equipment regarding scintillation studies. As it is illustrated in Fig. 5.5, the light curves of all stars demonstrate scintillation fluctuations, with amplitudes in the range of 20-50%. The variations of the brighter stars are dominated by correlated noise and they do not last longer than 100-120 msec. On the other hand, the light curve of the fainter star (Stella Ludoviciana, see Fig. 5.4) is more complicated, probably due to the small SNR. While the fluctuations of all stars appear to be periodic periodic, there are no evidences of periodicities in the L-S periodograms of the light curves.

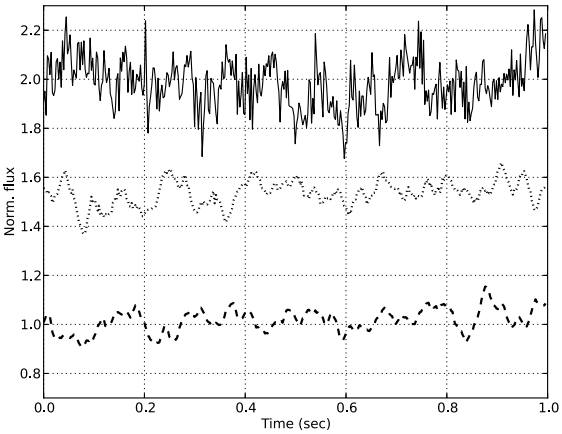

Figure 5.5: Demonstration of the light curves of the stars Mizar ($V_{mag} = 2.2$), Alcor ($V_{mag} = 4.0$) and Stella Ludoviciana ($V_{mag} = 7.5$), with duration 1 sec. There are clear variations with amplitudes in the order of 20-50%, caused by atmospheric scintillation.

Another clear feature of the light curves, in this time domain, is the fact that the scintillation fluctuations are not correlated between the stars, i.e., a dip in the light curve of Mizar (dashed line) does not necessarily appear in the light curves of the other stars. In larger time domains though there are obvious correlations between the light curves, caused by "slower" variations, i.e. the reduction of the stellar intensity due to atmospheric extinction, as the angle between the FOV and Zenith increases.

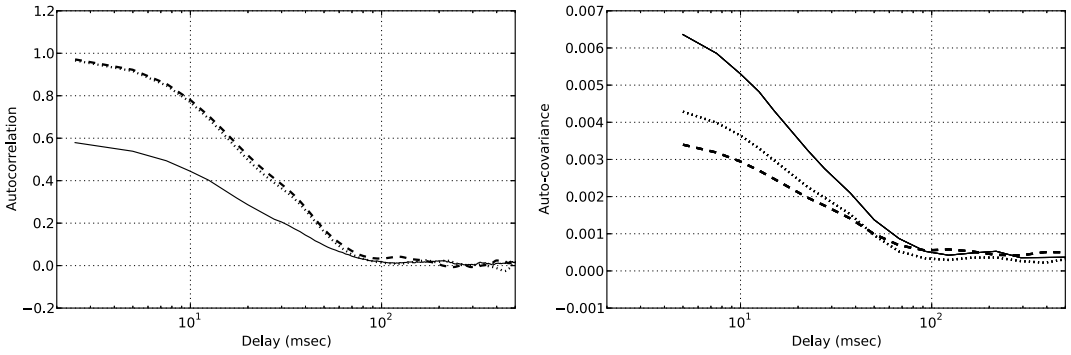

Figure 5.6: The autocorrelation (left) and auto-covariance (right) functions of the three stars. The results are in agreement with the results of Dravins et al. 1997a. The autocorrelation function of the fainter star has lower max-value, probably due to the increased noise in its light curve.

As expected from scintillation theory, the autocorrelation and the covariance functions of the stars demonstrate similar behaviors. Although, the maximum autocorrelation value of the fainter star (Stella Ludoviciana) is significantly lower than Mizar and Alcor, its general behavior is also in agreement with the other two. As it is clear from Fig. 5.6, the individual data points stop to be correlated for delays larger than 100 msec.

A broadly used method to effectively improve the precision of the light curves is by binning them. Fig. 5.7 demonstrates the variation of the standard deviation of the binned light curves, in respect to the size of the bins. The precision of the light curves remains almost stable for integrations smaller than 100 msec, which is the autocorrelation limit (cf., Fig. 5.6). For larger integrations, the effects of scintillation are summed up and they are propagated as gaussian noise. As a result the precision of the light curves improves as expected; inversely proportional to the number N of data points per bin:

$$\sigma_{\text{mean}} = \frac{\sigma_0}{\sqrt{N}} \,. \tag{5.7}$$

The red line, in Fig. 5.7, represents the expected precision, under the assumption that the light curves are clean of correlated noise and with the same initial standard deviation as the light curve of Mizar. The final discrepancy between the expected and calculated standard deviation is in the order of one magnitude. This is exactly the reason behind the precision loss of the ground based observations, in comparison the space based observations.

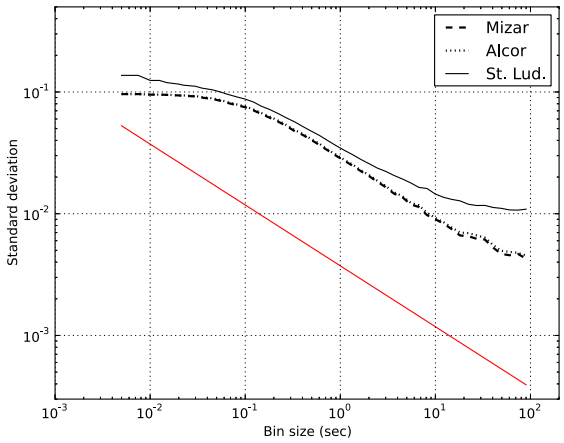

Figure 5.7: The standard deviation of binned light curves in respect to the size of the bins. All light curves reach precision of ∼0.5%, when binned with iterations longer than 60 seconds. The red line represents the expected light curve precision, assuming that the light curves are free of any kind of correlated noise. The divergence of the star St. Lud. is due to the lower SNR of its light curve. The degeneration of the plots for bins larger than 60 sec is due to under sampling.

5.7.2 Differential photometry of ϵ-Cep

The precision of the light curves, for each star in our sample, reaches values lower than 1%, when we are using bins larger than ∼10 sec. Furthermore, for the bright stars ($V_{mag} < 5$) it reaches values lower than 0.5% with binning integrations longer than ∼1 min. While this level of precision is not sufficient for the characterization of small exoplanets, it is acceptable for studies on eclipsing binaries and large exoplanets, i.e., in the size of Jupiter.

As a case study we observed the δ-scuti star, ϵ-Cep. In order to perform the differential photometry, I used the light curve from the star noted as "Comp. 2" ($V_{mag} = 10.1$) and I also used the "Comp. 3" ($V_{mag} = 10.2$) and "Comp. 1" ($V_{mag} = 9.2$) as check stars (cf., Fig. 5.4). In the top-panel of Fig 5.8 is illustrated the light curve of ϵ-Cep, where one can clearly distinguish the pulsations of the star and their periodic nature. Additionally there is visual evidence for a second order periodic signal. The most prominent period of the pulsations, is calculated using a L-S periodogram at 0.048 mins (bottom-panel of Fig. 5.8).

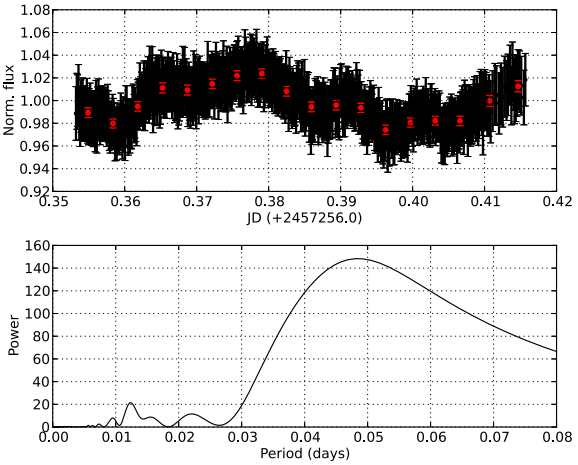

Figure 5.8: Top: The light curve of ϵ-Cep variable star. The black points are integrations of 790 exposures (10 sec) while the red points are integrations of 23700 exposures (5 mins). Bottom: The result of the Lomb Scargle periodogram. The leading period is 0.048 days.

The results are in good agreement with previous studies on ϵ-Cep (cf., Seeds & Price 1983 and Bruntt et al. 2007). While, there is no additional information about the physical processes on ϵ-Cep, it is clear from Fig 5.8 that we can perform high precision studies of bright variable stars, with high time resolution measurements, even without sophisticated data analysis. The requirement for an instrument which can perform such observations is emphasized by the very small number of published light curves of bright variable stars, e.g. the number of the published light curves of ϵ-Cep is not larger than five, while the quality of the existing light curves is controversial.

5.8 Conclusions and Discussion

The calculated autocorrelation and auto-covariance functions of the light curves of all our targets, agree with the results of Dravins et al. 1997a, as it is presented in Fig. 5.6. In addition, I measure the statistics of the light curves of multiple stars, using the same instrument. This allows to distinguish easier the systematic trends and thus to efficiently compare the effects of scintillation noise on light curves of different targets in the same FOV. As shown in Fig. 5.7, the impact of scintillation in the precision of the light curves is very large, i.e., without the effects of scintillation, the transit of an Earth-like planet like 55 Cnc e would be visible. Systematic, high speed observations of multiple targets might allow us to eliminate the scintillation effects using differential photometry and more sophisticated data analysis, e.g. the application of a high pass frequency filter on high speed light curves.

The detection of the pulsations of the ϵ-Cep, using differential photometry, demonstrates the power of our fast imager. Its ability to reach precision levels lower than 0.5% (comparable to observations made by telescopes with much larger diameter, e.g. Mislis & Schmitt 2009), renders it ideal for follow up observations on bright variable stars and large exoplanets. Furthermore, based on this study, should be possible to detect the transits of small planets, like Neptune, with integrations longer than a few minutes. Consequently a fast imager with the configuration presented in Fig. 5.2 can operate in survey mode due to its relatively wide field of view.

According to the results of Sect. 5.7, it is possible to identify the systematic errors which are introduced to the light curves from the instrument, using differential photometry. Given that fact, it would be interesting to perform fast imaging photometry in the same field, using an array of different telescopes. Assuming that the principals about scintillation theory are correct, it must be possible to follow the flying-shadows (see, Sect. 5.2) of a star, as they sweep across the different optical tubes. As a result the light curves of the same star from different telescopes, normalized and clean from instrumental systematics, should be cross-correlated with time delay inversely proportional to the speed of the shadows. Assuming that something like that is possible, we should be able to reference the scintillation variations in the simultaneous light curves of the same star from different telescopes and thus to subtract them.

While the fast imaging instrument is ideal for scintillation studies and bright star observations, there are several more astronomic applications for a telescope with large FOV and high frame acquisition rates. Next to high time resolution studies, such as transit timing, short duration stellar flares etc., our system can perform with great accuracy studies on lunar or planetary occultations of stars and lunar impacts. This kind of studies are performed as of today by 60 fps, 8-bit video cameras. As a result the measurements suffer from great uncertainties, due to the low dynamic range. In contrasts the high dynamic range of the Zyla 4.2 (16-bit) can cover larger brightness fluctuations, which can lead to better estimation of the properties of the observed events.

Chapter 6

Summary

One of the most heated subjects in human history, is the question about the existence of planets around other stars and their ability to sustain life. About twenty years ago, the first part of this question was answered with the confirmation of the detection of the first exoplanet, around a main sequence star. The launch and operation of space based observatories accelerated the detection rate of exoplanets, allowing us to explore their vast variety of sizes and configurations. As a result we slowly begin to understand processes like the planet formation or to make estimations on the population of the planets in our galactic neighborhood.

The main goal of my thesis is to improve the characterization of transiting extra solar planets around magnetically active stars. Following this logic I began the characterization effort of the planets Kepler-210 b and Kepler-210 c (see, Sect. 2). Both planets demonstrate transit timing variations (TTV). Despite the fact that the transits are affected by spot-crossing events (the occultation of the planet over a starspot during the transit), we proved that the TTV are real. Also, we use the so-called photo-eccentricity effect (Dawson & Johnson 2012)[1] in oder to prove that the orbits of the planets are highly eccentric. In order to explain the observed TTV and to test the stability of the system, I used n-body simulations, the results of which suggest that the TTV are not possible to be explained by the two planets alone. As a result we suggest the existence of an outer third planet, which we name KOI-676.03. Although the solutions for the orbit and mass of the planet KOI-676.03 are not unique, the most preferable configuration suggests a planet with mass $\sim$0.3-0.6 M_J in an slightly eccentric ($e \simeq 0.2$) orbit with period $\sim$63 days. If this is true, then the planet should be detectable with RV measurements.

The existence of photometric modulations in the light curve of Kepler-210, triggered multiple times the question if the observed TTV could be the result of spot-crossing events as others suggested in the past (Oshagh et al. 2013). To study the ways with which spot-crossing events affect single and consecutive transits I set up series of simulations with a variety of planet-star configurations, which I present in Sect. 3. The conclusion of this work is that spot-crossing events can introduce TTV with amplitudes 1% or less of the transit duration, depending on the location of the event in the transit profile. Properties that might slightly affect the location were the amplitude of the induced TTV is larger, are the limb darkening coefficients and the impact parameter. Assuming that the spot life-times are much larger than the rotational and orbital periods of the star and the planet respectively, the spot crossing events over such an active region can create, statistically significant, periodical signals. As a result the detection of TTV with amplitudes close to $\sim$ 1% of the transit duration, especially for planets

[1] I became aware about the Dawson & Johnson (2012) work, shortly after the publication of my paper on Kepler-210

with signal-to-noise ration in transit $\lesssim 15$, should be treated with caution. While my research was focused on the effect of spot-crossing events on TTV, it became clear to me that the same principles apply on the eclipse timing variations (ETVs) of binary stars.

Although the main target of my research on the system Kepler-210 was the characterization of the planets, I also studied the photospheric activity of the host star which is manifested as $\sim$2% modulations in the *Kepler* light curve. To fit the photometric modulations of Kepler-210 I apply a five spot model. Furthermore, I use the phenomenology of the phase folded light curve in combination with the resulted star spot locations in order to study the long-term photospheric evolution of Kepler-210. The visible momentum between different active regions (see, Fig. 4.4) can be confirmed with the use of L-S periodograms in accordance to the claims of Reinhold et al. (2013) and it consists a clear indication that the star is rotating differentially. The evolution of the starspots in time can be organized in six different "spot seasons". Evidences for the existence of those seasons consist the variance of the prominent period of the L-S periodogram of each one of then along with the cross-correlation of the corresponding parts of the light curve. The period variations in the leading period of the spots for each season, and thus their stellar latitude, is similar to those of sunspots during the 11-year magnetic cycles of the Sun. Finally, the life time of the active regions on the surface of Kepler-210 is estimated between $\sim$60 days and $\sim$90 days.

An effective method in order to extract information about the properties of the spots of a star is the exploitation of transiting/eclipsing companions in front of their primary star. To that end I propose the application of the unsharp masking method in the light curves of the transit residuals (see, Sect. 4.2). In addition, the comparison of the unsharp masking of the transit residuals with the $O-C$ diagram consists a fast and reliable way for the validation of the TTV of a system. Following this principle I study the timing variations and the photometric modulations of KOI-1452. Using the unsharp masking method I prove that the occulted spots are responsible for the measured ETV of KOI-1452, while in addition they are not responsible for the modulations in the *Kepler* light curve of the system. The hypothesis that the primary star of KOI-1452 is a γ Dor variable can naturally explain the periodicities of 1.9 days and larger with the most high powers in the Lomb-Scargle periodogram of the light curve, while the star spots which are occulted during the eclipses might be possible to explain the peak close to 1.17 days.

Despite the great success the space based observatories and the explosion of planet detected by them, they suffer from some very large disadvantages, i.e. the manufacturing costs or the immense difficulties in their maintenance. Consequently, the best solution for follow up observations or new surveys, is the establishment of an instrument on the earth, with the ability to reduce or even eliminate the atmospheric scintillation effects. Although this is an ambitious statement, we have made a few steps in that direction, with the assemble of a fast photometry telescope (see, Sect.5.4). The results of the first observations are very promising as 1) we are able to measure the autocorrelation functions of multiple stars simultaneously and 2) we manage to detect the signal of the δ-Scuti variable star ϵ-Cep. The future observations with this system will help us to understand the scintillation processes and the mechanisms with which it is affecting the earth based observations, in order to eliminate it.

The catalog with new planet detections grows day by day followed by the opportunities for new studies and discoveries. The research on planets around young, active, stars could reveal the procedures which led to the creation of the Solar System as we know it, and therefor they may bring us closer to unravel the mysteries regarding the origins of life.

Nomenclature

General Symbols

α	Semi-major axis
au	Astronomical unit, $149.6x10^6km$
b	impact parameter
e	eccentricity
Gb	Giga bites
K_{p}	Kepler magnitude
$M_{\odot}$	The mass of the Sun
$M_{\oplus}$	The mass of the Earth
$M_{\star}$	The mass of a star
M_{J}	The mass of planet Jupiter
M_{pl}	The radius of a planet
$R_{\odot}$	The radius of the Sun
$R_{\oplus}$	The radius of the Earth
$R_{\star}$	The radius of a star
R_{J}	The radius of planet Jupiter
R_{pl}	The radius of a planet
T_{o}	A reference transit epoch
V_{mag}	Magnitude of a star in the visible wavelength range

Observatories

CoRoT	COnvection ROtation et Transits

GTC Gran Telescopio Canarias

LBT Large Binocular Telescope

$PLATO$ PLAnetary Transits and Oscillations

$SALT$ Southern African Large Telescope

$TESS$ Transiting Exoplanet Survey Satellite

VLT Very Large Telescope

XMM X-ray Multi-Mirror mission

Acronyms

CCD Charge-coupled device

EB Eclipsing binaries

ETV Eclipse timing variations

FAP False alarm probability

FOV Field of view

fps Frames per second

KIC Kepler input catalog

KOI Kepler object of interest

$L-S$ Lomb Scargle periodogram

LD Limb darkening

LDC Limb darkening coefficients

$MCMC$ Marcov chain monte carlo

$O-C$ Residuals between the observed measurements and the values of a calculated ephemeris

PSF Point spread function

RV Radial velosity

$sCMOS$ Scalable complementary metal-oxide semiconductor

SNR signal to noise ratio

$TSNR$ signal to noise ratio of a transit

TTV Transit timing variations

References

Agol, E., Steffen, J., Sari, R., & Clarkson, W. 2005, MNRAS, 359, 567 13, 23, 31, 39, 67

Armstrong, D. J., Gómez Maqueo Chew, Y., Faedi, F., & Pollacco, D. 2014, MNRAS, 437, 3473 69, 71

Babcock, H. W. 1953, ApJ, 118, 387 7

Babcock, H. W. 1961, ApJ, 133, 572 5

Baglin, A., Auvergne, M., Barge, P., et al. 2006, in ESA Special Publication, Vol. 1306, ESA Special Publication, ed. M. Fridlund, A. Baglin, J. Lochard, & L. Conroy, 33 15, 39, 57, 67

Bakos, G., Noyes, R. W., Kovács, G., et al. 2004, PASP, 116, 266 14

Balbus, S. A. & Weiss, N. O. 2010, MNRAS, 404, 1263 74

Barnes, S. A. 2007, ApJ, 669, 1167 27

Barros, S. C. C., Boué, G., Gibson, N. P., et al. 2013, MNRAS, 430, 3032 16, 39, 51

Basri, G., Walkowicz, L. M., & Reiners, A. 2013, ApJ, 769, 37 40

Batalha, N. M., Rowe, J. F., Bryson, S. T., et al. 2012, ArXiv e-prints 23, 25

Beaulieu, J.-P., Bennett, D. P., Fouqué, P., et al. 2006, Nature, 439, 437 13

Berdyugina, S. V. 2005, Living Reviews in Solar Physics, 2, 8 31

Bertin, E. & Arnouts, S. 1996, A&AS, 117, 393 84

Bessel, F. W. 1844, MNRAS, 6, 136 10

Bonomo, A. S. & Lanza, A. F. 2012, A&A, 547, A37 57

Borucki, W. J., Koch, D., Basri, G., et al. 2010, Science, 327, 977 57

Borucki, W. J., Koch, D. G., Basri, G., et al. 2011, ApJ, 736, 19 15, 23

Brun, A. S. & Palacios, A. 2009, ApJ, 702, 1078 74

Bruntt, H., Suárez, J. C., Bedding, T. R., et al. 2007, A&A, 461, 619 85, 88

REFERENCES

Campbell, B., Walker, G. A. H., & Yang, S. 1988, ApJ, 331, 902 11

Carrington, R. C. 1863, Observations of the spots on the sun from November 9, 1853, to March 24, 1861, made at Redhill (London [etc.] Williams and Norgate), 604 4

Carter, J. A. & Winn, J. N. 2009, ApJ, 704, 51 27

Chabrier, G. & Küker, M. 2006, A&A, 446, 1027 57

Charbonneau, D., Brown, T. M., Latham, D. W., & Mayor, M. 2000, ApJ, 529, L45 12

Chauvin, G., Lagrange, A.-M., Zuckerman, B., et al. 2005, A&A, 438, L29 14

Claret, A., Hauschildt, P. H., & Witte, S. 2012, VizieR Online Data Catalog, 354, 69014 25, 43

Czesla, S., Huber, K. F., Wolter, U., Schröter, S., & Schmitt, J. H. M. M. 2009, A&A, 505, 1277 15, 39, 67, 70, 72

Dawson, R. I. & Johnson, J. A. 2012, ApJ, 756, 122 91

Donati, J.-F. & Collier Cameron, A. 1997, MNRAS, 291, 1 7

Dravins, D., Lindegren, L., Mezey, E., & Young, A. T. 1997a, PASP, 109, 173 17, 79, 82, 86, 89

Dravins, D., Lindegren, L., Mezey, E., & Young, A. T. 1997b, PASP, 109, 725 17

Dravins, D., Lindegren, L., Mezey, E., & Young, A. T. 1998, PASP, 110, 610 17

Edlén, B. 1943, ZAp, 22, 30 6

Fabrycky, D. C., Ford, E. B., Steffen, J. H., et al. 2012, ApJ, 750, 114 16, 39, 67

Fabrycky, D. C., Lissauer, J. J., Ragozzine, D., et al. 2014, ApJ, 790, 146 58

Fang, J. & Margot, J.-L. 2012, ApJ, 761, 92 58

Fekel, F. C. 1980, in Bulletin of the American Astronomical Society, Vol. 12, Bulletin of the American Astronomical Society, 500 7

Figueira, P., Marmier, M., Boué, G., et al. 2012, A&A, 541, A139 58

Frasca, A., Fröhlich, H.-E., Bonanno, A., et al. 2011, A&A, 532, A81 57

Fröhlich, C. 2012, Surveys in Geophysics, 33, 453 5

Fröhlich, H.-E., Küker, M., Hatzes, A. P., & Strassmeier, K. G. 2009, A&A, 506, 263 15, 57

Galle, J. G. 1846, MNRAS, 7, 153 9

Gatewood, G. & Eichhorn, H. 1973, AJ, 78, 769 10

Gilliland, R. L., Brown, T. M., Kjeldsen, H., et al. 1993, AJ, 106, 2441 79

Gilliland, R. L., Jenkins, J. M., Borucki, W. J., et al. 2010, ApJ, 713, L160 42

Guzik, J. A., Kaye, A. B., Bradley, P. A., Cox, A. N., & Neuforge, C. 2000, ApJ, 542, L57 74

Hale, G. E. 1908, ApJ, 28, 315 5

Heintz, W. D. 1988, JRASC, 82, 140 10

Henry, G. W., Eaton, J. A., Hamer, J., & Hall, D. S. 1995, ApJS, 97, 513 8, 15

Henry, G. W., Marcy, G. W., Butler, R. P., & Vogt, S. S. 2000, ApJ, 529, L41 12

Hershey, J. L. 1973, AJ, 78, 421 10

Hertzog, K. P. 1988, QJRAS, 29, 277 9

Holman, M. J. & Murray, N. W. 2005, Science, 307, 1288 23

Howard, R. & Harvey, J. 1970, Sol. Phys., 12, 23 63

Huber, K. F., Czesla, S., Wolter, U., & Schmitt, J. H. M. M. 2009, A&A, 508, 901 39, 57, 58, 69

Huber, K. F., Czesla, S., Wolter, U., & Schmitt, J. H. M. M. 2010, A&A, 514, A39 15

Ioannidis, P., Huber, K. F., & Schmitt, J. H. M. M. 2016, A&A, 585, A72 67, 68, 71

Ioannidis, P., Schmitt, J. H. M. M., Avdellidou, C., von Essen, C., & Agol, E. 2014, A&A, 564, A33 57, 58

Jacob, W. S. 1855, MNRAS, 15, 228 10

Jenkins, J. M., Caldwell, D. A., Chandrasekaran, H., et al. 2010, ApJ, 713, L120 69

Jetsu, L., Huovelin, J., Tuominen, I., et al. 1990, A&A, 236, 423 8

Johansen, A., Davies, M. B., Church, R. P., & Holmelin, V. 2012, ApJ, 758, 39 58

Kaye, A. B., Handler, G., Krisciunas, K., Poretti, E., & Zerbi, F. M. 1999, PASP, 111, 840 74

Kinemuchi, K., Barclay, T., Fanelli, M., et al. 2012, PASP, 124, 963 57

Koch, D. G., Borucki, W. J., Basri, G., et al. 2010, ApJ, 713, L79 39, 67

Küker, M. & Rüdiger, G. 2008, Journal of Physics Conference Series, 118, 012029 57

Lanza, A. F., Pagano, I., Leto, G., et al. 2009, A&A, 493, 193 15

Lanza, A. F., Rodonò, M., Pagano, I., Barge, P., & Llebaria, A. 2003, A&A, 403, 1135 5

Leighton, R. B. 1959, ApJ, 130, 366 7

Levison, H. F. & Duncan, M. J. 1994, Icarus, 108, 18 31

REFERENCES

Lissauer, J. J., Marcy, G. W., Bryson, S. T., et al. 2014, ApJ, 784, 44 15

Lissauer, J. J., Marcy, G. W., Rowe, J. F., et al. 2012, ApJ, 750, 112 15, 23

Lissauer, J. J., Ragozzine, D., Fabrycky, D. C., et al. 2011, ApJS, 197, 8 31

Lithwick, Y., Xie, J., & Wu, Y. 2012, ApJ, 761, 122 31

Mandel, K. & Agol, E. 2002, ApJ, 580, L171 12, 25, 42, 43, 70

Mao, S. & Paczynski, B. 1991, ApJ, 374, L37 13

Marsh, T. R. & Horne, K. 1988, MNRAS, 235, 269 7

Masuda, K., Uehara, S., & Kawahara, H. 2015, ApJ, 806, L37 50

Maunder, E. W. 1904, MNRAS, 64, 747 4

Mayor, M., Queloz, D., Marcy, G., et al. 1995, IAU Circ., 6251, 1 11

Mazeh, T., Holczer, T., & Shporer, A. 2015, ApJ, 800, 142 51

Mazeh, T., Nachmani, G., Holczer, T., et al. 2013, ApJS, 208, 16 16, 39, 50, 67, 71

McQuillan, A., Aigrain, S., & Roberts, S. 2012, A&A, 539, A137 57

McQuillan, A., Mazeh, T., & Aigrain, S. 2014, ApJS, 211, 24 57

Mislis, D. & Schmitt, J. H. M. M. 2009, A&A, 500, L45 89

Mitchell, S. A. 1929, Popular Astronomy, 37, 192 6

Morton, T. D. & Winn, J. N. 2014, ApJ, 796, 47 58

Moulton, F. R. 1899, AJ, 20, 33 10

Nesvorný, D., Kipping, D., Terrell, D., et al. 2013, ApJ, 777, 3 39

Orosz, J. A. 2015, ArXiv e-prints 50

Oshagh, M., Santos, N. C., Boisse, I., et al. 2013, A&A, 556, A19 16, 39, 51, 67, 91

Pallavicini, R., Golub, L., Rosner, R., et al. 1981, ApJ, 248, 279 7

Parker, E. N. 1979, Cosmical magnetic fields: Their origin and their activity 6

Petigura, E. A. & Marcy, G. W. 2012, PASP, 124, 1073 57

Pollacco, D. L., Skillen, I., Collier Cameron, A., et al. 2006, PASP, 118, 1407 14

Pollack, J. B., Hubickyj, O., Bodenheimer, P., et al. 1996, Icarus, 124, 62 12

Pont, F., Zucker, S., & Queloz, D. 2006, MNRAS, 373, 231 79

Qiu, P., Mao, Y.-N., Lu, X.-M., Xiang, E., & Jiang, X.-J. 2013, Research in Astronomy and Astrophysics, 13, 615 17

Rabus, M., Alonso, R., Belmonte, J. A., et al. 2009, A&A, 494, 391 39, 67

Rauer, H., Catala, C., Aerts, C., et al. 2014, Experimental Astronomy, 38, 249 16, 80

Reiger, S. H. 1963, AJ, 68, 395 17

Reiners, A. & Schmitt, J. H. M. M. 2002, A&A, 384, 155 7

Reinhold, T. & Reiners, A. 2013, A&A, 557, A11 57

Reinhold, T., Reiners, A., & Basri, G. 2013, A&A, 560, A4 16, 57, 62, 73, 92

Ricker, G. R., Winn, J. N., Vanderspek, R., et al. 2015, Journal of Astronomical Telescopes, Instruments, and Systems, 1, 014003 16, 80

Roddier, F. 1981, Progress in optics. Volume 19. Amsterdam, North-Holland Publishing Co., 1981, p. 281-376., 19, 281 81, 84

Rodono, M. & Cutispoto, G. 1992, A&AS, 95, 55 8

Rodono, M., Cutispoto, G., Pazzani, V., et al. 1986, A&A, 165, 135 8

Sanchis-Ojeda, R., Winn, J. N., Holman, M. J., et al. 2011, ApJ, 733, 127 16, 39, 45, 67

Schwabe, M. 1844, Astronomische Nachrichten, 21, 233 4

See, T. J. J. 1896, AJ, 16, 17 10

Seeds, M. A. & Price, C. W. 1983, Information Bulletin on Variable Stars, 2278, 1 85, 88

Sheeley, Jr., N. R. 1967, ApJ, 147, 1106 7

Snodgrass, H. B. & Ulrich, R. K. 1990, ApJ, 351, 309 63

Spoerer, F. W. G. 1890, MNRAS, 50, 251 4

Steffen, J. H., Fabrycky, D. C., Agol, E., et al. 2013, MNRAS, 428, 1077 16, 23

Strassmeier, K. G., Hall, D. S., Boyd, L. J., & Genet, R. M. 1989, ApJS, 69, 141 8

Struve, O. 1952, The Observatory, 72, 199 11

Szabó, R., Szabó, G. M., Dálya, G., et al. 2013, A&A, 553, A17 16, 39, 67, 71

Tassoul, M. 1980, ApJS, 43, 469 74

Taylor, G. I. 1938, Proceedings of the Royal Society of London Series A, 164, 476 82

Tingley, B. & Sackett, P. D. 2005, ApJ, 627, 1011 28

Tremaine, S. & Dong, S. 2012, AJ, 143, 94 58

Vaiana, G. S., Cassinelli, J. P., Fabbiano, G., et al. 1981, ApJ, 245, 163 7

van de Kamp, P. 1963, AJ, 68, 515 10

Van Reeth, T., Tkachenko, A., Aerts, C., et al. 2015, ApJS, 218, 27 74

Vogt, S. S. & Penrod, G. D. 1983, PASP, 95, 565 7

Walker, G. A. H., Bohlender, D. A., Walker, A. R., et al. 1992, ApJ, 396, L91 11

Walkowicz, L. M. & Basri, G. S. 2013, MNRAS, 436, 1883 16

WGESP IAU. 2003, Defintion of a "Planet", working group on extrasolar planets (WGESP) of the international astronomical union 9

Wilson, O. C. 1968, ApJ, 153, 221 7

Wilson, O. C. 1978, ApJ, 226, 379 7

Wolszczan, A. & Frail, D. A. 1992, Nature, 355, 145 10, 11

Wolter, U., Schmitt, J. H. M. M., Huber, K. F., et al. 2009, A&A, 504, 561 15, 25, 39, 67, 73

Zechmeister, M. & Kürster, M. 2009, A&A, 496, 577 47, 58, 69, 71

Hiermit erkldre ich an Eides statt, dass ich die vorliegende Dissertationsschrift selbst verfasst und keine anderen als die angegebenen Quellen und Hilfsmittel benutzt habe.
I hereby declare, on oath, that I have written the present dissertation by my own and have not used other than the acknowledged resources and aids.

Hamburg, den 06.09.2016 Unterschrift